

2015-01-28

Improving Reservoir Simulation using Seismic Data

Shamsa, Amir

Shamsa, A. (2015). Improving Reservoir Simulation using Seismic Data (Doctoral thesis, University of Calgary, Calgary, Canada). Retrieved from <https://prism.ucalgary.ca>. doi:10.11575/PRISM/26494
<http://hdl.handle.net/11023/2030>

Downloaded from PRISM Repository, University of Calgary

UNIVERSITY OF CALGARY

Improving Reservoir Simulation using Seismic Data

by

Amir Shamsa

A THESIS

SUBMITTED TO THE FACULTY OF GRADUATE STUDIES
IN PARTIAL FULFILMENT OF THE REQUIREMENTS FOR THE
DEGREE OF DOCTOR OF PHILOSOPHY

DEPARTMENT OF GEOSCIENCE

CALGARY, ALBERTA

January, 2015

© Amir Shamsa 2015

Abstract

The principal premise of this thesis is that the ambiguities of reservoir simulation can be and should be reduced by using time-lapse seismic data. Such data can be considered as a sort of reservoir dynamic data, with distinctive features compared to the typical reservoir production data. While well production data are sparse in space and dense in time, 4D time-lapse seismic can be utilized to fill the spatial data gaps between wells. This provides an opportunity to constrain reservoir dynamic behaviour not only at well locations but also between them by honoring time lapse response of the reservoir. This means that seismic assisted history matching should involve a simultaneous minimization of the mismatch between all types of measured and simulated data including seismic data.

This thesis is an effort to discuss critical aspects of integrating 4D time-lapse data in reservoir simulation and history matching. I have illustrated a detailed scheme of seismic assisted history matching with implications on real data, to emphasize the extra value that seismic data can bring into the conventional reservoir history matching. This goal was followed by developing a software application to assess the feasibility of the theory at industrial scales. In addition to the conventional oils, a significant effort has been devoted to extend the scope of the work to viscoelastic heavy oils and their fluid substitution models in thermal cases. I also studied the production/injection induced stresses impacts on anisotropic velocity variations, using coupled geomechanical-flow simulations.

The delineated scheme in seismic assisted history matching, proved to have a crucial contribution that cannot be ignored. The dynamic model for reservoir simulation should always be kept as simple as possible, but not simpler! This thesis is an argument that ignoring time lapse seismic data, builds a model which is simpler than a trustworthy model.

Acknowledgements

I would like to give my special thanks to my supervisor, Dr. Larry Lines, who has been supportive with providing the vision and encouragement during my doctoral program. He is not only a great supervisor and knowledgeable adviser but also an esteemed teacher in my life.

I would love to acknowledge the significant role of teachers, who portrayed my life trend in different aspects, among them are Mr. Mohammad Rashidpour, Dr. Pooladi Darvish, Dr. Gary Margrave and Dr. Edward Krebes.

I would like to thank the Consortium for Heavy Oil Research by University Scientists (CHORUS), and its coordinator Joan Embleton and also industry sponsors of CHORUS for generous software donation, financial support and providing data for this research.

I also would like to acknowledge Schlumberger's supports for providing required software and an internship opportunity.

I am also thankful to Seyyed Mohammad Hosseini, Hossein Aghabarati, Hassan Khaniani and Mehdi Paydayesh for their critical insights.

I also acknowledge and thank Sergei Filin, and Karin Michel for their steady encouragement during the difficult days in the last stages of this thesis.

Lastly, I wish to thank my family for their endless support. They are the major source of inspiration in my life. I acknowledge the greatest teachers, my parents, without whom I couldn't be at this position. I owe my wife for her patience, support and the times that she generously provided for my research and my 2 years old son, who taught me to be curious and to follow the inquisitive mind.

Dedication

To Leyla

&

Amirreza

Table of Contents

Abstract	ii
Acknowledgements	iii
Dedication	iv
Table of Contents	v
List of Tables	vii
List of Figures and Illustrations	viii
List of Symbols, Abbreviations and Nomenclature	xiv
CHAPTER ONE: INTRODUCTION	1
1.1 Research purpose	1
1.2 From simulation to seismic	2
1.2.1 Conventional oils	3
1.2.2 Heavy oils	5
1.2.3 Geomechanical impacts on seismic waves	7
1.3 Software used	7
1.4 Thesis contributions	8
1.5 Thesis structure	9
CHAPTER TWO: FROM RESERVOIR SIMULATION TO ELASTIC MODELLING	10
2.1 Reservoir simulation and history matching fundamentals	12
2.1.1 Reservoir simulation	12
2.1.2 History matching	18
2.2 Petro-elastic modelling	18
2.2.1 Gassmann’s equation	19
2.2.2 Fluid modulus	20
2.2.3 Matrix modulus	23
2.2.4 Dry frame modulus	25
2.2.5 Clay content	30
2.3 Seismic assisted history matching	31
2.4 Summary	34
CHAPTER THREE: FLUID SUBSTITUTION MODELS IN HEAVY OIL RESERVOIRS	36
3.1 Theoretical background	39
3.1.1 Shear modulus in heavy oil	39
3.1.2 Shear modulus modelling of heavy oil	41
3.1.3 Flash calculation	43
3.1.4 Viscoelastic fluid substitution schemes	45
3.2 Problem statement	46
3.3 Methodologies	47
3.3.1 Modelling bitumen and heavy oil	47
3.3.2 Forward modelling of elastic moduli	48
3.3.3 Compositional variation with temperature	52
3.3.4 Viscosity of the compositional fluid models	53

3.3.5 Elastic moduli of the oil and oil-rock system	53
3.4 Results and discussions	54
3.5 Summary	64
CHAPTER FOUR: STRESS SUBSTITUTION MODELS	66
4.1 Theoretical background	69
4.1.1 Production/Injection impacts on effective pressure	71
4.1.2 Velocity dependency to the stress state	78
4.1.3 Velocity calculation using the stiffness matrix	82
4.2 Numerical simulations and case studies	89
4.2.1 Model description	90
4.3 Geomechanics in thermal cases	97
4.4 Results and discussions	101
4.5 Summary	102
CHAPTER FIVE: CASE STUDY	105
5.1 Field and data description	106
5.2 Horizon interpretation and survey calibration	107
5.3 Post stack and pre-stack seismic inversion	110
5.3.1 Post-stack inversion	110
5.3.2 Pre-stack inversion	115
5.4 Reservoir modelling	117
5.4.1 Structural modelling	118
5.4.2 Property modelling	118
5.4.3 Geo-modelling in the case study	121
5.5 Reservoir simulation	124
5.6 Sim2Seis software development	126
5.6.1 Sim2Seis architecture for conventional fluids	127
5.6.2 Sim2Seis heavy oil version	139
5.7 Results and discussion	144
5.8 Summary	149
CHAPTER SIX: CONCLUSIONS	150
6.1 Conclusions	150
6.2 Suggestions for future works	152
6.3 Last words	153
Appendix A: Peng-Robinson equation of state	154
Appendix B: Coherent potential approximation method	157
Appendix C: Pedersen correlation for estimating viscosity	160
References	162

List of Tables

Table 2.1, Coefficients P^{mi} and Q^{mi} for four different inclusion shapes	28
Table 3.1, Parameters used	52

List of Figures and Illustrations

Figure 1.1, Work flow for conventional history matching (blue) and seismic assisted history matching (green). In the green path, the flow simulation results (pressure, temperature, saturations) is converted to acoustic/elastic moduli. The modelled moduli, then can be compared with acoustic/elastic moduli computed using seismic inversion.....	3
Figure 2.1, Rock physics bridges the parameters in reservoir domain (left) to the acoustic domain (right).	11
Figure 2.2, Model parameter matrix pattern for a 3×3×3 grid for a <i>two</i> phase flow, which is inverted to estimate pressure and fluid saturations at each grid cell at a single time step.	16
Figure 2.3, Model parameter matrix pattern for a 3×3×3 grid for a <i>three</i> phase flow, which is inverted to estimate pressure and fluid saturations at each grid cell at a single time step.	16
Figure 2.4, Pressure distribution in a water flood case, with no flow boundary condition.	17
Figure 2.5, Pressure distribution in the cells along the source (injector) and sink (producer). Each curve is for a constant time.	17
Figure 2.6, the workflow for seismic assisted history matching (modified from Carlson, 2006).....	32
Figure 3.1, Time lag between strain and stress in elastic, viscous and viscoelastic media. Note that both stress and strain are functions of time.	41
Figure 3.2, Modelled shear modulus along with Uvalde reservoir heavy oil data at 20°C, (after Batzle et al., 2006).	42
Figure 3.3, P-T phase diagram for heavy oil composition with C1 (0.15 moles), intermediate (0.1 moles) and heavy (0.75 moles) compounds. . At pressures above the bubble point line (lower solid line curve), the oil is a single liquid phase. As the pressure decreases at a constant temperature, the liquid expands until the pressure reaches the bubble point, at which a gas phase appears. The gas phase keeps growing until the pressure reaches the dew point (lower solid line curve), at which point the last liquid molecules evaporate. Dashed lines within the phase envelope denote the lines of a constant molar percentage of vapor.	48
Figure 3.4, Sensitivity of the shear wave velocity of the rock saturated with viscoelastic fluid, calculated using the double-porosity CPA method to different parameters. In the second row of this figure, α , G_0 and G_∞ are the arguments in the Cole-Cole empirical relation and are experimentally determined factor	

between 0 and 1, the real shear modulus measured at zero and infinite frequency, respectively. ϕ_c , S_w , S_g in the last row are the compliant porosity, water saturation and gas saturation, respectively. Data shown by black circles are from Uvalde field heavy oil at 20°C (Batzle and Hofmann, 2006).	50
Figure 3.5, Modelled elastic moduli along with Uvalde heavy oil data at 20°C (data from Batzle and Hofmann, 2006) for heavy oil and oil-saturated rock. The HS weighted average is 1/3 of upper HS bound plus 2/3 of the lower HS bound.	51
Figure 3.6, Gradual variations in the molar fraction of the components in the liquid phase of the heavy oil model at pressure of 1 atm, with 0.75 moles of heavy, 0.10 moles of intermediate and 0.15 moles of C1. Note that initially there is no light C1 component in the liquid phase, and by increasing temperature at constant pressure liquid loses more components.	55
Figure 3.7, Viscosity variations of the oil samples as a function of temperature at 1 atm.....	56
Figure 3.8, Cole-Cole fit for the heavy oil and bitumen models at 10 and 50°C.	56
Figure 3.9, Double-porosity CPA modelling of elastic moduli of rock saturated with two oil samples at 10 and 50°C.....	58
Figure 3.10, Attenuation curves for rock saturated with bitumen varying with temperature. At low frequencies (~ 1 Hz), there is an inverse proportionality between attenuation and temperature, where increasing temperature, decreases the attenuation. At very high frequencies ($\sim 10^{10}$ Hz), increasing temperature increases attenuation (direct proportionality). At medium frequencies ($\sim 10^4$ Hz), I observe that the maximum attenuation occurs at the intermediate temperature (130°C).....	59
Figure 3.11, Oil (first row) and rock oil (second row) storage modulus (first column) and Q (second column) of the bitumen sample.	61
Figure 3.12, Oil (first row) and rock oil (second row) shear storage modulus (first column) and Q (second column) of the heavy oil sample.....	62
Figure 4.1, Vertical effective stress changes (bar) after five years of production in two wells	74
Figure 4.2, Vertical effective stress changes (bar) after five years of production and injection.....	74
Figure 4.3, Horizontal effective stress changes (bar) after five years of production in wells.	75
Figure 4.4, Horizontal effective stress changes (bar) after five years of production and injection.....	75

Figure 4.5, Vertical displacement (meter) after five years of production in wells.	76
Figure 4.6, Vertical displacement (meter) after five years of production and injection. ..	76
Figure 4.7, Horizontal displacement (meter) after five years of production and injection.....	77
Figure 4.8, Horizontal displacement (meter) after five years of production and injection.....	77
Figure 4.9, Elements of stiffness tensor as functions of effective stress, modelled using MacBeth (2004) correlation (after Herwanger and Koutsabeloulis, 2011).....	80
Figure 4.10, Velocity as a function of effective pressure, in the vertical direction stress (after Herwanger and Koutsabeloulis, 2011).	85
Figure 4.11, V_p in VTI anisotropy sample in different directions. z points towards the velocity in vertical direction, where x and y are horizontal direction of the VTI medium (after Herwanger and Koutsabeloulis, 2011).	86
Figure 4.12, V_p and V_s in VTI anisotropy sample. Hydrostatic stress test (Left), Uniaxial strain test (middle) and Triaxial stress test (right) stress (after Herwanger and Koutsabeloulis, 2011).	87
Figure 4.13, V_p in orthorhombic sample in different directions (after Herwanger and Koutsabeloulis, 2011).	88
Figure 4.14, Velocity variation in different direction after increase of 10 bar in effective pressure for VTI shale sample.	89
Figure 4.15, Side view of the reservoir geometry, embedded in the geomechanical earth model.....	91
Figure 4.16, Pressure variations from 2010 to 2015, when only producer is open.	93
Figure 4.17, P wave velocity variations from 2010 to 2015, when only producer is open.	93
Figure 4.18, Pressure variations from 2010 to 2020, producer and injector are open.	94
Figure 4.19, P wave velocity variations from 2010 to 2020, producer and injector are open.	94
Figure 4.20, Grid plot shows the variation in effective stress in the vertical direction. Red color corresponds to increase in compressional stress (negative) while blue color shows reduction in compressional stress (positive). Top plot shows the variation of effective stress along the wells in the reservoir, where the bottom plot shows the variation of effective stress along the wells in the overburden.....	95

Figure 4.21, P-wave Velocity variations in principal directions from 2010 to 2015.....	96
Figure 4.22, P-wave Velocity variations in principal directions from 2010 to 2020.....	96
Figure 4.23, Effective stress variations during the water injection scenario. production starts at 2010, where injection starts at 2015. Both wells are open till 2020.....	100
Figure 4.24, Effective stress variations during the steam injection scenario. Production starts at 2010, where injection starts at 2015. Both wells are open till 2025.....	100
Figure 5.1, Location map of the primate field.	107
Figure 5.2, Statistical wavelet, correlation coefficients between synthetic seismogram and seismic trace at every well, and a sample seismic-well-tie.	108
Figure 5.3, Maximum cross-correlation between base and monitor survey.	109
Figure 5.4, Sweetness attribute of monitor survey.	109
Figure 5.5, Monitor vs. base survey (left), clustered data selected on the plot window (middle), is displayed in 3D view.	109
Figure 5.6, Model-based inversion (left) and band limited inversion (right) results on the base case seismic survey (2004).	111
Figure 5.7, Model based inversion (left) and band limited inversion (right) results on the monitor seismic survey (2009).....	111
Figure 5.8, Map of the band limited inversion results in base (upper row, 2004) and monitor (lower row, 2009) cases. Maps are representing the arithmetic mean of P-impedance in 10 millisecond window centered at the reservoir top (left column), 10 millisecond window bellow the reservoir top (middle column) and 20 millisecond window bellow the reservoir top (right column).....	112
Figure 5.9, Map of the model based inversion results in base (upper row, 2004) and monitor (lower row, 2009) cases. Maps are representing the arithmetic mean of P-impedance in 10 millisecond window centered at the reservoir top (left column), 10 millisecond window bellow the reservoir top (middle column) and 20 millisecond window bellow the reservoir top (right column).....	113
Figure 5.10, Square of the difference of band limited inversion results in monitor and base case, $(I_{p2009}-I_{p2004})^2$	114
Figure 5.11, Square of the difference of model based inversion results in monitor and base case, $(I_{p2009}-I_{p2004})^2$	114

Figure 5.12, Raw shot gather loaded for the prestack inversion.....	115
Figure 5.13, Processing workflow before pre-stack inversion.	116
Figure 5.14, Pre-stack inversion results on the base seismic survey (2004). The map shows arithmetic mean in window of 20 millisecond bellow the reservoir top.....	117
Figure 5.15, Stacking velocity cube, time horizons and well tops were used to create velocity model (1). Well tops and depth converted time horizon in depth domain (2). Defining reservoir boundary using sweetness attribute (3). Building grid skeleton (4). Defining model horizons (5). Adding vertical layers to the model (6). Rock type definition based on gamma ray and porosity values (7). Scaling up the logs into the grid cells (8). Variogram analysis (9). Cokriging rock types, porosity, permeability and saturation into the grid cells (10).	119
Figure 5.16, Simulation results in field level. Principle matching target is liquid production rate and the minimum bottom hole pressure at the wells is 2 bar. The wells are perforated in the entire reservoir interval. Note that the good match, other than reasonable static grid, fluid and rock properties is due to the fact that simulator is free to change the well head pressure. In case that pressure data is available this parameter is constrained and history matching process is more tedious.	126
Figure 5.17, Sim2Seis developed to convert simulation results to acoustic impedance.	128
Figure 5.18, Saturated elastic object in every grid cell is a function of matrix, dry frame and fluid elastic object.	129
Figure 5.19, Fluid elastic moduli object.	129
Figure 5.20, Sim2Seis inputs tab's interface; fluid elastic object.	130
Figure 5.21, It is possible to input grid as the input data.	130
Figure 5.22, Matrix elastic moduli object.	131
Figure 5.23, Calculations of the elastic moduli of the matrix; matrix elastic object.	132
Figure 5.24, Discrete facie input, for using in matrix elastic calculations.....	134
Figure 5.25, Calculations of the elastic moduli of the matrix for several facies units....	134
Figure 5.26, Dry frame work elastic moduli.	135
Figure 5.27, Calibration tab; dry frame elastic object.	135
Figure 5.28, Overriding input parameters (simulation, or intermediate properties).	136
Figure 5.29, Different outputs that a user can select to be created in the models pane. .	137

Figure 5.30, the log file generated by Sim2Seis for QC purposes.....	138
Figure 5.31, an structure designed for handling complex number algebra in C#.....	140
Figure 5.32, Viscoelastic Calibration tab.....	141
Figure 5.33, Loaded table will be automatically displayed on the corresponding plot section.	142
Figure 5.34, Loaded calibration data.	143
Figure 5.35, Modelled behaviour of the heavy oil.....	144
Figure 5.36, Comparison between the modelled (sim2seis) and real P-impedance (seismic inversion). The plot shows 0.55% correlation coefficient between data (x-axis) and model (y-axis). Colors show effective porosity.....	145
Figure 5.37, Property corrections include increasing permeability around the wells (a), co-kriging porosity with monitor acoustic impedance as secondary data (b) and dry frame modelling based on the different facies in every grid cells (c).....	147
Figure 5.38, Modelled P-impedance vs. inverted P-impedance in 2009 (monitor case). Colors show effective porosity.	148

List of Symbols, Abbreviations and Nomenclature

Symbol	Definition
A_d	Area perpendicular to flow in the d direction
n	Average number of contacts per grain
K_f	Bulk modulus of a fluid
K_{sat}	Bulk modulus of a fluid-saturated rock
K_{dry}	Bulk modulus of the dry rock or rock frame
K_m	Bulk modulus of the isotropic matrix
V_b	Bulk volume of the grid
P_c	Capillary pressure
C	Clay Content
V_p	Compressional wave velocity
P_c	Critical pressure
T_c	Critical temperature
Z	Depth gradient
C_{ij}	Elements of stiffness tensor
q_{lsc}	Flow rate of the fluid at standard condition
B_l	Formation volume factor
f	Frequency
f_i	Fugacity
z	Gas compressibility factor
i	Imaginary number
K_i	K-value for component i
L	Length
G''	Loss modulus
S_H	Maximum horizontal stress
S_h	Minimum horizontal stress
n	Mole number
S_v	Normal vertical stress
k_d	Permeability in d direction
P_l	Phase pressure
P_p	Pore pressure
P	Pressure
Q	Quality factor
P_r	Reduced pressure
T_r	Reduced temperature
k_{rl}	Relative permeability liquid
S	Saturation
G_{sat}	Shear modulus of a fluid-saturated rock
G_{dry}	Shear modulus of the dry rock or rock frame
V_s	Shear wave velocity
S	Shift parameter
R_s	Solution gas ratio
G'	Storage modulus
T	Temperature

t	Time
S_{ij}	Total or confining stress tensor
n_i	Unit vector element
V	Volume
x_i	Volume fraction
E	Young's modulus
ω	Angular frequency
α	Aspect ratio
$\langle \cdot \rangle$	Average
β	Biot's coefficient
Φ_c	Critical porosity
ρ	Density
λ_i	Eigen value
β_c	Flow term conversion factor
Φ_i	Fugacity coefficient
δ	Kronecker delta function
α_L	Linear thermal expansion coefficient
k_d	Permeability in d direction
ν	Poisson's ratio
\emptyset	Porosity
φ	Porosity
τ	Relaxation time
γ_l	Special gravity
ε	Strain
σ	Stress
σ_{ij}	Stress tensor's elements
μ	Viscosity

Chapter One: **Introduction**

1.1 Research purpose

Most of the petroleum reservoirs are currently either at their mature ages or have passed their production peaks. From reservoir management's point of view, it is vital to increase the recovery factor of these fields. This objective would be of significant interest if rather than collecting new data, one could add to the value of the already acquired data by mining the hidden features of them.

In terms of seismology, most of the reservoirs are experiencing time-lapse acquisition to monitor the position of current fluid fronts in porous media. In spite of the huge amount of available seismic data, there have been few practices to build dynamic reservoir models constrained by seismic response. Nonetheless, promising attempts have proved the unique features in seismic data as a diverse source of production data, in confining the reservoir model and mitigating risks of reservoir simulation forecasts (Huang et al., 1997; Arenas et al., 2001; Gosselin et al., 2003; Zou et al., 2006; Kazemi and Stephen, 2011).

With such an appealing motivation this thesis seeks to investigate the links between fluid flow in porous media and characteristics of propagating waves. Other than the general relationship, the goal is to decouple different production induced changes such as, change in the saturation, pressure, and temperature. This idea will be developed through rock physics research, coupled geomechanical-flow simulations and software programming, where necessary. The final goal in this thesis is to take advantage of seismic data as an exceptional confining criterion in reservoir history matching.

1.2 From simulation to seismic

Improvement of simulation results by integrating seismic data in reservoir history matching has received much attention in recent years. Reservoir simulation results are commonly validated with reservoir production data and bottom hole pressure history records to evaluate the behavior of the reservoir simulation model and the reliability of future forecasts. Seismic-assisted history matching (Gosselin et al., 2003) treats time-lapse seismic data similar to fluid production/pressure records. This approach constrains the dynamic reservoir model parameters to honor four-dimensional (4D) seismic surveys along with the well production history data. This ambitious goal is illustrated in figure 1.1. Conventional reservoir simulation as shown in this figure, starts with building a reservoir static model. This model is grounded on diverse data gathered from both the rock and fluid samples, and then populated within the structural grid based on seismic interpretations and depositional scenarios. In this figure, the blue path is the well-established practice which is currently common in industry and the green path is the seismic contribution. Seismic history matching can be implemented in three different levels as suggested by Gosselin et al., 2003. At the reservoir domain (pressure/saturation changes), elastic domain and seismic trace domain. In the current study I opt to perform history matching at elastic moduli level. In this context, I use Sim2Seis term to indicate conversion from simulation results to seismic impedances, even if strictly speaking Sim2Imp could be more appropriate term.

The spatially sparse well production data which are frequently sampled in time, can be integrated with seismic surveys which are densely acquired in space and are limited in time. Limited seismic time-lapse data can take advantage of abundant well production history data for effective interpretation in the course of reservoir production. Well behaviour in

turn, can be extended to the farther offsets by utilizing the seismic data and proper time-lapse interpretations.

1.2.1 Conventional oils

Many authors have worked on the integration of seismic time-lapse data in the simulation of conventional reservoirs (Huang et al., 1997; Arenas et al., 2001; Gosselin et al., 2003; Mezghani et al., 2004; Caers et al., 2006; Zou et al., 2006; Kazemi and Stephen, 2011). This integration is ultimately intended to alleviate the non-uniqueness solutions in the history matching process of fluid-flow simulations.

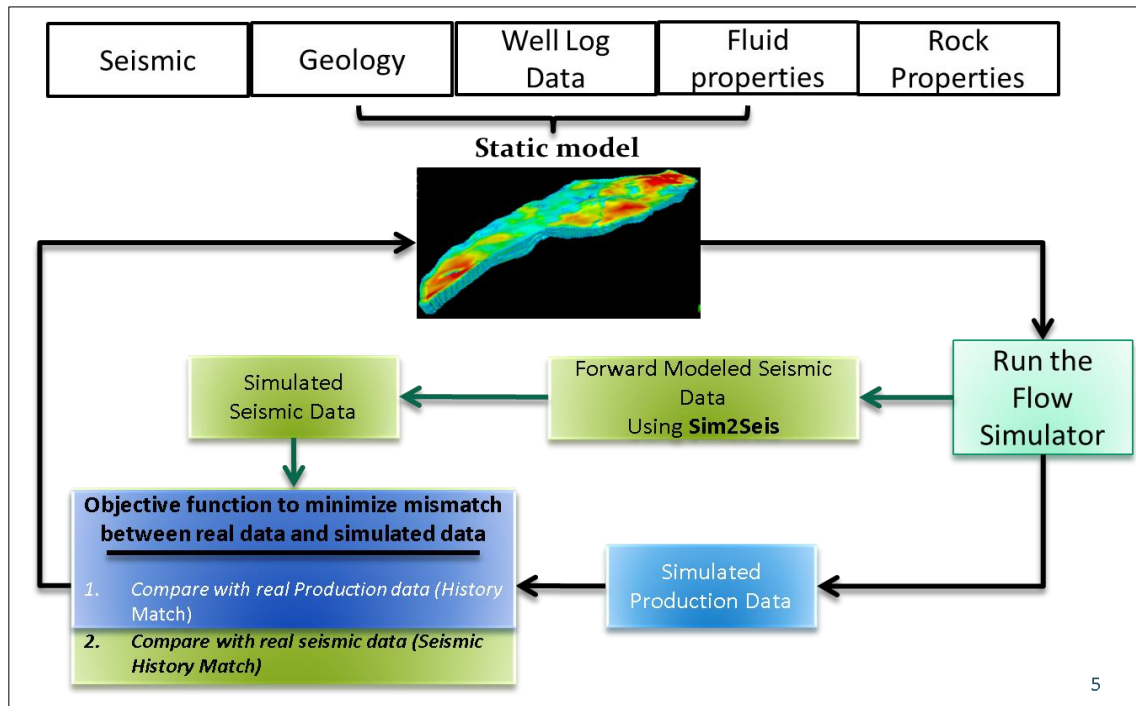


Figure 1.1, Work flow for conventional history matching (blue) and seismic assisted history matching (green). In the green path, the flow simulation results (pressure, temperature, saturations) is converted to acoustic/elastic moduli. The modelled moduli, then can be compared with acoustic/elastic moduli computed using seismic inversion.

A key step in the integration of seismic data and production records is the rock physics modelling that governs the domain change from the reservoir geodynamic model (e.g., pressure, temperature, saturation, porosity and gas-to-oil ratio) to the reservoir elastic properties. A well-known and commonly used method is Gassmann's equation (Gassmann, 1951; Smith et al., 2003). This method predicts that $G_{\text{sat}} = G_{\text{dry}}$, where G_{sat} is the shear modulus of a fluid-saturated rock and G_{dry} is the shear modulus of the dry rock.

Gassmann's equation expresses the bulk modulus of the rock saturated with fluid (K_{sat}), as a function of the bulk moduli of the fluid (K_f), the mineral materials or matrix (K_m) and the dry frame (K_{dry}). The fluid bulk modulus (K_f) can be calculated from either simulation results using calculated fluid compressibility (the inverse of the compressibility gives the bulk modulus) or Batzle and Wang (1992) formulations. The bulk modulus of the isotropic matrix (K_m) can be computed by estimating the effective bulk modulus of the mixture of the constituent minerals using the relations derived by Hashin and Shtrikman (1963). The Hashin-Shtrikman method in its original formulation gives the composite moduli for a two-phase material. However it can be further extended to apply for mixtures of more than two constituent minerals (Berryman, 1995).

The biggest uncertainty limiting the successful application of Gassmann's equations is the lack of knowledge of K_{dry} and G_{dry} . This complexity stems from the complexity of pore geometry and their dependence to the stress field. One can apply an estimated correlation between dry elastic moduli and rock porosity using laboratory measurements. Alternatively, there are many rock physics models that can be employed. One of the models that is able to include reservoir pressure depletion is the Hertz-Mindlin model (Mindlin,

1949). This theory proposes expressions for K_{dry} and G_{dry} as functions of effective pressure for unconsolidated sandstones.

Another method utilizes V_p and V_s data, which are estimated by the elastic inversion of available prestack data, in order to back calculate dry elastic moduli from Gassmann's equation. One can then employ these calculated values to generate saturated moduli for the time steps in which no real data are available, ignoring the influence of pore pressure reduction on the values of K_{dry} and G_{dry} .

1.2.2 Heavy oils

Although the portrayed fluid substitution scheme appears to be applicable in the case of rocks saturated with light oils, there are several serious flaws when heavy oil fills the pores. Due to their viscoelastic nature, heavy oils support shear stress, even at seismic frequencies and as a result, both the bulk and shear moduli of the fluid contribute to the velocity of heavy oil saturated rock. In addition Gassmann's equation is no longer valid at temperatures below approximately 60°C (Han et al., 2007a), because cold heavy oil reservoirs violate a number of assumptions used in developing Gassmann's equation.

Two of these assumptions are that the pore system must be connected and that fluids must be moveable (Smith et al., 2003). However, bitumen and extra heavy oil are sticky, tar-like, very viscous and sometimes even heavier than water, and must be heated or diluted with solvents in order to flow. Moreover, Gassmann's equation assumes that the framework of the rock is unchanged during the flow and this is not the case for unconsolidated sands in which the rock structure is altered and even partially produced along with heavy oil. The questionable results of employing Gassmann's equation in heavy oils have also been shown by Kato et al. (2008).

In addition to the inapplicability of Gassmann's fluid substitution equation, further complications arise due to the dependence of the elastic moduli of heavy oil on temperature and frequency (Nur et al., 1984; Eastwood, 1993; Schmitt, 1999; Batzle et al., 2006; Behura et al., 2007; Han et al., 2007a). The dependence on frequency leads to velocity dispersion and results in a discrepancy between the elastic moduli recorded in a laboratory and seismic frequencies. This adds more uncertainty to the results of Gassmann's equation for heavy oils; this is knowing the fact that Gassmann's equation has no explicit frequency variable and cannot account for velocity dispersion since it is essentially invalid for high frequencies.

Few researchers have suggested a practical fluid substitution modelling scheme in rocks saturated with viscoelastic fluids. Ciz and Shapiro (2007) proposed generalized Gassmann's equations in predicting the saturated bulk and shear moduli of rock samples saturated with heavy oils. Other methodologies have grounded their work on the effective elastic medium theory, which relates the elastic moduli of a composite medium to that of its constituents. For example, an approach suggested by Das and Batzle (2008), employs the Hashin-Shtrikman method of computing effective elastic moduli to set confining bounds for the elastic moduli of heavy oil saturated rock.

Gurevich et al. (2008) applied the self-consistent effective-medium method for composites, known as the coherent potential approximation (CPA), to estimate moduli of a composite system of oil and rock. Bown and Schmitt (2010) also employed the CPA method in carbonate rocks saturated with extra heavy oil using the De Ghetto viscosity model. Makarynska et al. (2010) enhanced the results of the CPA approach by using a double-porosity rock model and by introducing the compliant porosity term into CPA.

1.2.3 Geomechanical impacts on seismic waves

Disturbing reservoir equilibrium by production or injection will cause substantial consequences on the stress state of the reservoir. This stress disturbance has been historically ignored, partially due to the complexity of the coupled geomechanical-flow simulations.

Production from a reservoir decreases the pore pressure, which causes the rocks to undergo further overburden load since the supporting fluid has been expelled and has lost its opposing pressure. As the result the excess load of the overburden is transfer on the rock matrix. Such a stress state variations induced by pore pressure reduction, is usually highest around the wellbore and diffuses gradually away from the well. This heterogeneity in stress distribution will trigger a number of mechanisms in the reservoir, including decrease in porosity and permeability. Stress variations also can open or close fractures, activate faults, create subsidence and result in wellbore instabilities (Sayers, 2010). As the result of all these variations in the reservoir, time lapse seismic monitoring of the field should be capable of capturing the time shifts or amplitude changes not only within the reservoir, but also in the overburden.

In the current research, the stress impacts on seismic velocities have been studied and modelled in different reservoir production scenarios.

1.3 Software used

The following software has been used in this research:

Commercial software:

- Hampson-Russell, CGG (4D seismic calibration, seismic-well tie, pre/post stack inversion, reservoir characterisation)

- Petrel, Schlumberger (reservoir static modelling, geostatistical property modelling, seismic attribute analysis)
- Eclipse, Schlumberger (reservoir dynamic simulation)
- Visage, Schlumberger (geomechanical simulation)
- Petrel Reservoir Geomechanics, Schlumberger (coupled geomechanical-flow simulation)
- PVTi, Schlumberger (phase behaviour and reservoir fluid property modelling)
- WinProp, CMG (phase behaviour and reservoir fluid property modelling)

Programing:

- Matlab (fluid replacement modelling in viscoelastic fluid, velocity modelling as a function of variations in stress field)
- Visual studio, C# (developing the Sim2Seis codes)
- Ocean SDK for Petrel, Schlumberger (Integrating Sim2Seis into Petrel)

1.4 Thesis contributions

The following can be highlighted as the principal contributions of this thesis:

- Contributing the phase behaviour and compositional fluid properties in the fluid replacement models in viscoelastic fluids. The idea is to compare the impact of two opposing parameters, namely, GOR and temperature on viscosity.
- Characterizing thermal stress and resolving it from the pressure induced stress variations.
- Developing an industrial scale plugin to facilitate conversion of simulation results to seismic impedances.

1.5 Thesis structure

In this thesis, after the brief introduction in this chapter, chapter 2 is about the rock mechanical models that can be employed to bridge flow dynamic to the properties of saturated rock. In chapter 3, I extend the conventional fluid substitution model to the viscoelastic fluids. Furthermore, the frequency and temperature dependency of the fluids, and their imperative roles in fluid substitution analysis will be discussed. In chapter 4 we turn our attention to the alteration of stress states, which is another crucial mechanism in the seismic assisted history matching. I present different coupled geomechanical-flow simulations, to investigate wide variety of common scenarios including production, injection and thermal cases. In chapter 5, a case study is carried out to present the potential benefits of employing seismic assisted history matching approach. The case study is in heavy oil CHOPS reservoir. I implement the conventional fluid substitutional model, ignoring the geomechanical effects. The reason for this was lack of leak-off test data and viscoelastic lab measurements. Finally in chapter 6 I conclude this writing, followed by several recommendations for future research and developments.

Chapter Two: **From reservoir simulation to elastic modelling**

A key step in the integration of seismic data and reservoir production records is the rock physics modelling that governs the domain change from the reservoir geodynamic model (e.g., pressure, temperature, saturation, porosity and gas-to-oil ratio) to the reservoir elastic properties. This link has been schematically illustrated in figure (2.1). The ability of describing such a domain conversion enables us to address a very critical question, i.e., *“How do log measurements, core properties, and seismic data respond to the variations in reservoir conditions?”*

Provided that a reasonable answer is found to this question, then seismic data can be accounted for further constraining the reservoir history matching process.

Conventionally, the history matching ends up with establishing a consistent pressure, temperature and saturation condition. The measure for accuracy of such a condition is pressure data and fluid production rates, which have been recorded during the exploitation of the reservoir. Having an ability to convert the reservoir engineering data to seismic parameters, one can utilize 4-D seismic data to impose another measure for validating dynamic reservoir model. This seismic measure is quite unique in a sense that it is available not only at the wells but also between them.

Another application for described modelling ability in figure 2.1, is to predict 4-D seismic results at any upcoming date, without conducting acquisition operation. This might be an ambitious goal, however, its potential to assess the sensitivity of time lapse seismic should not be underestimated.

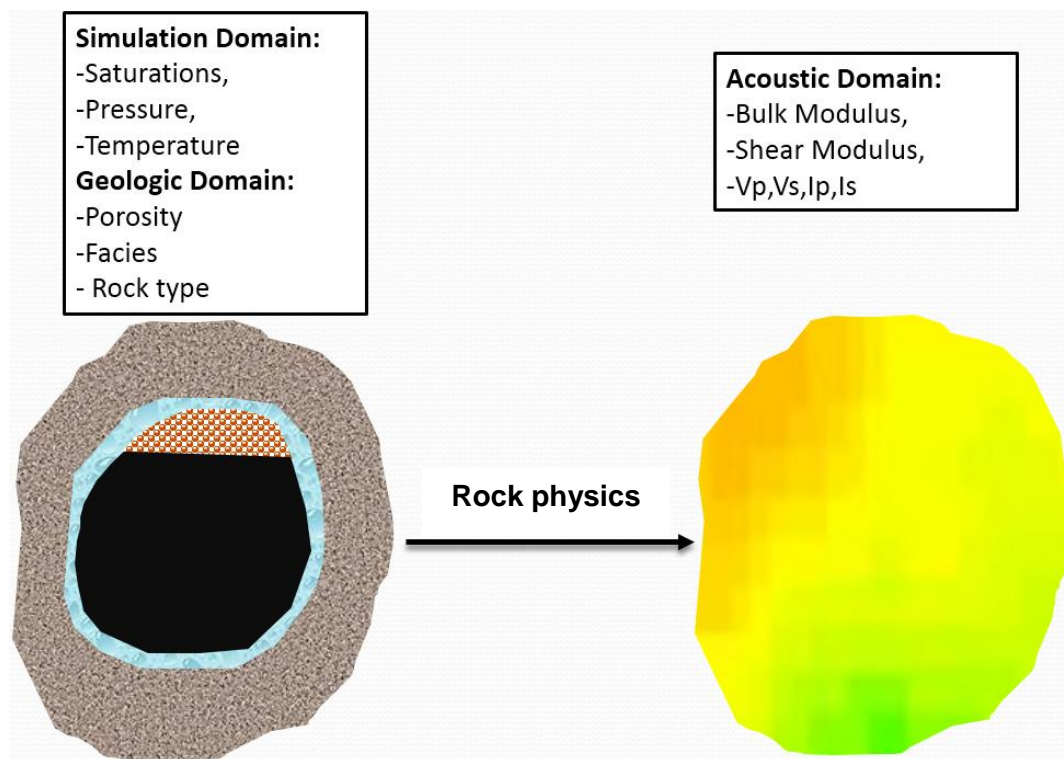


Figure 2.1, Rock physics bridges the parameters in reservoir domain (left) to the acoustic domain (right).

A legitimate concern in using rock physical models is the ability of decoupling different mechanisms that contribute in time-lapse seismic. During the reservoir production, saturation, pore pressure and temperature varies around the borehole and gradually diffuses through the reservoir to establish an equilibrium. Any of the varied parameters impacts the time-lapse seismic differently, depending on the rock and reservoir's condition. Their individual contributions on the time-lapse seismic signal may be along or in the opposite direction. Hence, the combined effect can be misleading and might represent a weakened or amplified time-lapse responses. Decoupling of the time-lapse drivers, is therefore a crucial step in the interpretation of time lapse responses; the objective that can only be achieved by a forward modelling based on a robust and reliable rock mechanical model.

Current chapter is an attempt to explain the rock physics' workflow required to convert reservoir properties to the acoustic moduli. I will also review and discuss the critical aspects of integrating 4D time-lapse data in the reservoir simulation.

2.1 Reservoir simulation and history matching fundamentals

2.1.1 Reservoir simulation

Two governing equations in reservoir simulation are Darcy's equation and the mass balance law. In fact in a multiphase flow system substituting Darcy's equation in the mass balance law, one will end up with the following form of diffusion equations for the three phases (oil, water, gas):

$$\begin{aligned}
& \frac{\partial}{\partial x} \left[\beta_c k_x A_x \frac{K_{ro}}{\mu_o B_o} \left(\frac{\partial p_o}{\partial x} - \gamma_o \frac{\partial Z}{\partial x} \right) \right] \Delta x \\
& + \frac{\partial}{\partial y} \left[\beta_c k_y A_y \frac{K_{ro}}{\mu_o B_o} \left(\frac{\partial p_o}{\partial y} - \gamma_o \frac{\partial Z}{\partial y} \right) \right] \Delta y \\
& + \frac{\partial}{\partial z} \left[\beta_c k_z A_z \frac{K_{ro}}{\mu_o B_o} \left(\frac{\partial p_o}{\partial z} - \gamma_o \frac{\partial Z}{\partial z} \right) \right] \Delta z \\
& = \frac{V_b}{\alpha_c} \frac{\partial}{\partial t} \left(\frac{\phi S_o}{B_o} \right) - q_{osc}
\end{aligned} \tag{2.1}$$

$$\begin{aligned}
& \frac{\partial}{\partial x} \left[\beta_c k_x A_x \frac{K_{rw}}{\mu_w B_w} \left(\frac{\partial p_w}{\partial x} - \gamma_w \frac{\partial Z}{\partial x} \right) \right] \Delta x \\
& + \frac{\partial}{\partial y} \left[\beta_c k_y A_y \frac{K_{rw}}{\mu_w B_w} \left(\frac{\partial p_w}{\partial y} - \gamma_w \frac{\partial Z}{\partial y} \right) \right] \Delta y \\
& + \frac{\partial}{\partial z} \left[\beta_c k_z A_z \frac{K_{rw}}{\mu_w B_w} \left(\frac{\partial p_w}{\partial z} - \gamma_w \frac{\partial Z}{\partial z} \right) \right] \Delta z \\
& = \frac{V_b}{\alpha_c} \frac{\partial}{\partial t} \left(\frac{\phi S_w}{B_w} \right) - q_{wsc}
\end{aligned} \tag{2.2}$$

$$\begin{aligned}
& \frac{\partial}{\partial x} \left[\beta_c k_x A_x \frac{K_{rg}}{\mu_g B_g} \left(\frac{\partial p_g}{\partial x} - \gamma_g \frac{\partial Z}{\partial x} \right) \right. \\
& \quad \left. + \beta_c k_x A_x \frac{K_{ro} R_s}{\mu_o B_o} \left(\frac{\partial p_o}{\partial x} - \gamma_o \frac{\partial Z}{\partial x} \right) \right] \Delta x \\
& \quad + \frac{\partial}{\partial y} \left[\beta_c k_y A_y \frac{K_{rg}}{\mu_g B_g} \left(\frac{\partial p_g}{\partial y} - \gamma_g \frac{\partial Z}{\partial y} \right) \right. \\
& \quad \left. + \beta_c k_y A_y \frac{K_{ro} R_s}{\mu_o B_o} \left(\frac{\partial p_o}{\partial y} - \gamma_o \frac{\partial Z}{\partial y} \right) \right] \Delta y \\
& \quad + \frac{\partial}{\partial z} \left[\beta_c k_z A_z \frac{K_{rg}}{\mu_g B_g} \left(\frac{\partial p_g}{\partial z} - \gamma_g \frac{\partial Z}{\partial z} \right) \right. \\
& \quad \left. + \beta_c k_z A_z \frac{K_{ro} R_s}{\mu_o B_o} \left(\frac{\partial p_o}{\partial z} - \gamma_o \frac{\partial Z}{\partial z} \right) \right] \Delta z \\
& = \frac{V_b}{\alpha_c} \frac{\partial}{\partial t} \left(\frac{\phi S_g}{B_g} + \frac{\phi R_s S_o}{B_o} \right) - q_{gsc}
\end{aligned} \tag{2.3}$$

where, ϕ is porosity,

β_c is transmissibility conversion factor equal to 1.127 (field)or 86.4e – 6 (metric) ,

V_b is the bulk volume of each grid cell,

α_c is volume conversion factor equal to 5.614583 (field)and 1 (metric),

$k_{x/y/z}$ is permeability in x/y/z direction,

$A_{x/y/z}$ is the cross-sectional area perpendicular to the flow in x/y/z direction,

k_{rl} is the relative permeability of phase l (oil, gas, water),

R_s is solution gas ratio,

μ_l is the viscosity of l (oil, gas, water),

B_l is the formation volume factor of phase l (oil, gas, water),

P_l is the phase pressure of phase l (oil, gas, water),

γ_l is the special gravity of phase l (oil, gas, water),

Z is the elevation,

$S_{x/y/z}$ is the fluid saturation,

q_{lsc} is the flow rate of the fluid (oil, water, gas) at standard condition.

The right hand side of equations is either source (injection) or sink (production) term with the positive and negative sign conventions, respectively.

In these three equations there are 6 unknowns, which are: P_o, P_w, P_g, S_o, S_w and S_g . We need three further equations in order to be able to solve this coupled system of equations.

One of the equations can be:

$$S_o + S_w + S_g = 1 \quad (2.4)$$

Two additional equations are needed to eliminate two of the unknowns:

$$P_{cow} = P_o - P_w = f(S_w) \quad (2.5)$$

$$P_{cgo} = P_g - P_o = f(S_g) \quad (2.6)$$

where P_c is the capillary pressure and is usually measured in standard core analysis as a function of saturation.

For detailed derivation and discretization process, refer to “Basic Applied Reservoir Simulation” by Ertekin et al. (2001). This system of equations results in a model known as black oil model which contains three phases; oil, gas and water. The assumption is that there is no mass transfer from one phase to another. Note that this system of equations is very nonlinear. In other words, relative permeability, porosity, solution gas ratio, viscosity,

formation volume factor, and special gravity are all functions of unknowns and should be updated at every single time step. This fact is potentially the source of many difficulties in the stability and convergence of the solutions. To tackle this issue in the linearization step, another law becomes inevitable which is the equation of state and governs pressure, temperature and volume states, based on the fluid properties.

The solution scheme adopted in reservoir simulation is the finite difference method. Solving this system of equations explicitly in time by using forward difference operator (using pressure at previous time steps), usually results in unstable predictions. Implicit solutions from the other hand, gives more stable solution at the cost of intensifying the computational operations. This is because at each step a system of equation must be solved by inversion of the model parameters' matrix, constructed by linearizing equations (2.1) through (2.3). Figure 2.2, illustrates a typical model parameter matrix pattern that is constructed for solving the system of equation at every single time step. This 54×54 matrix is for a two phase fluid flow and a simple $3 \times 3 \times 3$ grid block ($3 \times 3 \times 3 \times 2$ (oil, water) = 54). Figure 2.3, shows the 81×81 model parameter matrix pattern for the same grid geometry, with additional phase added to the system ($3 \times 3 \times 3 \times 3$ (gas, oil, water) = 81).

Figure 2.4, depicts a water flood case with a pair of injector (source) and producer (sink) wells, which has been simulated by solving the equation (2.1) through equation (2.6), with no flow boundary condition ($\nabla P = 0$). It is apparent in this figure that pressure builds up around the source and decreases around the sink. The plot in the figure 2.5, shows the numerical values for pressure decline/build up due to production/injection between the wells. Due to the high injection rate at source point, average pressure of the reservoir gradually increases compared to the initial pressure, as time proceeds.

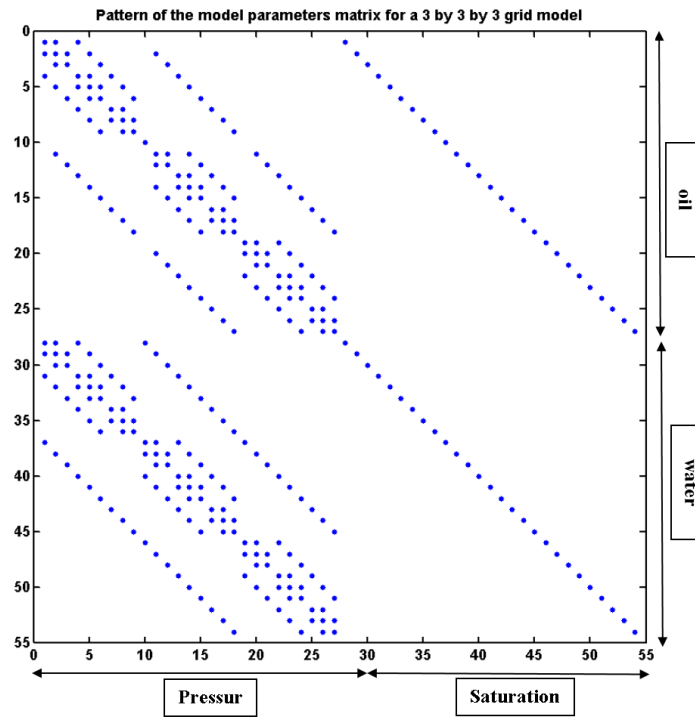


Figure 2.2, Model parameter matrix pattern for a $3 \times 3 \times 3$ grid for a *two* phase flow, which is inverted to estimate pressure and fluid saturations at each grid cell at a single time step.

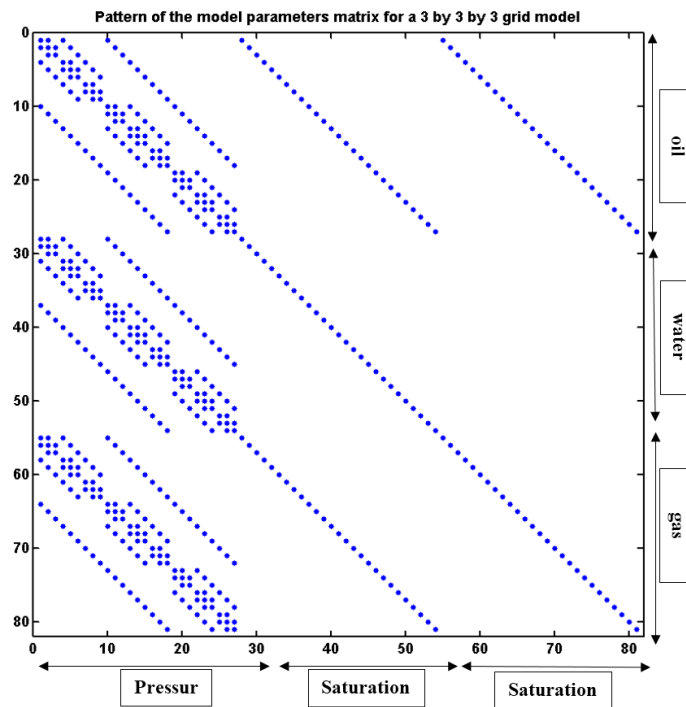


Figure 2.3, Model parameter matrix pattern for a $3 \times 3 \times 3$ grid for a *three* phase flow, which is inverted to estimate pressure and fluid saturations at each grid cell at a single time step.

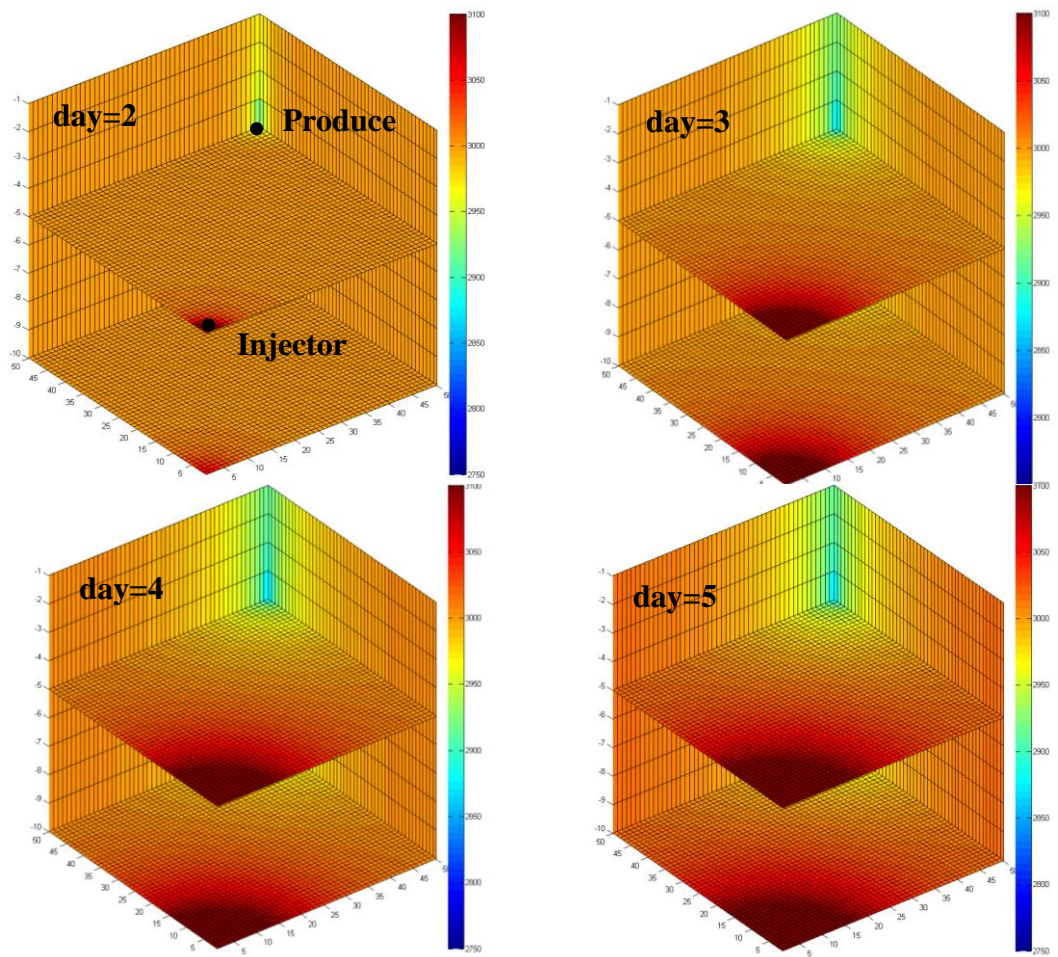


Figure 2.4, Pressure distribution in a water flood case, with no flow boundary condition.

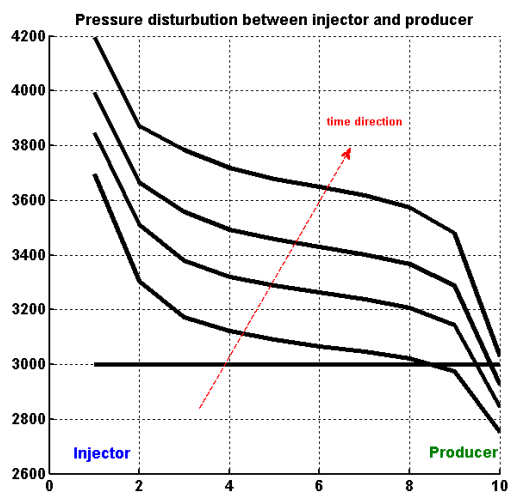


Figure 2.5, Pressure distribution in the cells along the source (injector) and sink (producer). Each curve is for a constant time.

2.1.2 History matching

The history matching process starts with running a simulation on the reservoir grid with certain rock and fluid properties. As discussed in the previous section, simulation is the process that brings all the information in a set of linear system of equations to come up with a solution to unknown parameters like pressure and saturation (also temperature in thermal cases). Measures of the validity of the model are liquid production rates and the pressure records at wells during the production. If calculated (simulated) rates of oil, gas and water match recorded rates and bottom-hole pressure, then the simulation is considered to be valid and hence reliable for future forecasts. If calculated parameters mismatch with the measured data, then the model parameters including grid properties, fluid properties, rock properties, initial and boundary conditions can be adjusted to come up with a closer similarity between the measured and calculated data.

This process of trying to make a reasonable agreement between the recorded reservoir production data and simulated data is known as history matching.

It should be noted that even if the problem of matching the history is an inverse problem, the solution for that is a forward modelling solution, due to the complexity and non-linearity of the diffusion equation.

2.2 Petro-elastic modelling

The disturbance in the initial state of the reservoir during its production, results in alteration of the initial state of elastic moduli of the rocks. In this section I will review the dominating rock mechanical relations that can be utilized to estimate the modified moduli of the rock, which undergoes production induced changes.

2.2.1 Gassmann's equation

A well-known and commonly used method to estimate the effects of saturation variations on elastic moduli is Gassmann's equation (Gassmann, 1951; Smith et al., 2003). This method predicts that $G_{sat} = G_{dry}$, where G_{sat} is the shear modulus of a fluid-saturated rock and G_{dry} is the shear modulus of the dry rock. Gassmann's equation expresses the bulk modulus of the rock saturated with fluid (K_{sat}), as a function of porosity (\emptyset), bulk modulus of the fluid (K_f), mineral materials or matrix (K_m) and the dry frame (K_{dry}):

$$K_{sat} = K_{dry} + \frac{(1 - \frac{K_{dry}}{K_m})^2}{\frac{\emptyset}{K_f} + \frac{1 - \emptyset}{K_m} - \frac{K_{dry}}{K_m^2}} \quad (2.7)$$

Another useful rearrangement of the Gassmann's equation is as follows (Mavko et al., 2009):

$$\frac{K_{sat}}{K_m - K_{sat}} = \frac{K_{dry}}{K_m - K_{dry}} + \frac{K_f}{\emptyset(K_m - K_f)} \quad (2.8)$$

Gassmann's equation is grounded on several important assumptions that should be considered in its application in different cases. For example Gassmann's equation cannot be applied to the non-uniform fluid saturations. It also assumes that the wave frequency is low and ignores attenuation and dispersion for high frequencies. Furthermore, it assumes that pores are connected and fluid in the pores comes to the equilibrium in the wave period time. This means that frequency is low enough that there is no pore-fluid movement across pore walls. In addition, Gassmann's equation also assumes that there is no chemical interaction between pore fluids and rock. The calculated K_{sat} and G_{sat} can be employed to compute the corresponding compressional and shear wave velocities:

$$V_p = \sqrt{\frac{K_{sat} + \frac{4}{3}G_{sat}}{\rho}} \quad (2.9)$$

$$V_s = \sqrt{\frac{G_{sat}}{\rho}} \quad (2.10)$$

where density can be estimated using the volume average between fluid and rock:

$$\rho_{sat} = \rho_m(1 - \phi) + \rho_w S_w \phi + \rho_{hc}(1 - S_w)\phi \quad (2.11)$$

where ρ_{sat} is the total density value, ρ_m is the density of the rock matrix, ρ_w is the density of brine water, ρ_{hc} is the density of hydrocarbons, ϕ is the porosity of the rock, and S_w is the water saturation.

2.2.2 Fluid modulus

The fluid bulk modulus (K_f) can be calculated from either simulation results using calculated fluid compressibility (the inverse of the compressibility gives the bulk modulus) or Batzle and Wang (1992) correlations. Batzle and Wang (1992), used the available correlations for compressibility measurements in reservoir engineering, and tried to make a connection between the compressibility and the measured elastic moduli data for a range of different fluids.

Once the individual fluid moduli are calculated, the Reuss harmonic averaging method can be employed for calculating the bulk modulus of the mixture of the fluids:

$$\frac{1}{K_f} = \frac{S_w}{K_w} + \frac{S_o}{K_o} + \frac{S_g}{K_g} \quad (2.12)$$

where, K_f is the effective bulk modulus of the fluid mixture. This equation is derived assuming the *iso-stress* state in different phases, where the applied stress, induces the same pore pressure for every single phase. This iso-stress condition is valid, provided that we

assume zero capillary pressure between immiscible phases. The situation that occurs when the fluid distribution is even and homogenous in the pores. The iso-stress condition is a reasonable assumption in the low frequency measurements and therefore Reuss average gives a realistic bulk modulus for the mixture of fluids.

An approximation for upper bound of fluid modulus can be estimated by the Voigt arithmetic averaging method:

$$K_f = S_w K_w + S_o K_o + S_g K_g \quad (2.13)$$

In this equation the assumption is that the medium goes through the *iso-strain* deformation. Reuss and Voigt method has been proved to be the upper and lower bounds of the elastic moduli, respectively (Hill, 1952). These bounds are also the limits for elastic moduli of the fluid mixtures. The difference between these two approaches has been discussed in more details in Mavko et al. (2009).

Needless to say that considering the fluid mixtures, the iso-stress assumption, is more tangible than iso-strain assumption behind the Voigt's method. This makes Reuss' bound a better candidate for calculation of elastic moduli of the mixture of fluid phases. However, this method becomes a bit tricky in the existence of gas phase. Since compressibility of the gas is $\sim 10^2$ times larger than liquids, it can be seen from equation (2.12) that K_f , is biased toward the introduction of gas. A small amount of gas will decrease K_f significantly and it is not possible to resolve the amount of gas saturation using Gassmann's equation. Brie et al. (1995) suggested a new mixing law which is capable to resolve different gas saturations better:

$$K_f = (K_{liquid} - K_g)(1 - S_g)^e + K_g \quad (2.14)$$

where e , can be determined empirically and usually is between 2 and 5.

Another limitation of equation (2.12) is that it cannot be employed in patchy saturation cases. In patchy saturations the iso-stress assumption will be violated in Reuss' relation. In addition, Gassmann's equation is not entirely valid since the pore pressure is not able to come to equilibrium in different patches within wave cycle. The patchy condition, is happening when the patch length is larger than a critical value, which is a function of wave frequency and fluid viscosity.

Strictly speaking, this critical length is:

$$L_c = \sqrt{\frac{K_f \kappa}{f \mu_f}} \quad (2.15)$$

where K_f , is the bulk modulus of the most viscous fluid, κ is permeability, f is seismic frequency and μ_f is the viscosity of the most viscous phase. for example for water ($\mu_f = 1$ centipoise = 0.001 Pa.s, and $K_f = 2.2 \text{ GPa}$) $L_c=10.42 \text{ cm}$, for $\kappa= 200 \text{ mD} = 200 * 9.869 * 10^{-13} \text{ m}^2$ and $f = 40 \text{ Hz}$. This means that induced pore pressure in seismic period (25 millisecond) will equilibrate in spatial space, smaller than 10.42 cm. If the dimension of fluid patches are greater than 10.42 cm, then they are referred as patchy saturation. Patchy saturation leads to higher compressional velocities and impedances and has no effect on shear velocities according to Mavko et al. (2009). In such a situation Johnson (2001) suggested to estimate K_f of the composites of two patches:

$$\frac{1}{K_f + \frac{4}{3}G} = \frac{S_1}{K_1 + \frac{4}{3}G} + \frac{S_2}{K_2 + \frac{4}{3}G} \quad (2.16)$$

where K_1 and K_2 are saturated bulk modulus computed from the Gassmann's equation, using K_{f1} (bulk modulus of first fluid) and K_{f2} (bulk modulus of second fluid), respectively. This method assumes the shear modulus (G) are equal in the entire medium, which is a reasonable assumption, irrespective of the pore fluid type.

Equation (2.16) is only valid for high enough frequencies:

$$\omega_c \propto D/L^2 \quad (2.17)$$

where D is slow wave diffusivity and L is size of patches.

2.2.3 Matrix modulus

The matrix modulus is essentially the effective modulus of the mixture of individual minerals. Values for elastic moduli of the minerals are already measured and are known. However, in addition to the minerals and their volume fractions, the geometric details of the constituent minerals are also required (Mavko et al., 2009). Since it is impractical to acquire such an information, we can define some bounding limits for the effective medium moduli of the mixture of minerals. Hill (1952) proved that upper and lower bounds for the effective elastic moduli are in fact Voigt and Reuss average, respectively. He suggested that the average of these two methods, can be used as the effective mixed elastic modulus.

Different effective medium theories, can also be employed for estimating the effective modulus of a rock matrix using its constituent mineral moduli. For example the bulk modulus of the isotropic matrix (K_m) can be computed by estimating the effective bulk modulus of the mixture of the constituent minerals using the relations derived by Hashin and Shtrikman (1963). The Hashin-Shtrikman method in its original formulation gives the composite moduli for a two-phase material. However it can be further extended to apply for mixtures of more than two constituent minerals (Berryman, 1995):

$$K^{HS-} = \Lambda(G_{min}) \quad (2.18)$$

$$K^{HS+} = \Lambda(G_{max})$$

$$\Lambda(z) = \left\langle \frac{1}{K_i + \frac{4}{3}z} \right\rangle^{-1} - \frac{4}{3}z$$

$$G^{HS+} = \Gamma(\zeta(K_{max}, G_{max}))$$

$$G^{HS-} = \Gamma(\zeta(K_{min}, G_{min}))$$

$$\Gamma(z) = \left\langle \frac{1}{G_i + z} \right\rangle^{-1} - z$$

$$\zeta(K, G) = \frac{G}{6} \left(\frac{9K + 8G}{K + 2G} \right)$$

where G_i and K_i are the shear moduli and bulk moduli of the constituents, respectively. The brackets $\langle . \rangle$ indicate a weighted average with respect to the volume fraction over the medium.

Hashin-Shtrikman gives a minimum and maximum bound for the elastic moduli and provides the narrowest possible bounding limits (Mavko et al., 2009). Arguably, the average of these two bounds can be considered as the corrected moduli.

This method can be employed to the mixtures of solid and liquid as well. In such a case the modified Hashin-Shtrikman (Mavko et al., 2009) scheme suggests the use of the concept of critical porosity, ϕ_c , to further narrow down the bounding limits, in the fluid-solid mixtures. The critical porosity (which is about 40% for sandstone) is the porosity above which solid falls apart and is not able to support loads anymore. In such a situation solid becomes suspension in the fluid phase and elastic moduli can be exactly calculated by the Reuss averaging since iso-stress conditions dominates. In the modified Hashin-

Shtrikman method, effective moduli of mineral plus ϕ_c percent of fluid is calculated using Hashin-Shtrikman and then it will be used instead of the fluid phase to be mixed with solid mineral in the Hashin-Shtrikman method again.

2.2.4 Dry frame modulus

The biggest uncertainty limiting the successful application of Gassmann's equations is the lack of knowledge of K_{dry} and G_{dry} . Dry frame moduli (K_{dry} and G_{dry}) refer to the moduli of the porous rock where the pores are empty. It worth mentioning that dry moduli is not necessarily measured on dry rock samples and drained sample can be used as well. The challenge is to ensure that the pore pressure remains unchanged during the test. This situation is similar to a rock filled with air at standard conditions (Mavko et al., 2009).

Experimental Correlation with porosity

One can apply an estimated correlation between dry elastic moduli and rock porosity using laboratory measurements. Murphy et al. (1993) suggested the following expressions between dry frame moduli of the rock and its porosity (ϕ), for the porosities smaller than 0.35:

$$K_{dry} = 38.18(1 - 3.39\phi + 1.95\phi^2) \quad (2.19)$$

$$G_{dry} = 42.65(1 - 3.48\phi + 2.19\phi^2) \quad (2.20)$$

and for the porosities greater than 0.35 they used:

$$K_{dry} = \exp(-62.60\phi + 22.58) \quad (2.21)$$

$$G_{dry} = 42.65(-62.60\phi + 22.73) \quad (2.22)$$

These correlations had been measured on the gas saturated and pure quartz sandstones, and should be calibrated for different rock types and saturating fluids.

Hertz-Mindlin

Alternatively, there are many rock physics models that can be employed. One of the models that is able to include reservoir pressure depletion is Hertz-Mindlin model (Mindlin, 1949). This theory proposes expressions for K_{dry} and G_{dry} as functions of effective pressure for unconsolidated sandstones:

$$\begin{aligned}
 K_{Dry} &= \left[\frac{\phi/\phi_c}{K_{HM} + \frac{4}{3}G_{HM}} + \frac{1 - \phi/\phi_c}{K + \frac{4}{3}G_{HM}} \right]^{-1} - \frac{4}{3}G_{HM}, \\
 G_{Dry} &= \left[\frac{\phi/\phi_c}{G_{HM} + Z} + \frac{1 - \phi/\phi_c}{G + Z} \right]^{-1} - Z, \\
 Z &= \frac{G_{HM}}{6} \left[\frac{9K_{HM} + 8G_{HM}}{K_{HM} + 2G_{HM}} \right];
 \end{aligned} \tag{2.23}$$

for $\phi \leq \phi_c$, and the following equation for $\phi \geq \phi_c$:

$$\begin{aligned}
 K_{Dry} &= \left[\frac{(1 - \phi)/(1 - \phi_c)}{K_{HM} + \frac{4}{3}G_{HM}} \right. \\
 &\quad \left. + \frac{(\phi - \phi_c)/(1 - \phi_c)}{\frac{4}{3}G_{HM}} \right]^{-1} - \frac{4}{3}G_{HM} \\
 G_{Dry} &= \left[\frac{(1 - \phi)/(1 - \phi_c)}{G_{HM} + Z} \right. \\
 &\quad \left. + \frac{(\phi - \phi_c)/(1 - \phi_c)}{Z} \right]^{-1} - Z
 \end{aligned} \tag{2.24}$$

where ϕ is porosity; ϕ_c is the critical porosity; K and G are the bulk and shear moduli of the mineral phase, respectively. K_{HM} and G_{HM} are calculated from the Hertz-Mindlin theory as:

$$K_{HM} = \left[\frac{G_m^2 n^2 (1 - \phi_c)^2}{18\pi^2 (1 - \nu)^2} P \right]^{\frac{1}{3}} \quad (2.25)$$

$$G_{HM} = \frac{5 - 4\nu}{5(2 - \nu)} \left[\frac{3G_m^2 n^2 (1 - \phi_c)^2}{2\pi^2 (1 - \nu)^2} P \right]^{\frac{1}{3}}$$

where P is the effective pressure, ν is the Poisson's ratio of the mineral phase calculated from K_m and G_m ; n is the average number of contacts per grain, and can be approximated by its relation with porosity (Dvorkin and Nur, 1996):

$$n = 20 - 34\phi + 14\phi^2 \quad (2.26)$$

Effective medium theories

Effective medium theories, are developed for finding a replacement medium such that its moduli are equal to the mixture of individual modulus of constituent materials. These methods are applicable in a wide range of applications, including metalloggy, composite materials, fracture mechanics and polymers. In rock physics, these methods are employed to calculate the elastic moduli of the rock matrix using their constituent minerals.

One can also consider pore space and its porosity, as one of the constituents of the rock frame, and hence the dry modulus of the rock can be computed in this manner. Kuster and Toksöz (1974) derived an approximation to calculate effective moduli for randomly distributed inclusions embedded in a medium (Berryman, 1980b):

$$(K_{KT}^* - K_m) \frac{K_m + \frac{4}{3} G_m}{K_{KT}^* + \frac{4}{3} G_m} = \sum_{i=1}^N x_i (K_i - K_m) P^{mi} \quad (2.27)$$

$$(G_{KT}^* - G_m) \frac{G_m + \zeta_m}{G_{KT}^* + \zeta_m} = \sum_{i=1}^N x_i (G_i - G_m) Q^{mi} \quad (2.28)$$

where P^{mi} , and Q^{mi} are parameters describing the effect of an inclusion of material i in the background medium (Table 2.1). In this table $\zeta = \frac{G}{6} (\frac{9K+8G}{K+2G})$, $\gamma = G (\frac{3K+G}{3K+7G})$, m and i refer to the matrix and inclusions, respectively. α is the crack aspect ratio, x_i is the volume fraction of the inclusion component and K_{KT}^* and G_{KT}^* , are effective medium moduli that can be worked out explicitly using equations 2.27 and 2.28.

Table 2.1, Coefficients P^{mi} and Q^{mi} for four different inclusion shapes

Inclusion shape	P^{mi}	Q^{mi}
Spheres	$\frac{K_m + \frac{4}{3} G_m}{K_i + \frac{4}{3} G_m}$	$\frac{G_m + \zeta_m}{G_i + \zeta_m}$
Needles	$\frac{K_m + G_m + \frac{1}{3} G_i}{K_i + G_m + \frac{1}{3} G_i}$	$\frac{1}{5} \left(\frac{4G_m}{G_m + G_i} + 2 \frac{G_m + \gamma_m}{G_i + \gamma_m} + \frac{K_i + \frac{4}{3} G_m}{K_m + G_m + \frac{1}{3} G_i} \right)$
Discs	$\frac{K_m + \frac{4}{3} G_i}{K_i + \frac{4}{3} G_i}$	$\frac{G_m + \zeta_i}{G_i + \zeta_i}$
Penny cracks	$\frac{K_m + \frac{4}{3} G_i}{K_i + \frac{1}{3} G_i + \pi \alpha \beta_m}$	$\frac{1}{5} \left(\frac{8G_m}{4G_i + \pi \alpha (G_m + 2\beta_m)} + 2 \frac{K_i + \frac{2}{3} (G_i + G_m)}{K_i + \frac{4}{3} G_i + \pi \alpha \beta_m} \right)$

Another practical method to come up with a reasonable estimation of dry frame moduli is to use the Hashin-Shtrikman method. In this method two components, namely the matrix component $(1 - \phi)$ and pore component (ϕ) with 0 moduli can be combined to come up with an elastic moduli of the dry frame.

The coherent potential approximation (CPA) method is an iterative for estimating effective-medium moduli of a composite system and can be employed as an alternative to Hashin-Shtrikman. This method has been discussed in details in Appendix (B).

Calculation of dry moduli using V_p and V_s data

Another method for calculating dry modulus, utilizes available V_p and V_s data (e.g., V_p and V_s calculated from seismic inversion) , in order to back calculate dry elastic moduli using inverse form of Gassmann's equation:

$$K_{dry} = \frac{K_{sat} \left(\frac{\phi K_m}{K_f} + 1 - \phi \right) - K_m}{\frac{\phi K_m}{K_f} + \frac{K_{sat}}{K_m} - 1 - \phi} \quad (2.29)$$

One can then employ these calculated values to generate saturated moduli for the time steps in which no data are available, ignoring the influence of pore pressure reduction on the values of K_{dry} and G_{dry} . This equation should be used with care in small porosities, since it can result in erratic and unstable results. The sensitivity of this method to the small porosity can be readily seen from equation (2.29).

Calculation using V_p or V_s only

There is a method explained by Lee (2003) originated by Gregory (1976) for calculation of dry frame moduli when V_p is only available. One can rewrite Gassmann's equation in the following form:

$$a\beta^2 + b\beta + c = 0 \quad (2.30)$$

where $\beta = 1 - \frac{k_{dry}}{k_m} = \frac{\Delta V_{pore}}{\Delta V_{bulk}}$ is defined as Biot's coefficient, at constant pressure. Also

$$a = \frac{4}{3}G_m k_f \quad (2.31)$$

$$b = \rho k_f V_p^2 - (k_m + \frac{4}{3}G_m)[k_f(1 + \phi - k_m\phi)]$$

$$c = \phi(k_f - k_m)(-\rho V_p^2 + k_m + \frac{4}{3}G_m)$$

By solving equation (2.30) for β one can, then calculate k_{dry} using $\beta = 1 - k_{dry}/k_m$.

G_{dry} can be derived by the following formula (Krief et al., 1990):

$$G_{dry} = G_m(1 - \beta) \quad (2.32)$$

In cases where there is only V_s data, one can use equation (2.10), and considering that $G_{dry} = G_{sat}$, equation (2.32) can be employed to calculate β and k_{dry} , as the result.

Another useful method for calculating V_p , in case that V_s is not measured was given by Mavko et al. (1995). They showed that V_p can be reasonably estimated by:

$$\frac{M_{sat}}{M_m - M_{sat}} \approx \frac{M_{dry}}{M_m - M_{dry}} + \frac{M_f}{\phi(M_m - M_f)} \quad (2.33)$$

where $M = \rho V_p^2$ which is equal to $K + 4/3G$.

2.2.5 Clay content

Assuming that clay minerals are part of the matrix, and knowing that they are more compressible, then we expect reduction of the velocities by increasing clay content. The effect of clays on seismic properties also depends on the position of clay particles in the rock and on the clay type (Wang, 2001). Usually introducing a small amount of clay will reduce the velocity significantly. The reason is that tiny clays will fill small spaces between

grain contacts and reduce the stiffness of the contact points. Han et al. (1986), reported an experimental correlation which relates the sand stone velocity to its porosity and clay content:

$$V = V_0 - a\phi - bC \quad (2.34)$$

where a, b are experimentally measured factors, ϕ is porosity and C is the clay content. This expression can be used for both P and S wave velocities, and obviously shows a decreasing trend in velocity with increasing porosity or clay content.

2.3 Seismic assisted history matching

In section 2.1, I explained the results that are expected from the reservoir simulators, and in section 2.2 the rock mechanical formulations were summarized, those which can be employed to convert dynamic simulation results to the bulk and shear modulus of the saturated rock. In this section I discuss the practical aspects and considerations in seismic assisted history matching process.

Figure 2.6, illustrates the typical approach for seismic assisted history matching workflow. Note that steps 1 through 4 (Carlson, 2006) is the conventional history matching scheme, which already is well-established in the industry.

At every step, there are different parameters that can be treated as matching parameters, where one can play around to end up with a good match between measured and simulated data. We should emphasize that these parameters can be treated as matching parameters, only if their true values are unknown or have been measured with a certain degree of uncertainty.

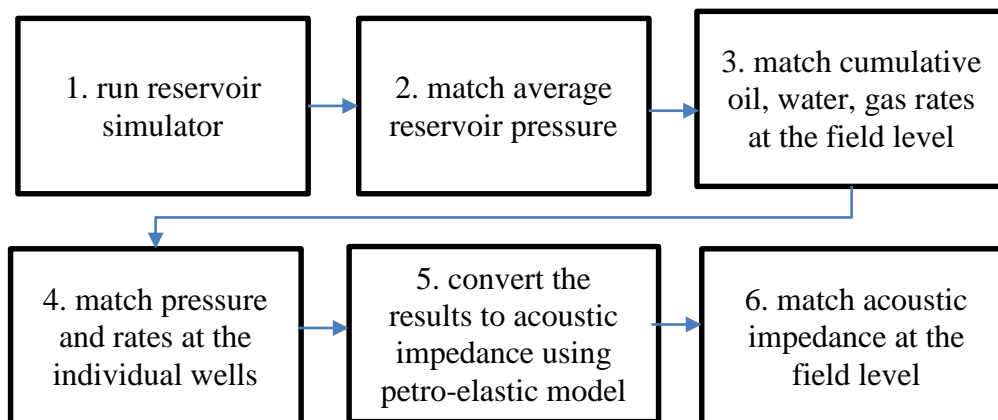


Figure 2.6, the workflow for seismic assisted history matching (modified from Carlson, 2006).

The followings are some considerations required at every steps:

1. The reservoir model should be capable of producing enough liquids. That's what we need to verify before step 1. A quick material balance check should be run to see if it has enough fluid in place. Also initial and boundary conditions should be checked to confirm that the reservoir has enough driving energy to produce.

2. To match the reservoir pressure at the field level, the initial condition as well as boundary condition, can be considered as the matching parameters. Also rock compressibility dictates the ability of rock to expand or shrink due to pore pressure changes, and directly influence the pore pressure. We should be careful in the sense that the rock compressibility that we are referring here (pore volume changes with pore pressure changes) is different from rock compressibility that is typical in seismology (bulk volume changes with confining pressure changes).

3. Two dominating parameters in this step are hydrocarbons fluid properties, and relative permeability curves.

4. Skin factor, bottom-hole pressure and local rock permeability can be treated as matching parameters.

5. This steps was discussed in the previous sections in details.

6. In this step the seismic impedance calculated from seismic inversion is compared with seismic impedance computed using described rock physic models. This step requires two distinct level of matching to be considered. First is the case that the simulation results are reasonably correct (which we never know!). In such a case we need to play around with the post simulation parameters. The main unknown parameter is K_{dry} to be tuned. The second case is when after running step 5 we end up with surprises! In other word we see a drastic local, or global differences between the modelled acoustic impedance and the acoustic impedance from seismic data. Even if it is disappointing to observe discrepancies, it should be recalled that identifying and resolving these mismatches is the main goal during the process of *seismic assisted history matching*, in order to improve our understanding from the reservoir model.

Depending on the fluid substitution modelling used, the matching parameters are different in this step. Generally the amount of gas produced in the reservoir has major influence on the petro-elastic modelling. Hence, PVT properties of the hydrocarbon can be treated as the matching parameter.

Adding a constant value (negative in injection or positive in production) to the K_{dry} might shift the data to the true values, if the stress induced corrections has not been

considered in the modelling. From the other hand, adding clay content will reduce the velocities, depending on porosity.

Local discrepancies are quite interesting to be observed, since they might be an indicator of reservoir compartmentalization or faults or subtle lithological variation like increasing shale content which reduces the seismic velocity.

2.4 Summary

The goal in this chapter was to portray the workflow required for conversion of reservoir engineering domain to acoustic impedance domain. I started off by defining reservoir simulation and governing equations in this domain. Next, the history matching process was briefly discussed. The history matching process starts with running a simulation on the reservoir grid with certain rock and fluid properties. Conventionally, the history matching ends up with establishing a consistent pressure, temperature and saturation condition. The measure for validity of such a condition is pressure data and fluid production rates, which have been recorded during the exploitation of the reservoir.

Having an ability to convert the reservoir engineering data to seismic parameters, one can utilize 4-D seismic data to impose another measure of dynamic reservoir model validation. The discussions in this chapter were followed to explain the rock physics' workflow needed to convert reservoir properties to the acoustic moduli. The main focus was on conventional flow, where Gassmann's equation can be employed for calculating saturated bulk moduli from different rock and fluid properties. In this regard, different techniques in estimation of bulk moduli of matrix, dry framework and fluid were discussed. In addition I pointed out the impact of clay contents and also rock properties in case of

patchy saturated. Finally in the last section I explained practical considerations and techniques required in seismic assisted history matching workflow.

Chapter Three: **Fluid substitution models in heavy oil reservoirs**

Fluid substitution models were discussed for conventional reservoirs in the previous chapter in detail. Although the portrayed fluid substitution scheme appears to be applicable in the case of rocks saturated with light oils, there are several serious flaws when heavy oil fills the pores. Due to their viscoelastic nature, heavy oils support shear stress, even at seismic frequencies and as a result, both the bulk and shear moduli of the fluid contribute to the velocity of heavy oil saturated rock. Furthermore, Gassmann's equation is no longer valid at temperatures below approximately 60°C (Han et al., 2007a), because cold heavy oil reservoirs violate a number of assumptions used in developing Gassmann's equation. One of the assumptions is that the pore system must be connected and the other is that fluids must be moveable (Smith et al., 2003). However, bitumen and extra heavy oil are sticky, tar-like, very viscous and sometimes even heavier than water, and must be heated or diluted with solvents in order to flow. Moreover, Gassmann's equation assumes that the framework of the rock is unchanged during the flow and this is not quite the case for unconsolidated sands in which the rock structure is altered and even partially produced along with heavy oil. The questionable results of employing Gassmann's equation in heavy oils have also been shown by Kato et al. (2008).

In addition to the inapplicability of Gassmann's fluid substitution equation, further complications arise from the dependence of the elastic moduli of heavy oil on temperature and frequency (Nur et al., 1984; Eastwood, 1993; Schmitt, 1999; Batzle et al., 2006; Behura et al., 2007; Han et al., 2007a). The dependence on frequency leads to velocity dispersion and results in a discrepancy between the elastic moduli recorded in a laboratory and seismic frequencies. This adds more uncertainty to the results of Gassmann's equation for heavy

oils; this is knowing the fact that Gassmann's equation has no explicit frequency variable and cannot account for velocity dispersion since it is essentially invalid for high frequencies.

Few researchers have suggested a practical fluid substitution modelling scheme in rocks saturated with viscoelastic fluids. Ciz and Shapiro (2007) proposed generalized Gassmann's equations in predicting the saturated bulk and shear moduli of rock samples saturated with heavy oils. Other methodologies have based their work on the effective elastic medium theory, which relates the elastic moduli of a composite medium to that of its constituents. For example, an approach suggested by Das and Batzle (2008), employs the Hashin-Shtrikman method of computing effective elastic moduli to set confining bounds for the elastic moduli of heavy oil saturated rock.

Gurevich et al., (2008) applied the self-consistent effective-medium method for composites, known as the coherent potential approximation (CPA), to estimate moduli of a composite system of oil and rock. Bown and Schmitt (2010) also employed the CPA method in carbonate rocks saturated with extra heavy oil using the De Ghetto viscosity model. Makarynska et al. (2010) enhanced the results of the CPA approach by using a double-porosity rock model and by introducing the compliant porosity term into CPA approach.

One of the goals of the current study is the examination of different aspects of proposed viscoelastic fluid substitution models. The objective is the establishment of a practical method for converting dynamic reservoir properties to elastic moduli in heavy oil reservoirs, where insufficient laboratory data cast doubt on the modelling results. We use

a more realistic fluid model by taking into account the fluid's composition in the viscosity calculations.

I modelled two different oil compositions introduced into the pores as the saturating fluid: a single-component dead oil (oil with no light component and dissolved gas) sample with a heavy molecular weight to represent bitumen and a compositional live oil sample with lighter components as representative of heavy oil. The selection of the lighter fluid sample worked towards illustrating the influence of compositional variations of the saturating fluid with temperature variations on the elastic moduli of the saturated rock. Our modelling strategy makes use of fluid phase behavior as an output of reservoir simulation in the forward elastic modelling of thermal reservoirs. One should make provisions that this scheme is unfit for solvent-assisted recovery, which is a common scenario in heavy oil recovery. In such a case, asphaltene precipitation normally occurs and solid phase deposits left in the pores are required to be considered in the calculations of the elastic moduli.

The current study put the heavier bitumen sample to use for the comparison between elastic moduli of the rocks when they are saturated with heavy oils of varying viscosities.

The capabilities for temperature prediction and consequently, viscosity estimation are of significant practical consequence in increasing the total recovery factor in thermal reservoirs. It is always challenging to determine if injected steam has reached the entire reservoir or if there are some unreachable and untouched regions. In addition, controlling the growth pattern of the steam chamber has a direct impact on total recovery. I demonstrate how the unique relationship among the frequency, the temperature and the elastic moduli for a rock saturated with a particular fluid can provide a workflow for determining the temperature at different locations of the reservoir.

For validation purposes during this study, Uvalde heavy oil data measured by Batzle et al. (2006) were used as obtained from the literature (Behura et al., 2007; Das and Batzle, 2008; Gurevich et al., 2008; Makarynska et al., 2010).

3.1 Theoretical background

3.1.1 Shear modulus in heavy oil

Heavy oils exhibit properties of both viscous fluids and elastic materials. As an elastic material, the linear elasticity is described by Hooke's law, which presents the stress as a linear function of strain:

$$\sigma = M\varepsilon \quad (3.1)$$

where σ , M and ε are the stress, elastic modulus and strain, respectively.

As a viscous fluid, heavy oils obey the stress-strain relationship in which stress is proportional to the strain rate:

$$\sigma = \mu\dot{\varepsilon} \quad (3.2)$$

with μ being the viscosity, and $\dot{\varepsilon} = d\varepsilon/dt$.

According to (3.1) and (3.2), stress and strain are in phase and 90° out of phase for the elastic and viscous materials, respectively. We suppose that σ is a sinusoidal function of time:

$$\sigma(t) = \sigma_{max}\sin(\omega t) \quad (3.3)$$

the strain response of a linearly viscoelastic material then lags the stress by phase angle δ :

$$\varepsilon(t) = \varepsilon_{max}\sin(\omega t - \delta) \quad (3.4)$$

For heavy oils, strain is out of phase with stress varying from 0 to 90° , depending on the temperature and measuring frequency. Lakes (2009) gives a more detailed discussion. Figure 3.1 reveals the stress and strain response with different time lags. In elastic

materials, the resultant strain is in phase with the applied stress (no phase lag) and removal of the load, yields the simultaneous removal of strain (i.e. the elastic body has no memory).

In viscous fluids, the resultant strain depends on the history of the applied stress (90° phase lag) and there is no recovery from the deformation upon the removal of the load (i.e. the viscous body has an extreme memory). In other words, the strain at the present time, $\varepsilon(t)$, depends on the stress history up to the present time, t , and not just to the stress at time t , which occurs for ideal elastic materials.

In heavy oils, we expect to observe a combination of both elastic and viscous materials. That is to say, these materials have a certain memory and depending on their viscoelastic nature, can be partially affected by their past, as time (or frequency) comes into play.

The complex shear modulus (G) of heavy oils is given by the in-phase elastic component (or storage modulus, G') and the out-of-phase viscous component (or loss modulus, G''):

$$G = G'(\omega) + G''(\omega)i \quad (3.5)$$

where G' and G'' are the abilities of a medium to store energy elastically and to dissipate energy as a fluid, respectively. Attenuation is then defined as the reciprocal of the quality factor, Q (Q is the measure of energy loss per cycle according to Sheriff and Geldart (1995)):

$$Q^{-1} = \frac{G''}{G'} = \tan \delta \quad (3.6)$$

where δ is the phase lag between the stress and the resultant strain.

For a purely elastic medium in which there is no imaginary elastic moduli component, there is no energy loss; therefore, $Q^{-1} = 0$. In such a case, there is no phase lag between the stress and the resultant strain and all the energy is stored. For viscous fluids, $Q^{-1} = \infty$,

which denotes that all the energy is dissipated and no energy is stored ($\delta = 90$). For a detailed explanation of these relationships, please refer to Ferry (1980).

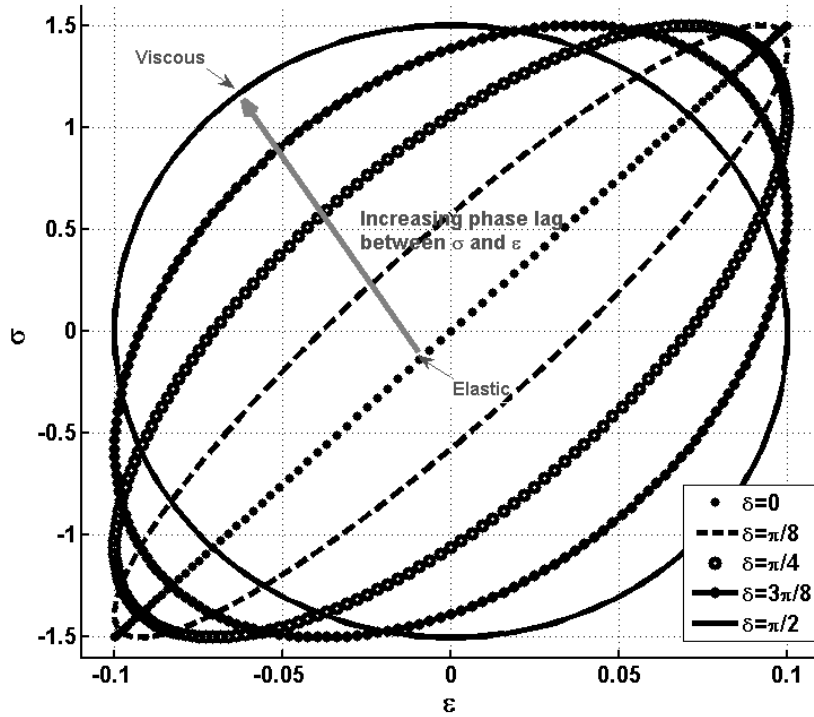


Figure 3.1, Time lag between strain and stress in elastic, viscous and viscoelastic media. Note that both stress and strain are functions of time.

3.1.2 Shear modulus modelling of heavy oil

The simplest model used to describe complex shear moduli as a function of angular frequency (ω), is the Maxwell model:

$$G(\omega) = \frac{G_{\infty}}{1 - (i\omega\tau)^{-1}} \quad (3.7)$$

where $i = \sqrt{-1}$, $\tau = \eta/G_{\infty}$ is the relaxation time, η is the viscosity of the oil, and G_{∞} is the real shear modulus at infinite frequency. Batzle et al. (2006) and Behura et al. (2007)

noted that the frequency dependency described by the Maxwell model is stronger than can be observed in experimental data (Gurevich et al., 2008).

Batzle et al. (2006) used the Cole-Cole empirical relationship to approximate the frequency-dependent shear modulus of the heavy oil:

$$G(\omega) = G_{\infty} - \frac{G_{\infty} - G_0}{1 + (i\omega\tau)^{\alpha}} \quad (3.8)$$

where $\tau = \eta / (G_{\infty} - G_0)$, G_0 is the real shear modulus at zero frequency, and α is an experimentally determined factor between 0 and 1.

Figure 3.2 shows the modelled storage modulus generated from the Maxwell model, the Cole-Cole correlation and measured data at 20°C.

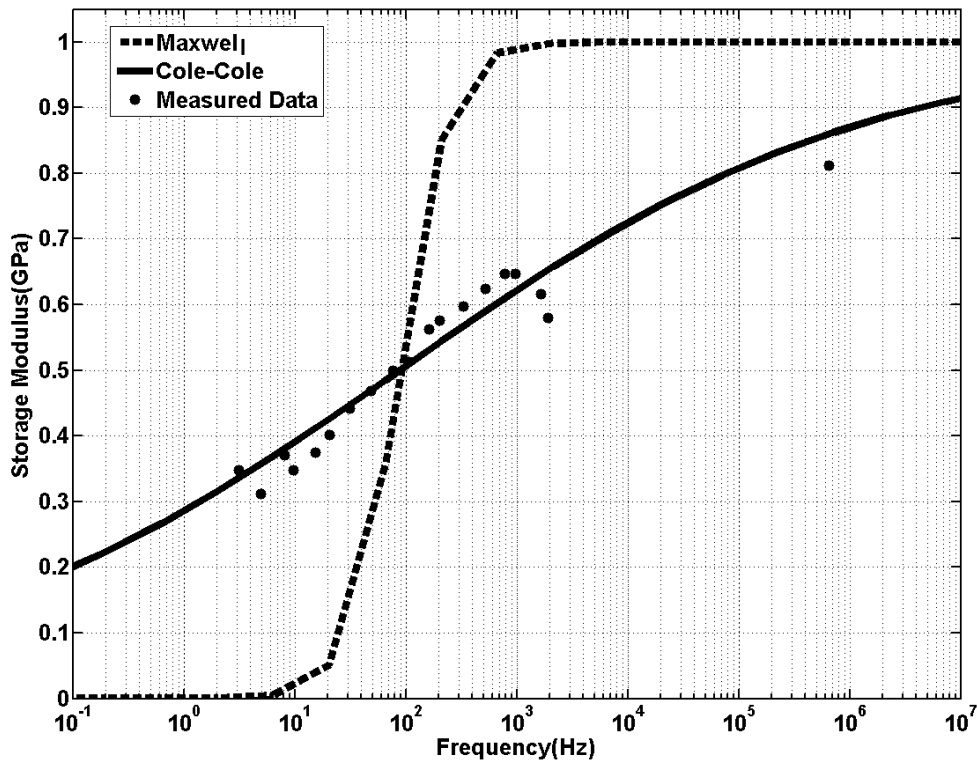


Figure 3.2, Modelled shear modulus along with Uvalde reservoir heavy oil data at 20°C, (after Batzle et al., 2006).

3.1.3 Flash calculation

It is apparent in equation (3.8) that the shear modulus of the heavy oil depends on its viscosity. In order to have a reasonable estimate of the oil viscosity, we need to characterize the phase behavior of the fluids as a function of the pressure, the temperature and the oil composition. The flash calculation is a common tool in reservoir engineering to calculate the number of phases and their compositions, given the pressure, temperature and composition of the fluid. For example, if we carry out a flash calculation on a fluid with a known composition and a fixed pressure and temperature (P_I, T_I), we can figure out the number of moles in the liquid and gas phases, once equilibrium is reached. In addition, the composition of each phase can be determined. When the compositions of all the phases are known, we can work out the properties (e.g., viscosity) of each phase. The required four steps for flash calculation are as follows:

1. An estimate of the equilibrium ratio, K_i , which is the number of moles of a component in vapor (Y_i) to that in liquid (X_i), is made using a reasonable equation, such as Wilson's equation (1968) that is based on the pressure (P), temperature (T), molecular fraction and properties of each component:

$$K_i = \left(\frac{P_{ci}}{P}\right) \exp[5.37(1 + \omega_i) \left(1 - \frac{T_{ci}}{T}\right)] \quad (3.9)$$

where ω is the acentric factor. T_c and P_c are the absolute critical temperature and pressure, respectively, which can be found in chemical tables showing the properties of pure compounds. The subscript i refers to the i^{th} component in the fluid system.

2. An ordinary flash calculation is done in order to calculate the compositional fractions in the liquid and vapor phases, using the total material balance and the material balance for each component:

$$n^L + n^V = 1 \quad (3.10)$$

$$X_i n^L + Y_i n^V = Z_i \quad (3.11)$$

where n^L and n^V are the moles of the liquid and vapor, respectively. X_i , Y_i and Z_i are the mole fractions of the i^{th} component in the liquid, vapor and mixture, respectively.

The idea in an ordinary flash calculation is that we guess n^L (or n^V) and verify if equation (3.11) is satisfied for all the components based on the guessed n^L and n^V and the values of k_i estimated in step 1.

3. Using the calculated X_i and Y_i from step 2, the cubic equation of state for liquid and vapor is set up as a function of the compressibility factor (Appendix A). All three roots are calculated with the maximum and minimum roots corresponding to the vapor and liquid compressibility factors, respectively.

4. In the equilibrium state, the fugacity (the measure of the tendency of a fluid to transform from one phase to another) of each component should be equal throughout all the phases in a heterogeneous system. We calculate the fugacity (Appendix A) of each component to compare the values in the liquid and vapor phases. If they are equal, the correct composition fractions are X_i and Y_i ; otherwise, the K_i values are updated, and we start over from step 2.

For a detailed explanation of flash calculation using an equation of state, please refer to Danesh (1998).

3.1.4 Viscoelastic fluid substitution schemes

Effective-medium theories estimate an equivalent model of a medium based on the properties and relative fractions of its constituents. These theories can be applied to the composites of heavy oil and rock knowing their fractions. By calculating the shear modulus of heavy oil from equation (3.8) and knowing the shear properties of the rock, we can combine the moduli to come up with the effective oil-rock composite properties. The Hashin-Shtrikman (HS) method, for example, gives the narrowest bounds for the elastic modulus of such a composite. Ideally, given the exact geometrical details for the isotropic constituents, this would give the precise value of the moduli of the composite medium. The averages of the upper and lower HS bounds are reasonable for the composite of the different minerals, since their geometrical details are more or less similar. However, for the fluid and rock system, not only does the separation between constraining bounds broaden, but the average may not be a good choice to represent the effective elastic properties of the fluid and rock system. As a matter of fact the bounds become quite separated, and we lose some of the predictive value (Mavko et al., 2009).

CPA is an alternative method to find the equivalent properties of the composite between the HS bounds (Berryman, 1980b, 1995). This technique is known to provide reliable estimates of the frame moduli of heterogeneous materials (Ogushwitz, 1985). The poor results of the CPA method for a single-porosity system can be improved with the use of a double-porosity system, considering cracks in the rocks (Makarynska et al., 2010). Appendix B provides the details for the CPA method.

3.2 Problem statement

The goal of this study is the establishment of a viscoelastic fluid substitution model where the rock is saturated with different fluids. We seek to establish a framework for viscoelastic fluid substitution first and then to investigate the corresponding practical aspects of this framework.

Two heavy oil samples were numerically modelled to represent heavy oil (live oil) and bitumen (dead oil; oil with no light component and dissolved gas), where the viscosity of bitumen was intended to be much higher than that of heavy oil. We selected a heavy oil sample to study the compositional variation effects on elastic moduli with temperature, whereas modelling of bitumen was done to compare elastic moduli of the rock saturated by two distinct viscoelastic fluids with different ranges of viscosities. In other words, we are looking for answers to the following two questions:

1. How would the elastic moduli of the oil-rock system change, given gas liberation with increasing temperature?
2. How would the elastic moduli of the oil-rock system change if the saturating heavy oil fluid was replaced by a more viscous fluid?

The heavy oil sample was modelled to address the first question; and the bitumen sample, in comparison to the heavy oil sample, was utilized to answer the second question. This comparison related the elastic moduli of a particular oil-rock system with a certain temperature and frequency. Hence, temperature can be predicted when frequency and elastic moduli are known.

3.3 Methodologies

3.3.1 Modelling bitumen and heavy oil

In order to determine the phase behavior of a hydrocarbon mixture, we need to have its chemical composition and the prevailing temperature and pressure. Although a reservoir fluid can be composed of thousands of compounds, a full description of fluid by identifying all its constituents may not be possible, and reservoir oil is commonly described by discrete hydrocarbon components (Danesh, 1998).

The bitumen model in this study has a single component with a molecular weight of 600 Kg/Kgmol. The other fluid model, i.e., the heavy oil fluid, is composed of three hydrocarbon constituents: C1, intermediate and heavy components. The behavior of the heavy oil fluid depends on the properties of these three components and their molar fractions. We assume that the molecular weight for the C1, intermediate and heavy components are 16 Kg/Kgmol (equivalent to methane), 96 Kg/Kgmol (typical for heavy components) and 359 Kg/Kgmol (typical for ultra-heavy components), with molar fractions of 0.15, 0.10 and 0.75, respectively. The largest fraction is that of heavy components, so that the behavior of the mixture is similar to that of heavy oils.

Figure 3.3 shows the phase behavior of the heavy oil fluid sample at different temperatures and pressures. At pressures above the bubble point line (lower solid line), the oil is a single liquid phase. As the pressure decreases at a constant temperature, the liquid expands until the pressure reaches the bubble point, at which a gas phase appears. The gas phase keeps growing until the pressure reaches the dew point (lower solid line), at which point the last liquid molecules evaporate. In figure 3.3, the dashed lines within the phase envelope denote the lines of a constant molar percentage of vapor. This phase diagram

displays all the characteristics of a heavy oil fluid composition: a wide interval of temperatures with a high critical temperature ($\approx 565^\circ\text{C}$), a relatively narrow range of pressures with a low critical pressure of 2308 kPa and a low cricondenbar (the maximum pressure at which two phases can coexist) of 6000 kPa. The large variations in the temperature and pressure of the oil above the bubble point releases very little gas, which is evident from the dashed lines.

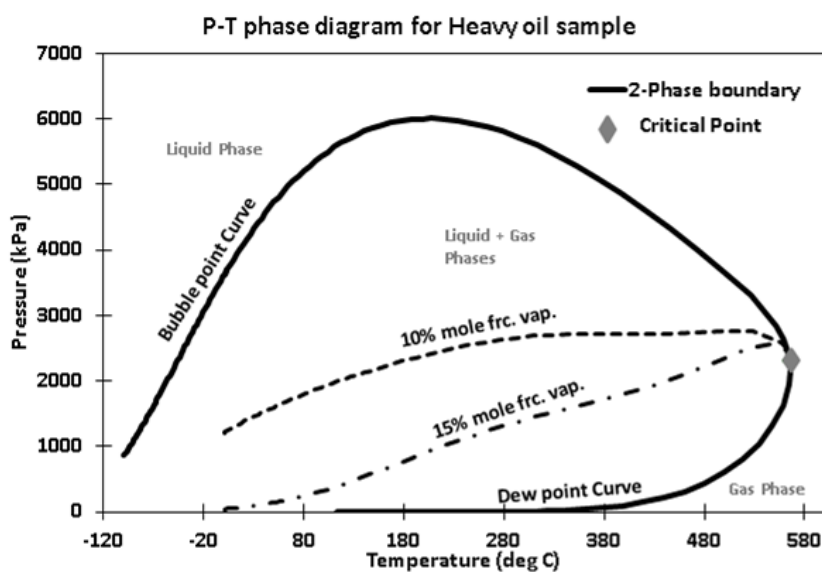


Figure 3.3, P-T phase diagram for heavy oil composition with C1 (0.15 moles), intermediate (0.1 moles) and heavy (0.75 moles) compounds. . At pressures above the bubble point line (lower solid line curve), the oil is a single liquid phase. As the pressure decreases at a constant temperature, the liquid expands until the pressure reaches the bubble point, at which a gas phase appears. The gas phase keeps growing until the pressure reaches the dew point (lower solid line curve), at which point the last liquid molecules evaporate. Dashed lines within the phase envelope denote the lines of a constant molar percentage of vapor.

3.3.2 Forward modelling of elastic moduli

In order to forward model the elastic moduli of heavy oil saturated rock using an effective-medium method, we needed to have good estimates of several unknown

parameters that are involved in the computation of either the fluid moduli or the effective-medium moduli of the fluid and rock system.

The unknown parameters can be estimated by fitting the modelled moduli to the real data. However, since the limited measured data never represent the entire reservoir, they cannot be employed for the modelling of the all reservoir grids with certainty. To assess the confidence in the modelling results, a sensitivity analysis of the model parameter is a crucial step in establishing the uncertain parameters for uncertainty analysis. Figure 3.4 illustrates the sensitivity of the forward modelling of the shear wave velocity using the double-porosity CPA method (Appendix B). In this figure, the base values for the unknown parameters are the numbers in the legends having an asterisk, and all of them are equally weighted. Each panel illustrates the sensitivity of the shear wave velocity with respect to the parameter denoted in the title, where the rest of the unknowns are left with the base values. As is illustrated in this figure, introducing the compliant porosity has significantly improved the shear velocity model; however it is still strongly controlled by the aspect ratio of the compliant porosity. The rest of the fluid and rock parameters are less sensitive in the modelling. The panels showing the sensitivity of the results to the water and gas saturations are shown in order to represent how these fluids influence the shear velocity, and they are usually considered as known parameters in a reservoir model.

In practice, the numerous unknown parameters should be set to have the best match with real data (Figure 3.5). The parameters used to generate this figure are presented in Table 3.1. Some of these parameters may be measured directly in laboratories; however, most of them can be set practically by fitting the more commonly available data, such as velocity.

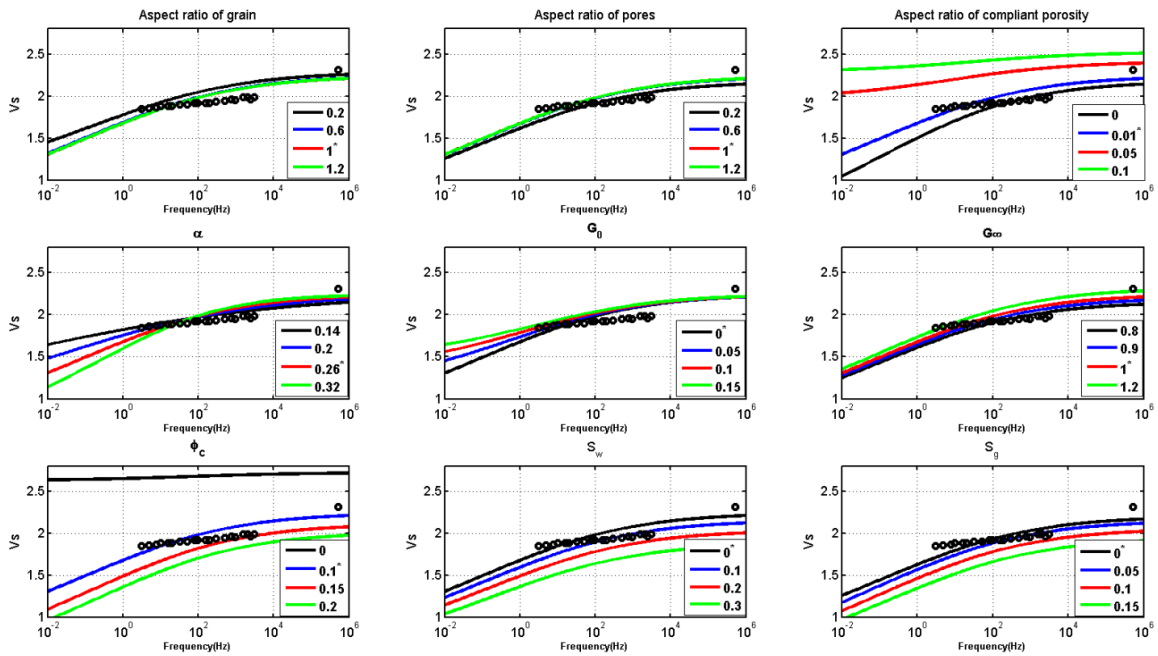


Figure 3.4, Sensitivity of the shear wave velocity of the rock saturated with viscoelastic fluid, calculated using the double-porosity CPA method to different parameters. In the second row of this figure, α , G_0 and G_∞ are the arguments in the Cole-Cole empirical relation and are experimentally determined factor between 0 and 1, the real shear modulus measured at zero and infinite frequency, respectively. ϕ_c , S_w , S_g in the last row are the compliant porosity, water saturation and gas saturation, respectively. Data shown by black circles are from Uvalde field heavy oil at 20°C (Batzle and Hofmann, 2006).

Once all the parameters are set, we can apply them to calculate the elastic moduli at every grid point of the reservoir model; even though, it might be optimistic to rely on a laboratory sample to represent the rock of an entire reservoir. This procedure is similar to a common practice in reservoir engineering history matching, where one tries to tune the equation of state or the relative permeability curves based on limited fluid or core samples to subsequently apply the tuned equations to the whole reservoir.

The unknown elastic parameters can be seen as adaptable scaling factors in assessing the match between the measured lab data and the modelled elastic moduli or, on a bigger

scale, between the synthetic seismic model and the time-lapse seismic records over the course of reservoir production. These uncertain parameters in elastic matching are in addition to the huge number of unknown parameters in reservoir history matching; however, their diverse nature makes them unique constraining parameters.

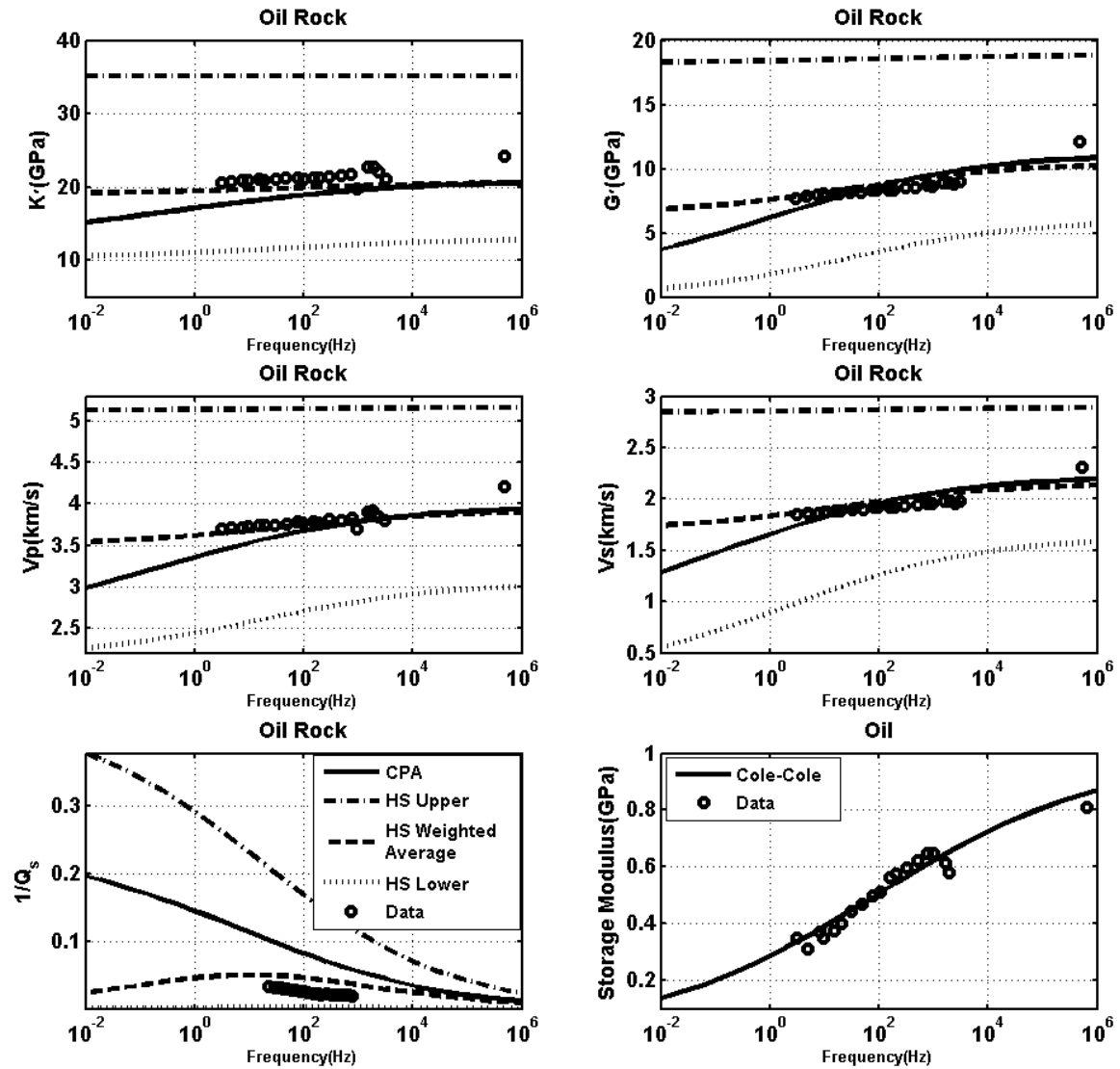


Figure 3.5, Modelled elastic moduli along with Uvalde heavy oil data at 20°C (data from Batzle and Hofmann, 2006) for heavy oil and oil-saturated rock. The HS weighted average is 1/3 of upper HS bound plus 2/3 of the lower HS bound.

Table 3.1, Parameters used

Matrix Bulk Modulus	45 GPa
Matrix Shear Modulus	30 GPa
Matrix Density	2.7 g/cc
Oil Bulk Modulus	2.03 GPa
Water Bulk Modulus	2.15 GPa
G_0	0
G_∞	1
α	0.261
Porosity, ϕ	0.25
Compliant Porosity, ϕ_c	0.05
Aspect Ratio[Matrix, ϕ , ϕ_c]	[1, 1,0.01]
Water Saturation, S_w	10 %
Gas Saturation, S_g	0 %

3.3.3 Compositional variation with temperature

To study the elastic properties of the two fluid models, we needed to evaluate their viscosities at various temperatures. In order to make a reasonable estimate of viscosity, it is necessary to find the molar fractions of each phase at certain temperatures and pressures. The next step is the determination of the composition of the liquid phase, since the available components and their fractions dictate the viscosity of the liquid.

I performed flash calculations at standard pressure (1 atm) on the heavy oil sample to determine the fractional composition of the fluid phase at different temperatures. The 3-parameter Peng-Robinson equation of state (Jhaveri and Youngren, 1988) was employed in the flash calculations (Appendix A).

In order to have phase equilibrium at a certain pressure and temperature, the volume should be variable according to the equation of state ($pV = znRT$). Increasing temperature leads to the release of dissolved gas and expansion of the free gas. Assuming an

approximately constant pore volume, the extra gas will be produced and as a result, the composition of the remaining fluid will then be different.

3.3.4 Viscosity of the compositional fluid models

Unlike the well-developed theoretical models for gas viscosities, there is no definitive model for the viscosity of liquids, which is mainly due to the complex momentum transfer mechanisms in liquids (Viswanath et al., 2007). Nonetheless, for practical purposes, empirical correlations can usually be calibrated to predict the viscosity as a function of pressure and temperature for different fluid compositions.

I employed Pedersen's correlation for calculating viscosities at each temperature (Appendix C). Pedersen et al. (1984) described the complete details of the method to predict the viscosity of hydrocarbons. The average absolute deviations of viscosities derived by this correlation are generally less than the other generalized methods available in the literature and are about 12%, 8% and 5%, respectively for pure fluids, binary mixtures and crude oils (Viswanath et al., 2007).

3.3.5 Elastic moduli of the oil and oil-rock system

In order to model the elastic moduli of a rock saturated with viscoelastic fluid, the first step was to obtain a reasonable estimate of the fluid elastic moduli. I calculated the oil shear moduli according to the prediction of the Cole-Cole correlation, using the α , G_0 and G_∞ values shown in Table 1. In order to come up with a reasonable estimate of the bulk moduli of the fluid, I used CPA method to combine the elastic moduli of oil, gas and water. Here, the implicit assumption is that saturation distribution is homogenous in porous media. However, in heterogeneous fluid saturations in which fluid distribution is patchy

and patches are larger than wavelength, the effective properties of the rock vary depending on the saturation pattern, and CPA method will not provide the reliable results.

Once the shear elastic modulus of the oil is estimated, the moduli of rock-oil system could be computed by the effective-medium theory of composite materials. The elastic moduli of the oil and rock composite is derived using the CPA method in a double-porosity system and the corresponding attenuation ($1/Q$) was then estimated by equation (3.6).

For the calculation of the velocities, we needed to have an estimate of the densities of the fluids, in addition to the shear and bulk moduli. The mass and volume is calculated using the outputs of the flash calculation: X_i (molar fraction of each component in the liquid phase) and n^L (number of moles in liquid phase) and the compressibility factor. The mass is equal to the sum of $X_i M_i$ for all components, where X_i and M_i are the molar fraction and the molecular weight of the i^{th} component, respectively. The volume is computed by the equation of state at a given temperature and pressure by using n^L and the calculated compressibility factor for the liquid phase.

3.4 Results and discussions

In order to focus on the viscoelastic properties of the liquid phase, we assumed that the light components turn to vapor and leave the liquid phase with increasing temperature. As a result, the remaining liquid composition provided the compositional input for the flash calculations in the next step (i.e. next temperature). Figure 3.6 shows the gradual change in the liquid phase composition with increasing temperature. As is apparent in this figure, most of the C1 component is in the vapor phase at the initial state of pressure and temperature. The liquid phase loses light components continuously with increasing temperature, until it effectively becomes one component at around 130°C.

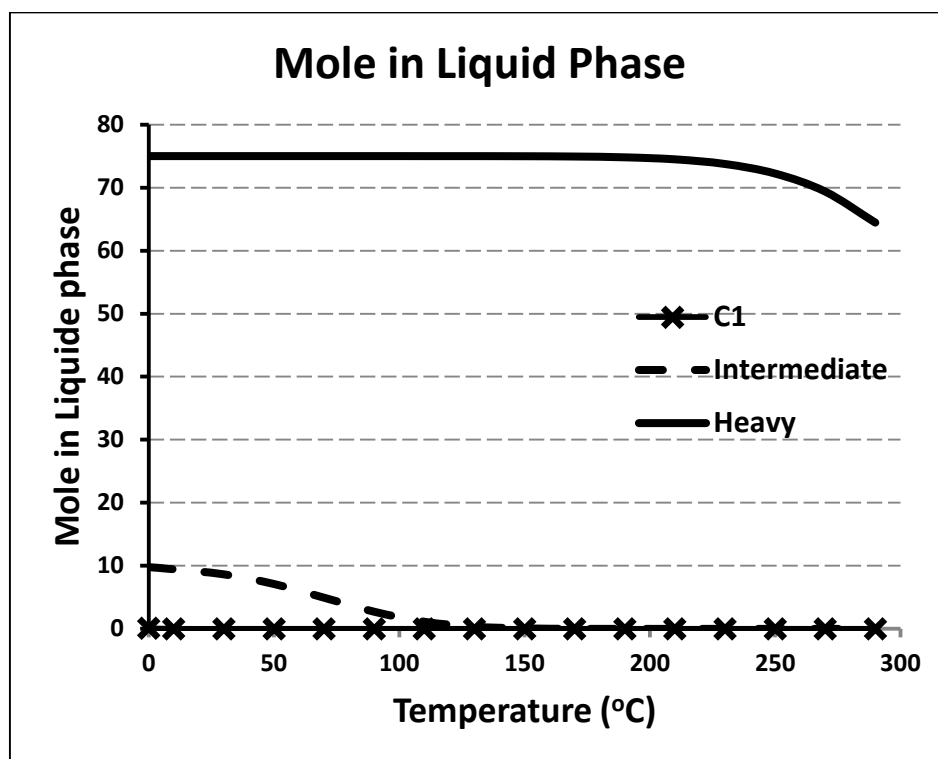


Figure 3.6, Gradual variations in the molar fraction of the components in the liquid phase of the heavy oil model at pressure of 1 atm, with 0.75 moles of heavy, 0.10 moles of intermediate and 0.15 moles of C1. Note that initially there is no light C1 component in the liquid phase, and by increasing temperature at constant pressure liquid loses more components.

Figure 3.7 illustrates the estimated viscosities at 1 atm and different temperatures, using Pedersen's correlation. Two mechanisms contribute to controlling the fluid viscosity. The first is the melting process, which is inclined to decrease the viscosity; and the second is gas liberation, which made the remaining liquid phase more viscous. Both of these mechanisms were taken into account in generating Figure 3.7, which demonstrates that the melting mechanism had the dominant influence on the viscosity.

Figure 3.8 shows the storage moduli (the real part of the complex shear modulus) of the two fluids as a function of frequency at 10°C and 50°C. The increased temperature shifted

the curve to the right, i.e., by increasing the temperature, the same storage value occurred at higher frequency (i.e. at an earlier time). The wide ranges of frequencies were chosen to delineate the differences and similarities between the four presented cases.

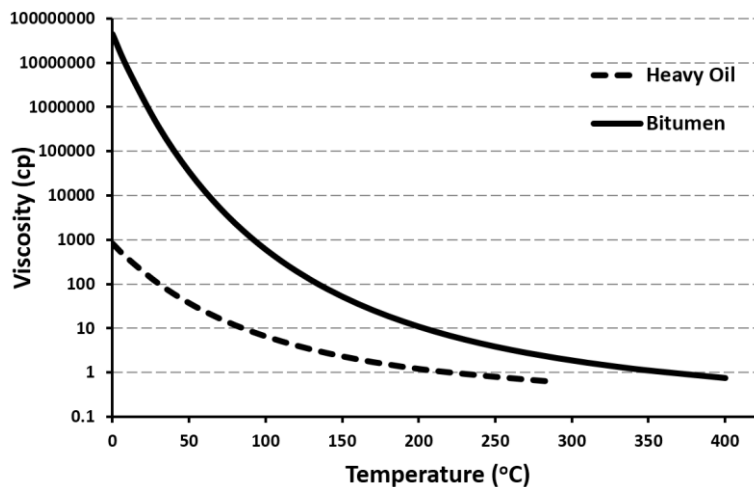


Figure 3.7, Viscosity variations of the oil samples as a function of temperature at 1 atm.

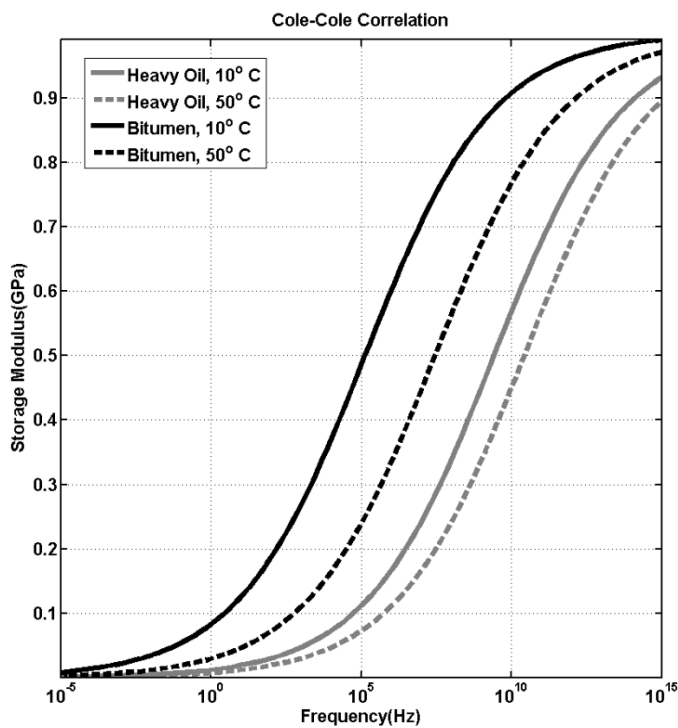


Figure 3.8, Cole-Cole fit for the heavy oil and bitumen models at 10 and 50°C.

Other attenuation mechanisms could also have occurred over this wide range of frequencies, making the Cole-Cole prediction less reliable. At a certain frequency and temperature, the bitumen stores more shear energy than heavy oil, due to the stronger elastic behavior of bitumen. The storage modulus decreases with increasing temperature, indicating the transition of viscoelastic medium towards a viscous fluid.

Figure 3.9, shows the calculated elastic moduli from the double-porosity CPA method. Table 3.1, provides the parameters that were used in this modelling. Although all four cases show similar behavior with a shift along the frequency axis, their moduli are not the same in a certain range of frequencies. As evident in this figure, the bitumen saturated rock has higher moduli than the heavy oil saturated sample at any temperature and at a constant frequency. However, heating noticeably reduced the moduli of both fluid samples.

The behavior of attenuation in the saturated rock is complicated by the fluid's viscosity in the practical range of frequencies ($\sim 10^{-2}$ - 10^5 Hz). In the case of heavy oil samples (grey lines), attenuation decreases with increasing temperature (inverse proportionality). In this case, heating moves the heavy oil from a viscoelastic state to a less viscous fluid at all the frequencies in the aforementioned range, and the oil-rock system acts more like an elastic medium, resulting in lower attenuation. In contrast, bitumen attenuation strongly depends on frequency, since the oil-rock system still acts like a viscoelastic medium after heating. In such a case, in the low and high frequency ranges, we observe inverse and direct proportionalities between the temperature and the attenuation. At low frequencies, the mechanism is similar to that of the heavy oil. However, at high frequencies, the viscoelastic medium shows solid-like behavior: the higher the viscosity, the more solid like are the properties. Consequently, less attenuation is expected for the rock that is saturated with the

higher viscosity fluid; that is to say more solid like behavior is anticipated for bitumen at 10°C.

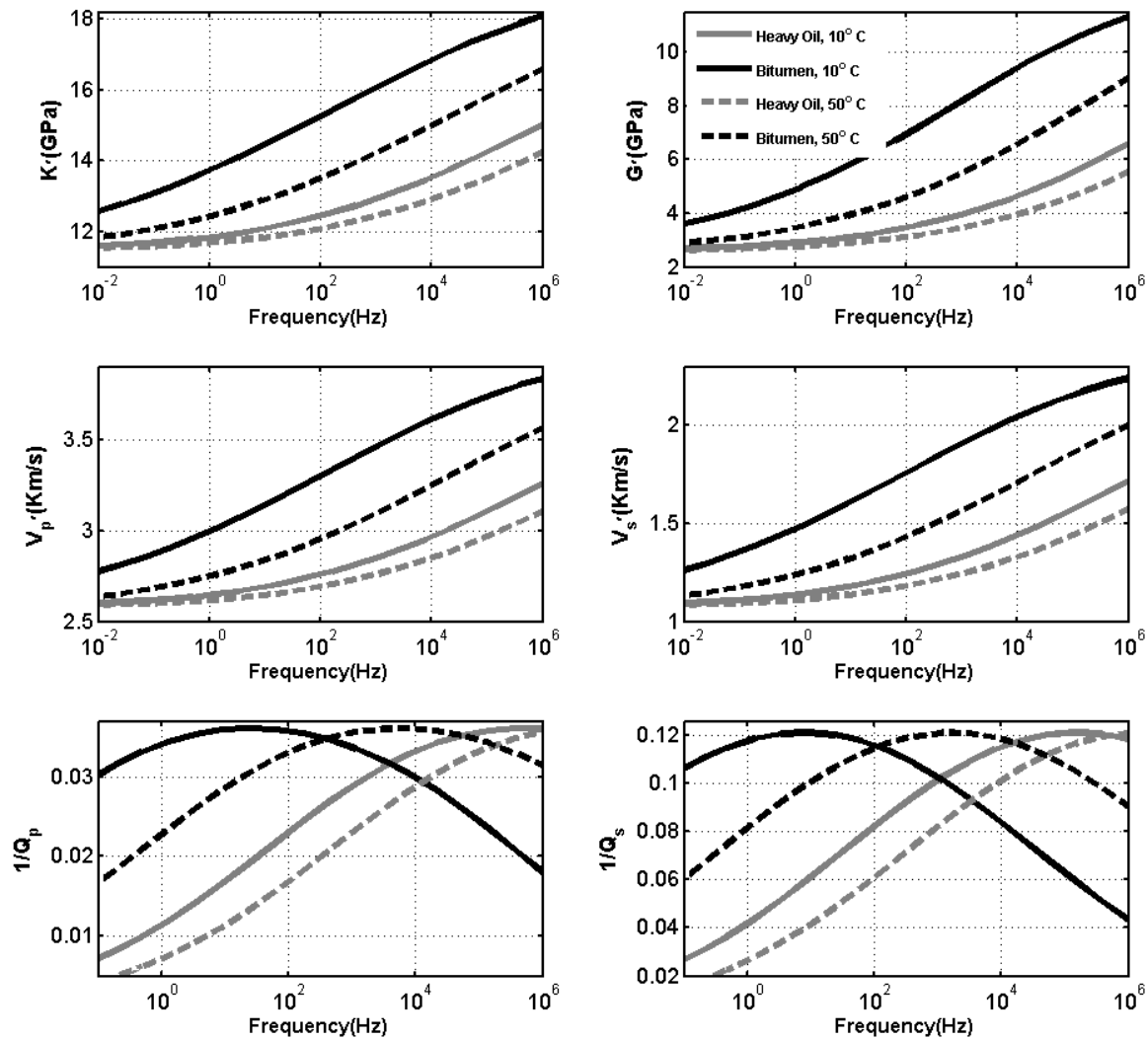


Figure 3.9, Double-porosity CPA modelling of elastic moduli of rock saturated with two oil samples at 10 and 50°C.

Figure 3.10 shows the shear wave attenuation as a function of frequency at varying temperatures for the bitumen model. The bell-shaped attenuation curve shifts to the right as the temperature increased; that is to say by increasing the temperature, the same amount of attenuation could be observed at higher frequencies. This follows the frequency-

temperature superposition; i.e. changes measured in the sample at low temperatures are similar to those at high frequencies and vice versa (Menard, 1999). In other words, at either a low temperature or a high frequency, the viscoelastic medium has the solid like behaviour.

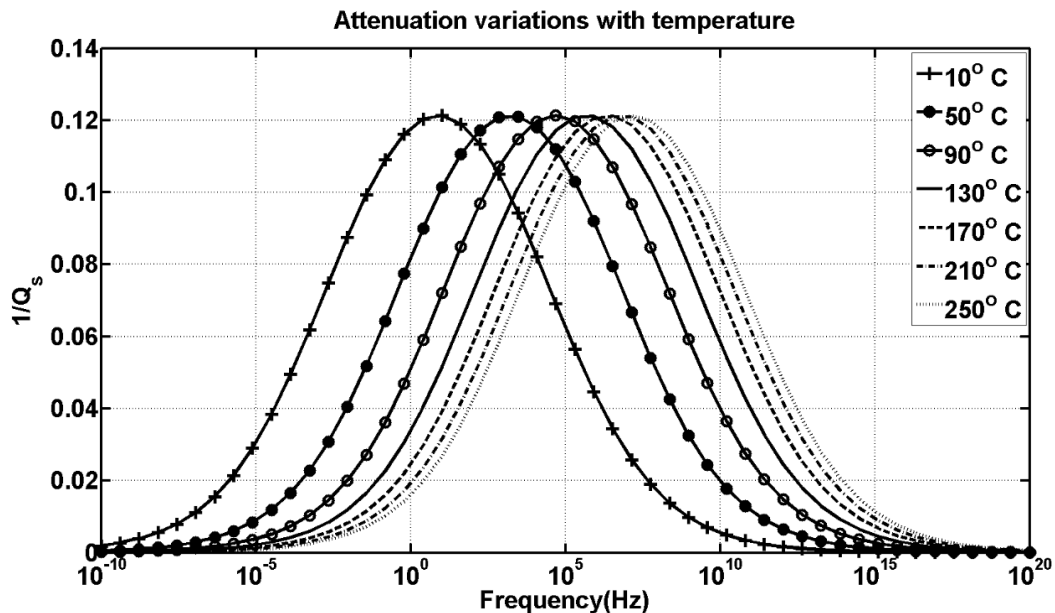


Figure 3.10, Attenuation curves for rock saturated with bitumen varying with temperature. At low frequencies (~ 1 Hz), there is an inverse proportionality between attenuation and temperature, where increasing temperature, decreases the attenuation. At very high frequencies ($\sim 10^{10}$ Hz), increasing temperature increases attenuation (direct proportionality). At medium frequencies ($\sim 10^4$ Hz), I observe that the maximum attenuation occurs at the intermediate temperature (130°C).

The bell-shaped curve of the attenuation plotted against frequency indicates that the attenuation increase to its maximum, which is followed by decreasing values. At both very high and low frequencies, there is elastic medium behavior. Considering that viscoelastic material acts like solid and liquid at high and low frequencies, respectively, the rock would

have contained both solid and liquid phases at high and low frequencies, respectively; this creates an elastic frame in both cases with very low attenuation.

To study the effect of temperature on attenuation, I focus on three curves in Figure 3.10: those at 10, 130 and 250°C. At low frequencies (~ 1 Hz), there is an inverse proportionality, where increasing temperature, decreases the attenuation. At very high frequencies ($\sim 10^{10}$ Hz), increasing temperature increases attenuation (direct proportionality). At medium frequencies ($\sim 10^4$ Hz), I observe that the maximum attenuation occurs at the intermediate temperature (130°C); the minimum attenuation is shifted from the highest temperature attenuation curve (250°C) to the lowest temperature attenuation curve (10°C) with increasing frequency.

One can conclude, therefore, that an increase followed by decrease in the attenuation trend may occur with increasing temperature (oil-rock Q_s , in Figure 3.11). However, to notice this behavior in the practical range of frequency ($\sim 10^{-2}$ - 10^5 Hz), heavy oil should have a very large viscosity, or else it falls in the zone in which inverse proportionality exists between attenuation and temperature. This situation is evident in Figure 3.12 (oil-rock Q_s).

This characteristic increasing-decreasing behavior is in good agreement with the experiments done by Behura et al. (2007) for the Q of an oil-rock sample with Uvalde field data. It should, however, be noted that our modelling systematically contradicts the similar behavior for shear storage moduli of oil (G') recorded in the same article. In our simulation, G' decreases monotonically with increasing temperature (oil G' , in Figures 3.11 and 3.12); and, the results rule out the possibility of observing the decreasing-increasing trend for G' of oil, due to the loss of light components. Nonetheless, this monotonically decreasing trend is in line with the expectation of observing a zero shear modulus at high temperatures,

where the medium is literally a viscous fluid. The aforementioned discrepancy between the recorded and expected behavior of Newtonian fluids, were also mentioned in the same article by Behura et al. (2007).

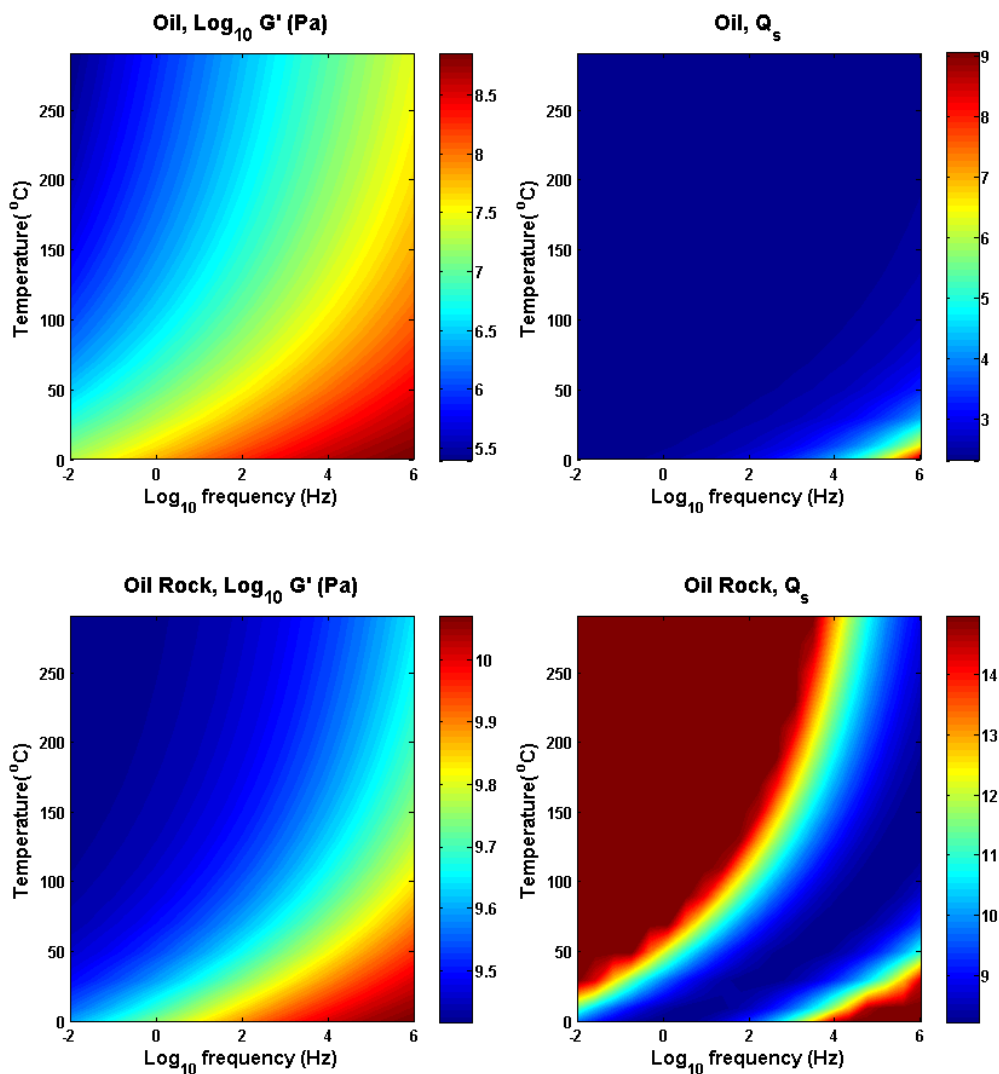


Figure 3.11, Oil (first row) and rock oil (second row) storage modulus (first column) and Q (second column) of the bitumen sample.

During a solvent-based heavy oil recovery process that is based on the dilution of heavy oil using solvents, such as C3 to C6, the precipitation of asphaltene is almost always the

case; and the non-monotonic trend for G' of oil would definitely be observed with increasing temperature. In fact, one of the advantages of injecting solvent, is the in situ upgrading of oil by leaving the precipitated asphaltene behind in the reservoir. The applied solvent (toluene) for extracting heavy oil in Behura et al. (2007), probably has altered the oil stability condition and reduced the solubility of the asphaltene in a similar mechanism with increasing temperature, eventually resulting in a solid phase and an increasing G' .

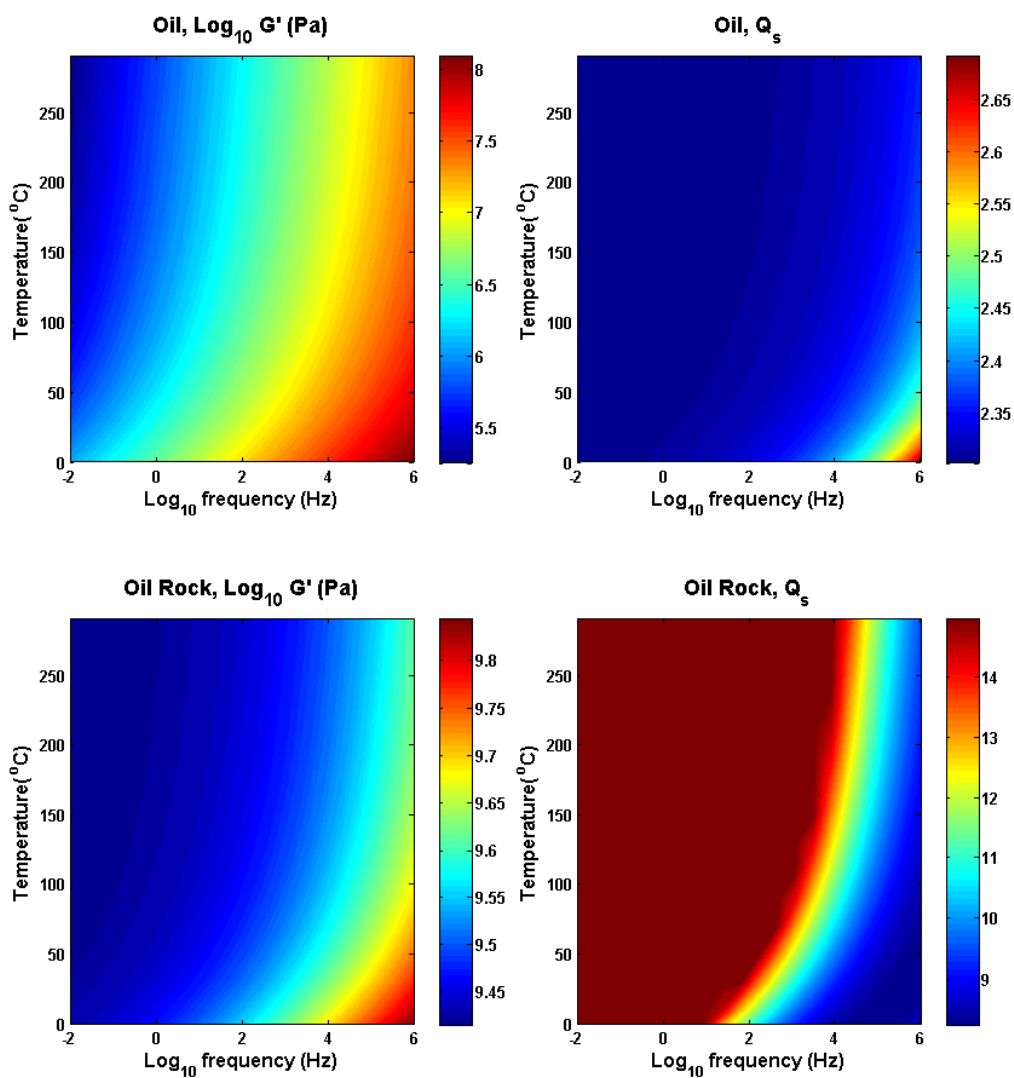


Figure 3.12, Oil (first row) and rock oil (second row) shear storage modulus (first column) and Q (second column) of the heavy oil sample.

As evident in Figures 3.11 and 3.12, each of the modelled fluids has their own individual pattern of elastic moduli as functions of frequency and temperature. This unique signature is based on the rock properties and the composition of the saturating fluid. Such a relation can be employed to find out the temperature distribution through the reservoir using the following workflow:

1. Divide the prestack seismic cube into the sub-cubes with certain frequency ranges, where the higher the divisions, the higher the temperature resolution, e.g., [0-15] Hz; [15-30] Hz; [30-45] Hz; [45-60] Hz; [60-75] Hz; [75-90] Hz; [90-105] Hz, and [105-120] Hz
2. Derive the shear moduli for all the sub-cubes using elastic inversion.
3. Create a signature map of the shear moduli of the oil-rock system, based on inversion results in step 2, using regions where we have good knowledge of the temperature distribution (e.g., around the hot steam injector wells or next to the cold reservoir boundaries). This signature map for the reservoir would be similar to Figures 3.11 and 12 (oil-rock, G'). One can also derive this map by laboratory measurements, if available.
4. Predict the temperature (and, as a result, viscosity) in the regions far from the wells, once we populate the signature map. We can estimate the unknown temperature based on the elastic moduli at the known frequency from step 2 and relation among the temperature, the frequency and the elastic moduli, characterized in step 3.

I have made the assumption that the oil composition and rock were similar for the entire reservoir; however, the rock obviously varies along the reservoir. Care must be taken in this regard, and the values for the shear modulus should be read from the similar facies in

the reservoir grid model. In other words, the number of signature maps should be equal to the number of facies in the reservoir model.

3.5 Summary

Viscoelastic fluid substitution modelling has been studied using compositional fluid models. This has led to the development of a practical fluid substitution framework that can be integrated with heavy oil phase behavior and simulation results. In cases with limited laboratory elastic measurements, the numerous uncertain parameters should be tuned with the available data before applying this modelling scheme to an entire reservoir. It would be interesting to evaluate the feasibility of the suggested fluid substitution scheme in a real reservoir simulation.

The fluid compositional analysis suggests that viscosity is such a strong function of temperature and that the solution's gas cannot have a tangible influence on the elastic moduli of heavy oil reservoirs. Considering the small amounts of gas in a solution and the low-pressure characteristics of heavy oil reservoirs, we can conclude that the viscosity increase due to gas liberation can simply be ignored in heavy oils. Hence, the fluid shear modulus should decrease monotonically with increasing temperature.

Attenuation always has a bell-shaped behavior with increasing frequency at a constant temperature. At a constant frequency, however, different behaviors may be observed for attenuation with increasing temperature, depending on the measured frequency and oil viscosity. In an applicable range of frequencies ($\sim 10^{-2}$ - 10^5 Hz), attenuation decreases after an increasing trend for ultra-heavy oil, whereas a monotonically decreasing trend is expected for heavy oils with lower viscosities.

Based upon the temperature-frequency-shear modulus relationship, a new approach has been proposed for estimating temperature in the reservoir. Further research in this regard, with application in real cases, is recommended to validate the proposed method.

Chapter Four: **Stress substitution models**

Stress variations during the course of production of a reservoir can have significant time-lapse effects on seismic responses as a result of consequential variations in seismic velocities. These stress-induced velocity changes can be even higher than the changes in velocity due to the fluid substitution, depending on the rock's property.

There are two fundamental differences between the flow induced and geomechanical induced time lapse signatures. Firstly, the tensorial nature of production/injection induced stress will translate to velocity anisotropy as a function of time. The second difference is that the reservoir production/injection not only changes the velocity of seismic waves within and beneath the reservoir, but also impacts overburden and sideburden velocities (Herwanger and Koutsabeloulis, 2011).

During the course of reservoir production, any disturbance in the reservoir equilibrium by either production or injection will result in significant consequences on the stress state of the reservoir and neighboring host rocks. The decrease in the pore pressure due to production causes the rocks to undergo an additional overburden load. This is because a portion of supporting pore fluid has been expelled and the remaining fluid has partially lost its opposing pressure. This will transfer the resultant excess load of the overburden to the rock framework. This compressional stress is the origin of velocity variations. A similar argument is also true for the case of injection, which will result in tensional stress.

Obviously, the alteration in the stress state is higher around the wellbore and gradually diffuses away farther from wells, the fact that will trigger a series of momentums. For example, it induces a non-uniform stress variation that can potentially activate faults, or disturb cap rock integrity. The change in effective stress also tends to decrease (or increase)

the porosity and permeability. This is because the stress variations can open (injection) or close (production) fractures and pores. Subsidence is another side effect of the induced stress, which also can dramatically impact the well bore stability (Sayers, 2010).

Stress variations not only modify the wave velocity within the reservoir, but also impacts the surrounding rocks including overburden, underburden and sideburdens. This means that the time lapse seismic signatures can potentially be seen on the host rocks too. This fact is quite compelling since overburden is not affected by the fluid variations, and by modelling overburden stress changes, we can differentiate between the stress and fluid effects in the reservoir. With all these significant changes due to deviation from the base stress state of the reservoir, it is reasonable to expect that such changes can be captured in 4D time lapse seismic monitoring either as time shifts or as amplitude changes (Segall, 1989; Grasso, 1992; Hatchell et al., 2003, Hatchel and Bourne, 2005; Staples et al., 2007a; Herwanger and Horne, 2009; Sayers, 2010; Herwanger and Koutsabeloulis, 2011).

In conventional reservoir simulations the interaction between stress variations and fluid flow is generally ignored, where they do interact and can be modelled by coupling geomechanical and flow simulators. This ignorance is partially due to the complexity of the geological model, unknown rock mechanical parameters, and intensive numerical computations of the coupled system of equation.

During the conventional flow simulation, permeability is treated as invariable and porosity variation is estimated as a function of pressure using pore compressibility. On the other hand in the coupled geomechanical-flow system, the altered stress state will impact porosity and permeability as the result of production/injection. Employing a geomechanical simulator to model such variations results in updated permeability and

porosity at every simulation time step which will be fed into the flow simulator. The flow simulator in turn, provides the pressure and temperature values at every time steps to the geomechanical simulator.

In practice the coupling between fluid flow and rock mechanics can be established using a wide range of techniques, from empirical correlations to implicit methods which tend to solve coupled differential equations. However, there are two schemes for solving the coupled geomechanical-flow simulation, in general. In *One-way coupling*, fluid simulation results (pressure and temperature) are fed into the geomechanical simulator in different time steps. However, fluid simulation remains independent of the geomechanical parameters (porosity and permeability do not change). This deficiency is the price for obtaining fast geomechanical results. In *Two-way coupling*, both simulators are communicating back and forth during at every time steps. In such a case, results of flow or geomechanical simulation will impact the other simulator. As Tran et al. (2009) pointed out, in this case the flow variables (pressure, temperature) and geomechanical variables (stress, displacements) can be solved simultaneously using a single matrix, or can be solved separately and in sequence. Samier et al. (2003) compared and summarized different coupling schemes. Hernandez (2011) provided a detailed research on the application of different coupling methods, with their implications in various production scenarios.

In this chapter geomechanical effects on seismic velocities are investigated. Since the effects of pore fluid changes on seismic velocity variations have already been discussed in chapter three and chapter four, the focus here is only on the matrix and the framework. Several different scenarios has also been modelled using coupled geomechanical-flow

simulator to demonstrate the stress changes due to reservoir behaviour and the resultant impacts on the seismic velocity.

4.1 Theoretical background

Three orthogonal principal stresses i.e., S_v , S_H , S_h as well as the direction of one of the horizontal stresses are essential to describe the stress state in the earth. S_v is normal to the earth and two horizontal stresses are usually perpendicular to S_v and to each other in a horizontal plane. In general, to describe the state of stress, one must define six stress magnitudes or three stress magnitude and the three angles that defines the orientation of the stress coordinate system with respect to a reference coordinate system (Zoback, 2012). An important concept in geomechanical studies is the *Effective stress*, which is defined as,

$$\sigma_{ij} = S_{ij} - \delta_{ij}\beta P_p \quad (4.1)$$

where S_{ij} is the principal stress (e. g., S_v , S_H , S_h), P_p is pore pressure (or fluid pressure), δ_{ij} is Kronecker delta function, and β is an effective stress coefficient, known as Biot's constant, which is defined as $1 - K_{dry}/K_m$, so $0 \leq \beta \leq 1$. The importance of the effective stress concept is that, it is the parameter that control the seismic properties of the rock. Seismic velocities and both compressional (I_p) and shear (I_s) impedances, have direct relationships with effective stress (Wang, 2001). According to equation (4.1), pore pressure opposes the confining overburden pressure. Hence, the effective pressure is an inevitable parameter defined to characterize the opposite impacts of the pore pressure and confining pressure on the elastic parameters. Apparent in equation (4.1) is that pore pressure can't exceed S_{ij} , otherwise the formation will be hydraulically fractured.

In addition to the vertical stress, an earth medium undergoes horizontal stresses as well. This horizontal stress is the result of vertical stress on the rock and inability of the bounded

rocks to expand. The relationship between horizontal and vertical stress can be shown to be as the following:

$$S_H = S_h = \frac{\nu}{1 - \nu} S_v \quad (4.2)$$

where S_v , S_H , and S_h are the principal vertical, maximum and minimum horizontal stress, respectively and ν is the Poisson's ratio. According to equation (4.2), the higher the Poisson's ratio (more deformable rock) results in higher horizontal stress. This is because a hard rock can partially support the vertical stress, however, rocks like shale with higher Poisson's ratio will deform more compared to sands, and since they are bounded by the surrounding rocks and hence unable to expand, most of the vertical stress will be transferred to surrounding rocks, which in turn increases the horizontal stress. This explains the fact in hydraulic fracturing, in which a certain amount of pressure that can exceed the S_h and break a sand formation, cannot break the shale formation and the fracture stops growing (supposing that shale has higher Poisson's ratio).

In case of porous medium with pore pressure P_p , similar equation to equation (4.1) holds for effective stress:

$$\sigma_H = \sigma_h = \frac{\nu}{1 - \nu} \sigma_v \quad (4.3)$$

Substituting the effective stress expression in equation (4.1) into equation (4.3), will result in:

$$S_H = S_h = \frac{\nu}{1 - \nu} S_v + \frac{1 - 2\nu}{1 - \nu} \beta P_p \quad (4.4)$$

where S_v , S_H , and S_h are the principal vertical, maximum and minimum horizontal stress, respectively, β is the Biot's constant, P_p is the pore pressure and ν is the Poisson's ratio.

The second term in right hand side of the equation (4.4) corresponds to the contribution of

pore pressure to the horizontal stress. According to this equation, the lower the pore pressures the lower the horizontal stress, which means easier failure of formations in low pressure zones. This explains why drillers tend to decrease the mud weight while drilling within a depleted zone.

Note that depletion will reduce S_h , where has negligible effect on S_v . This means that in case of reservoir depletion, the rate of increase of $\sigma_v = S_v - \beta P_p$ is faster than $\sigma_h = S_h - \beta P_p$ which will result in increase of the shear stress. This in turn can reactivate the faults, compromise the cap rock integrity, result in shear failure, and cause wellbore instabilities. For more detailed derivations and discussions regarding to the background theory, the interested reader can refer to Sayers (2010) and Zoback (2012).

4.1.1 Production/Injection impacts on effective pressure

The effective stress principal states that all measurable effects of a change in stress – such as compaction and variation in elastic wave velocities – are only functions of the effective stress (Sayers, 2010). Since effective stress is a function of pressure depletion or pressure build up, then a reservoir can potentially undergo a complex stress state variations during its life. Here in this section, I will investigate how reservoir production/injection will influence the stress state of the reservoir and the rock displacement.

In the following analysis, the effective stress and rock displacements have been modelled using a coupled geomechanical-flow simulator around injection and production wells. The applied simulator implements one-way coupling. In this scheme the stress variation occurs due to pressure and temperature changes in the flow simulator, where the induced stress will not impact the flow simulator (permeability and porosity are not affected). This is sufficient for the purpose of this study since the porosity and permeability

variations and their impacts on fluid simulation is not the concern in this research. The deployed flow simulator, ECLIPSE, feeds its results into PETREL RG (reservoir geomechanics) plug-in for PETREL. This plug-in employs the geomechanical simulator engine called Visage at each time step to simulate induced stress and resultant displacements using finite element method. Both software are Schlumberger commercial packages.

Hereafter, the following conventions are selected for the analysis:

- Compressional stress (push) is negative and tensile stress (pull) is positive,
- Negative change in principal stress (red color) → increase in compression force (pushing force),
- Positive change in principal stress (blue color) → increase in extensional force (pulling force).

It is apparent that at the well location, which is either source or sink of pressure, the largest pressure disturbance is observed and as a result we expect maximum alteration of effective stress. Figure 4.1, illustrates reservoir effective stress distributions around two production wells after 5 years. Note that the compressional effective stress has increased as a result of pore pressure decrease. This behaviour is typical in the producer wells in which reduction in pore pressure tends to increase the effective stress according to the equation (4.1). This is because the reservoir has been depleted and the fluid which used to partially support the overburden load has left the pore space.

Compressional stress increase in vertical direction, also will happen in sideburdens, where underburden and overburden will unbound and subside respectively. The overburden velocity variation is unique in a sense that it is rooted only from stretching (or squeezing)

of the rocks due to the compaction (or expansion) of the reservoir. Unlike the reservoir in which velocity variations are also controlled by fluid replacement, overburden is only influenced by geomechanical momentums.

Figure 4.2, shows another scenario in which one of the wells is an injector. As the injector well increases the pore pressure, effective stress will be reduced. This in turn, will put underburden and overburden into further compressional stress.

Figure 4.3 and figure 4.4, shows the horizontal effective stress changes, for these two scenarios. It can be seen that similar behaviour to vertical direction is happening for the horizontal stress. One can see that by rotating the vertical stress variations by 90° , it will be converted to the horizontal stress (compare figure 4.2 and figure 4.4 for example).

Displacement is another unknown parameter in geomechanical simulation. Figure 4.5 and figure 4.6 delineate the rock displacement in vertical direction in production and production/injection scenarios, respectively. Figure 4.7 and figure 4.8 show the horizontal displacement in the two scenarios.

In figures that displacements are displayed, the downward and leftward movements are colored in red, where upward and rightward displacements are represented in blue color. During the production of a well, reservoir shrinks due to depletion and loses part of supportive force of fluids. As the result, the surrounding rocks around the reservoir are going to unbound due to increase in tensile stress and are going to move towards the reservoir. Strictly speaking the predominant stress state is still compressional, and only tensile stress is added to the background which leads to the overall decrease of compressional stress state. This phenomenon is reversed in injector wells, where reservoir expands and the surrounding rocks are going to move away from the reservoir, accordingly.

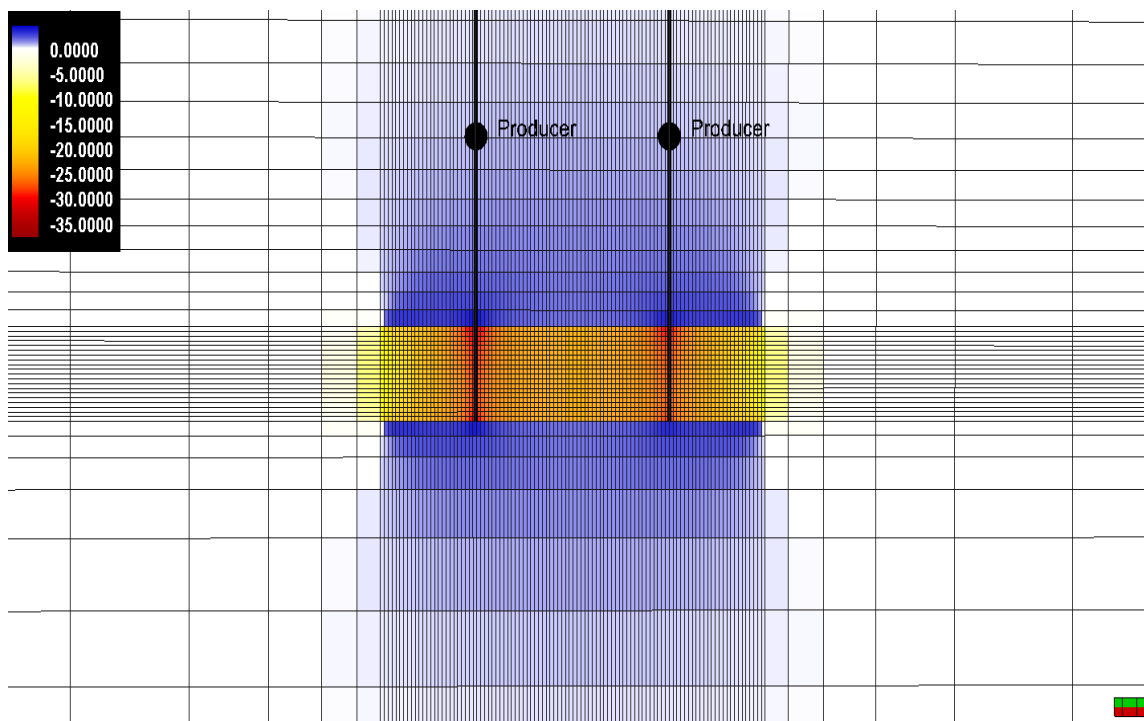


Figure 4.1, Vertical effective stress changes (bar) after five years of production in two wells

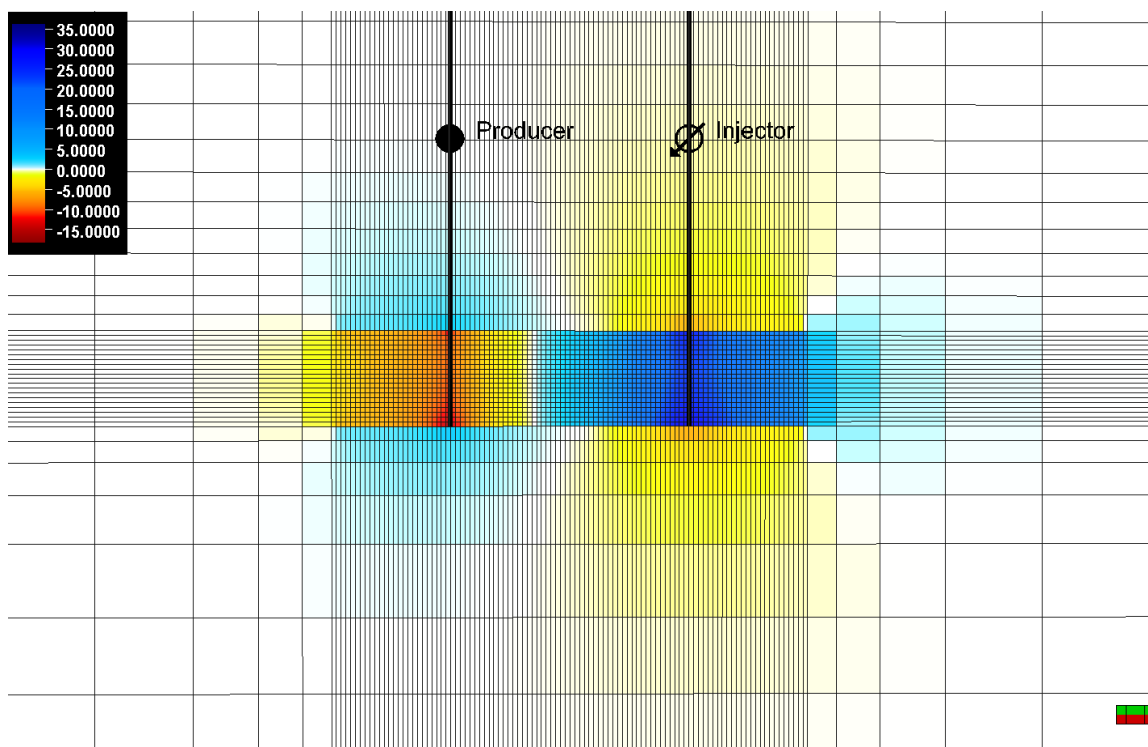


Figure 4.2, Vertical effective stress changes (bar) after five years of production and injection.

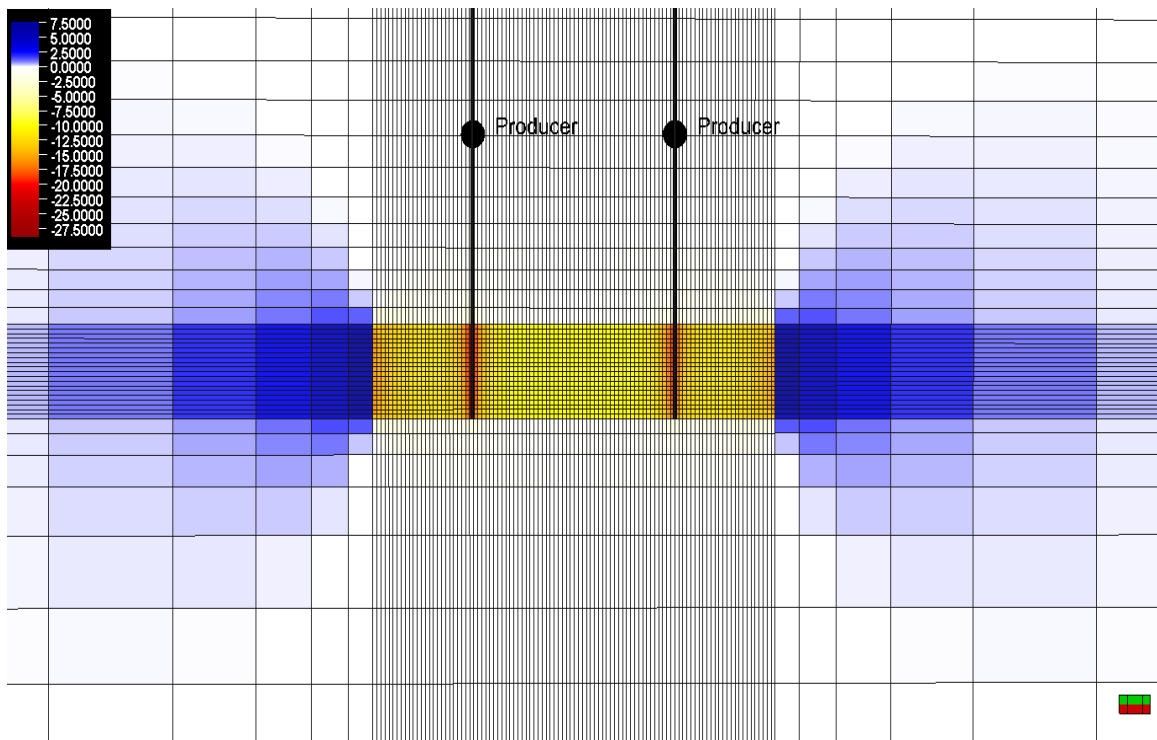


Figure 4.3, Horizontal effective stress changes (bar) after five years of production in wells.

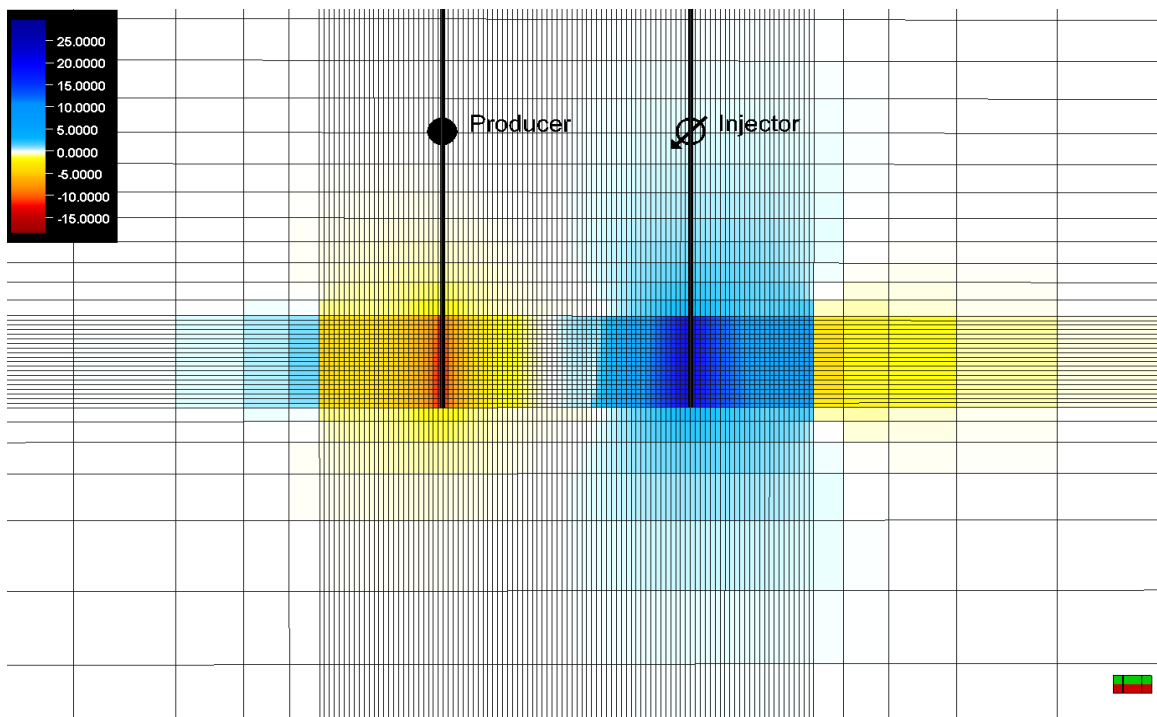


Figure 4.4, Horizontal effective stress changes (bar) after five years of production and injection.

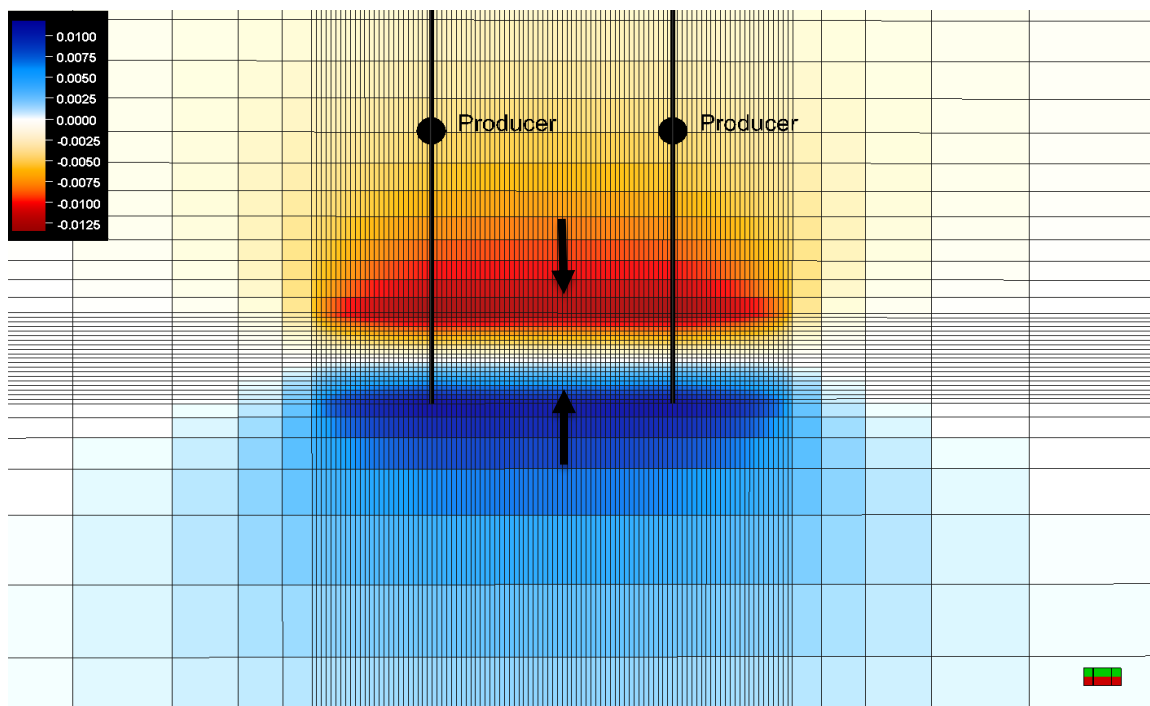


Figure 4.5, Vertical displacement (meter) after five years of production in wells.

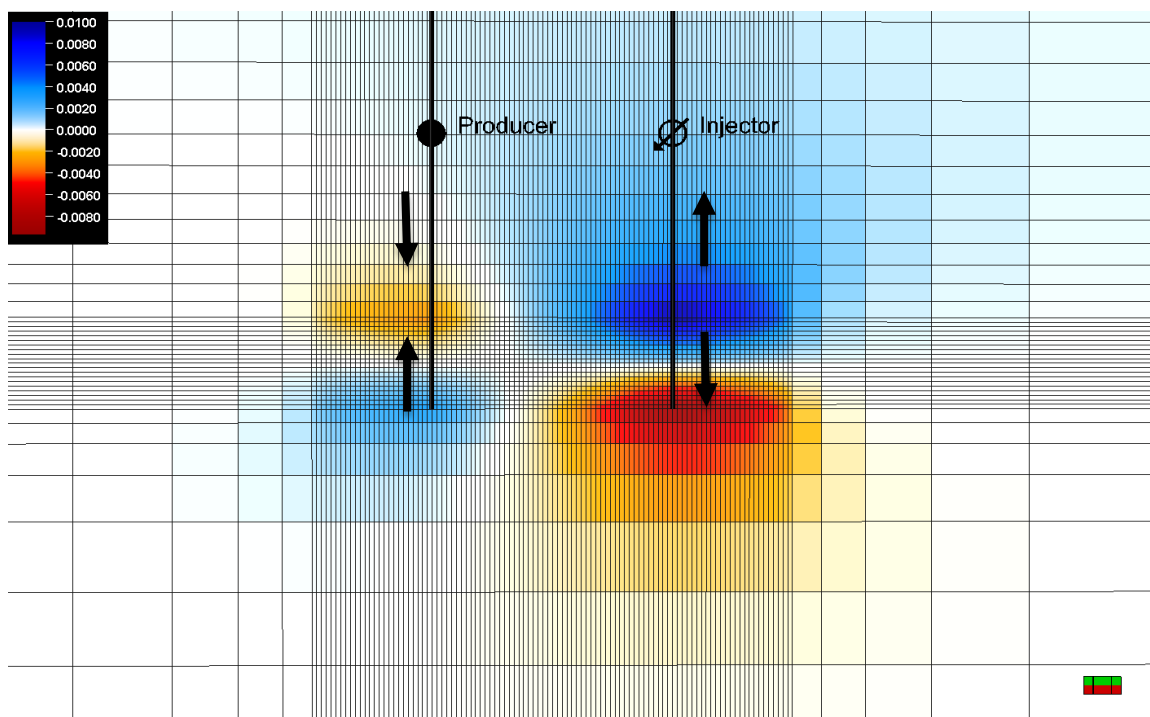


Figure 4.6, Vertical displacement (meter) after five years of production and injection.

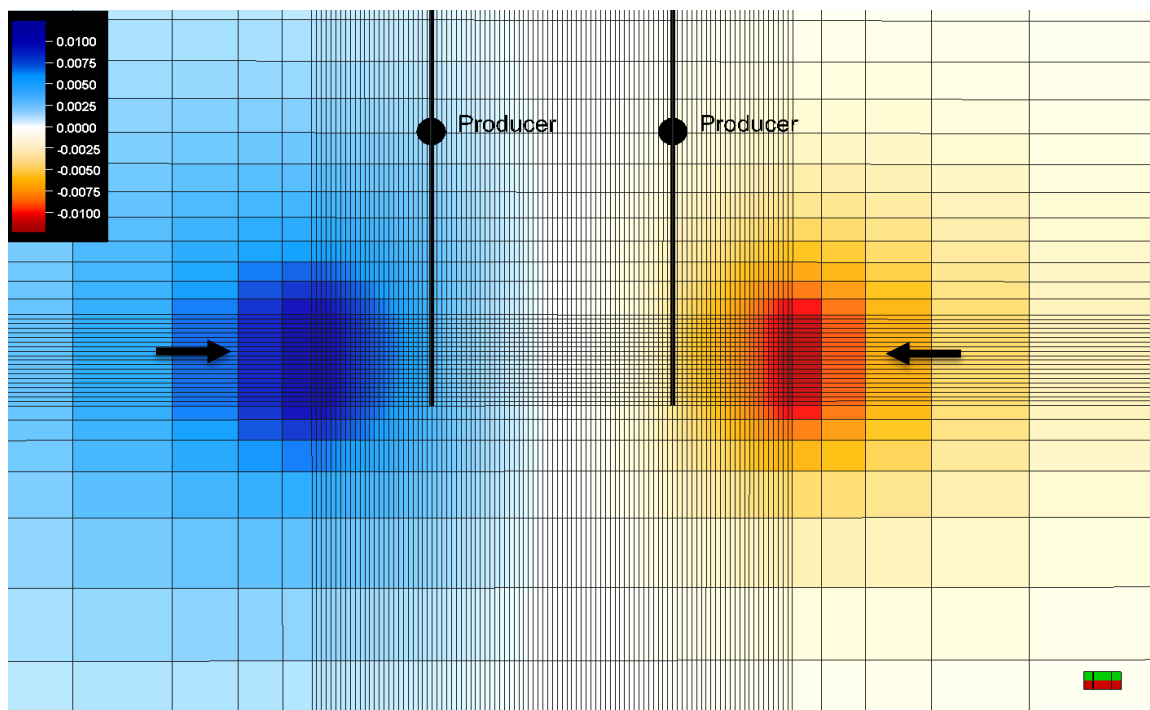


Figure 4.7, Horizontal displacement (meter) after five years of production and injection.

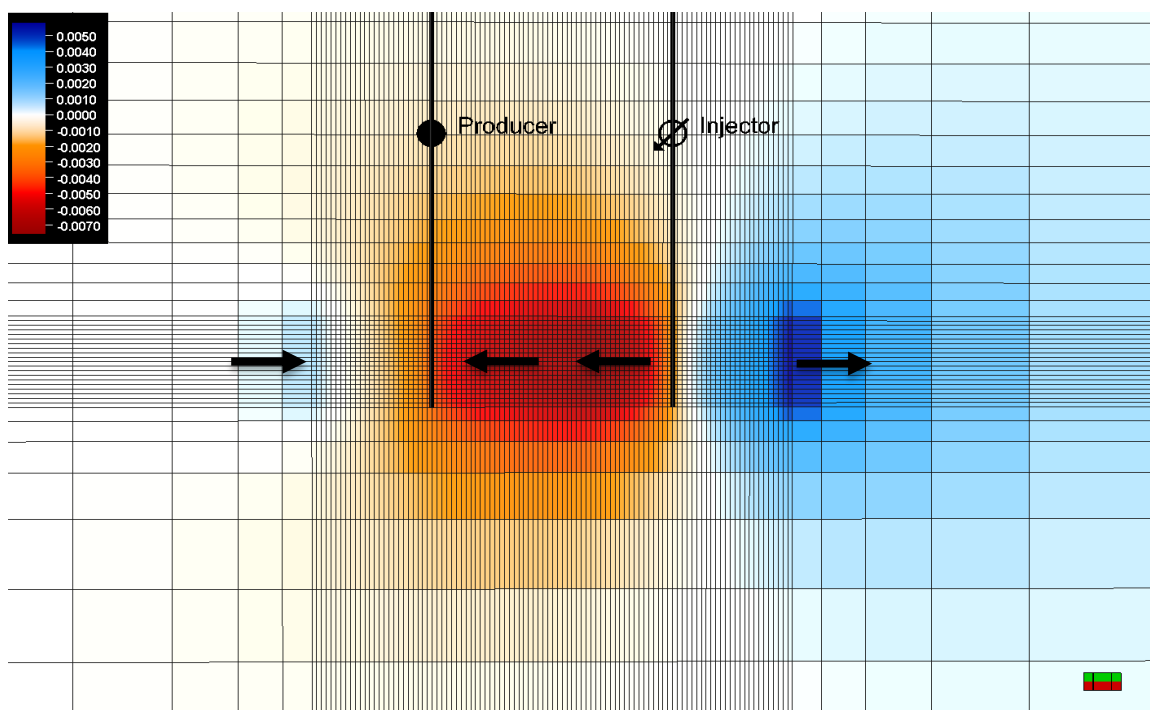


Figure 4.8, Horizontal displacement (meter) after five years of production and injection.

4.1.2 Velocity dependency to the stress state

Elastic wave velocities in rocks vary with changes in effective stress due to the presence of stress-sensitive discontinuities within the rock such as grain boundaries, pores and fractures. In fact, elastic wave velocities in sedimentary rocks are strong non-linear functions of stress (Sayers, 2005). At high confining stress, any discontinuities within the rock are assumed to be closed. At intermediate stress it is assumed that discontinuities are partially open. Applying stress on a rock tends to compress the grain contacts between opposing faces of the discontinuity, and causes an increase in the velocity of the propagating wave. This implicitly means that changing the stress state of an elastic medium will change the stiffness tensor; the fact that is usually ignored in most applications of elasticity. The assumption of elastic properties that are independent of stress state is called *second-order elasticity*. In contrast, the *third-order elasticity* is a theory which describes the dependency of elastic constants to the stress state (Herwanger and Koutsabeloulis, 2011).

In this section, workflow to calculate velocity as a function of stress variations (after Herwanger and Koutsabeloulis, 2011) are explained, assuming the third-order elasticity holds. The objective is to relate the velocity variations to the changes in stress state of a rock.

The earth is assumed to be isotropic medium, most of the time. Nonetheless, earth is comprised of minerals which are typically anisotropic. In addition layered earth and fractures can introduce anisotropic medium. Applying different stress loads on such a medium, will impact velocity propagation in different orientations differently, which is opposed to the case of isotropic earth assumption.

In a vertical transverse isotropic medium, the stiffness tensor has five independent elastic elements:

$$C_{VTI} = \begin{bmatrix} C_{11} & C_{12} & C_{13} & 0 & 0 & 0 \\ C_{12} & C_{11} & C_{13} & 0 & 0 & 0 \\ C_{13} & C_{13} & C_{33} & 0 & 0 & 0 \\ 0 & 0 & 0 & C_{44} & 0 & 0 \\ 0 & 0 & 0 & 0 & C_{44} & 0 \\ 0 & 0 & 0 & 0 & 0 & C_{66} \end{bmatrix} \quad (4.5)$$

where $C_{12} = C_{11} - 2C_{66}$.

Figure 4.9, shows these five elements of stiffness tensor as a function of effective stress for the Jurassic shale sample reported in Hornby (1998). The analytical curve fit to the measured data is based on the correlation suggested by MacBeth (2004):

$$C_{ij} = \frac{C_{ij}^{\infty}}{1 + E_{C_{ij}} e^{-\frac{P_{eff}}{P_{C_{ij}}}}} \quad (4.6)$$

where C_{ij}^{∞} , $E_{C_{ij}}$ and $P_{C_{ij}}$ can be estimated by finding the best fit curve through the measured data. MacBeth (2004), used this equation to describe pressure dependency of shear modulus and bulk modulus of different rock samples. Herwanger and Koutsabeloulis (2011) employed this equation to model all the elements of stiffness tensor.

Third order elasticity theory

For the next set of analysis the third order elasticity theory is used to predict stiffness tensor as a function of effective stress. Third-order elasticity theory as described in Prioul et al. (2004) can be employed to predict the stiffness tensor at a certain stress distribution in stressed VTI solid. This model needs the knowledge of strain variations in three principal

axis as well as three third-order elastic tensors plus the reference values of the stiffness tensors:

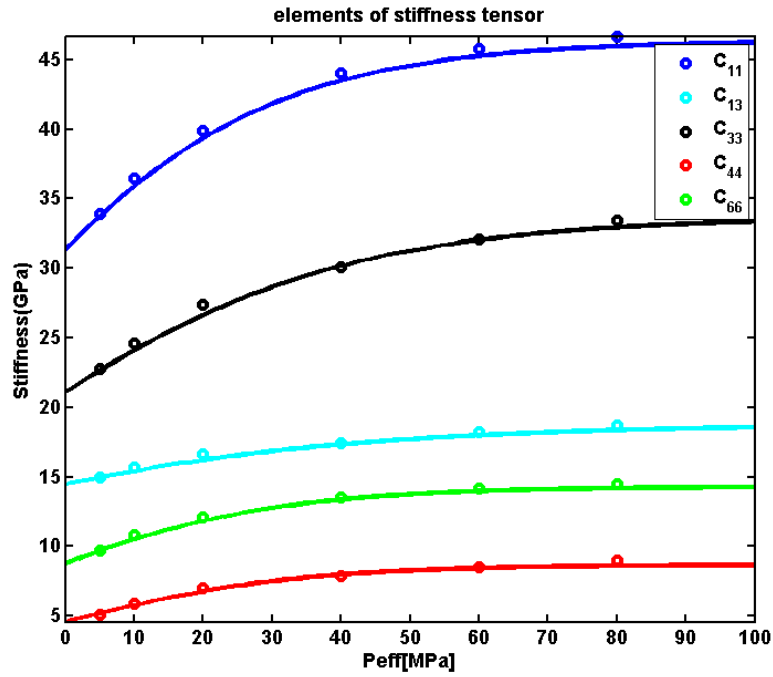


Figure 4.9, Elements of stiffness tensor as functions of effective stress, modelled using MacBeth (2004) correlation (after Herwanger and Koutsabeloulis, 2011).

$$C_{11} \cong C_{11}^0 + c_{111}\varepsilon_{11} + C_{112}(\varepsilon_{22} + \varepsilon_{33}) \quad (4.7)$$

$$C_{22} \cong C_{11}^0 + c_{111}\varepsilon_{22} + C_{112}(\varepsilon_{11} + \varepsilon_{33})$$

$$C_{33} \cong C_{33}^0 + c_{111}\varepsilon_{33} + C_{112}(\varepsilon_{11} + \varepsilon_{22})$$

$$C_{12} \cong C_{12}^0 + c_{112}(\varepsilon_{11} + \varepsilon_{22}) + C_{123}\varepsilon_{33}$$

$$C_{13} \cong C_{13}^0 + c_{112}(\varepsilon_{11} + \varepsilon_{33}) + C_{123}\varepsilon_{22}$$

$$C_{23} \cong C_{13}^0 + c_{112}(\varepsilon_{22} + \varepsilon_{33}) + C_{123}\varepsilon_{11}$$

$$C_{66} \cong C_{66}^0 + c_{144}\varepsilon_{33} + C_{155}(\varepsilon_{11} + \varepsilon_{22})$$

$$C_{55} \cong C_{44}^0 + c_{144}\varepsilon_{22} + C_{155}(\varepsilon_{11} + \varepsilon_{33})$$

$$C_{44} \cong C_{44}^0 + c_{144}\varepsilon_{11} + C_{155}(\varepsilon_{22} + \varepsilon_{33})$$

where $c_{144} = (c_{112} - c_{123})/2$ and $c_{155} = (c_{111} - c_{112})/2$. In these expressions C_{111} , C_{112} and C_{123} are three independent parameters that can be estimated from lab measurements.

Third-order elasticity is often not general enough to describe the shapes of real stress–strain curves over large ranges of stress and strain. Third-order elasticity is most useful when describing stress–strain within a small range around a reference state of stress and strain (Mavko et al., 2009).

As Herwanger and Koutsabeloulis (2011), pointed out the most complicated situation in which we can apply equation (4.7), is orthorhombic anisotropy provided that the symmetry axis of the anisotropy tensor and the stress tensor is in line with the coordinate axis. In the general anisotropy case, the number of the third order tensor can be as much as 53 (Hearmon, 1953; Sarkar et al., 2003)

Hooke's law

Note that Equation (4.7) is in fact a function of strain, so one step is needed ahead to calculate strain from the applied stress changes. To calculate values of strain one needs to compute the strain values resulting from stress variations using the inverse of Hooke's law.

The following equation expresses Hooke's law:

$$\sigma_{11} = (\lambda + 2\mu)\varepsilon_{11} + \lambda\varepsilon_{22} + \lambda\varepsilon_{33} \quad (4.8)$$

$$\sigma_{22} = \lambda\varepsilon_{11} + (\lambda + 2\mu)\varepsilon_{22} + \lambda\varepsilon_{33}$$

$$\sigma_{33} = \lambda\varepsilon_{11} + \lambda\varepsilon_{22} + (\lambda + 2\mu)\varepsilon_{33}$$

$$\sigma_{12} = 2\mu\varepsilon_{12}$$

$$\sigma_{13} = 2\mu\varepsilon_{13}$$

$$\sigma_{23} = 2\mu\varepsilon_{23}$$

which its inverse is:

$$\varepsilon_{11} = \frac{1}{E}\sigma_{11} - \frac{\nu}{E}\sigma_{22} - \frac{\nu}{E}\sigma_{33} \quad (4.9)$$

$$\varepsilon_{22} = -\frac{\nu}{E}\sigma_{11} + \frac{1}{E}\sigma_{22} - \frac{\nu}{E}\sigma_{33}$$

$$\varepsilon_{33} = -\frac{\nu}{E}\sigma_{11} - \frac{\nu}{E}\sigma_{22} + \frac{1}{E}\sigma_{33}$$

$$\varepsilon_{12} = \frac{1}{2\mu}\sigma_{12}; \varepsilon_{13} = \frac{1}{2\mu}\sigma_{13}; \varepsilon_{23} = \frac{1}{2\mu}\sigma_{23}$$

4.1.3 Velocity calculation using the stiffness matrix

Herwanger and Koutsabeloulis (2011) summarized a two-step workflow for calculation of V_p and V_s in any arbitrary direction described by unit vector (n_1, n_2, n_3) using C_{ij} , stiffness tensor's elements and density, ρ .

In the first step, it is required to build the Kelvin-Christoffel matrix, Γ_{ij} as described by the following set of equations:

$$\begin{aligned}\Gamma_{11} = & n_1^2 C_{11} + n_2^2 C_{66} + n_3^2 C_{55} + 2n_1 n_2 C_{16} \\ & + 2n_1 n_3 C_{15} + 2n_2 n_3 C_{56}\end{aligned}\quad (4.10)$$

$$\begin{aligned}\Gamma_{12} = & n_1 n_2 (C_{12} + C_{66}) + n_1^2 C_{16} + n_2^2 C_{26} + n_3^2 C_{45} \\ & + n_1 n_3 (C_{14} + C_{56}) + n_2 n_3 (C_{46} + C_{25})\end{aligned}$$

$$\begin{aligned}\Gamma_{13} = & n_1 n_3 (C_{13} + C_{55}) + n_1^2 C_{15} + n_2^2 C_{46} + n_3^2 C_{35} \\ & + n_1 n_2 (C_{14} + C_{56}) + n_2 n_3 (C_{36} + C_{45})\end{aligned}$$

$$\Gamma_{21} = \Gamma_{12}$$

$$\begin{aligned}\Gamma_{22} = & n_1^2 C_{66} + n_2^2 C_{22} + n_3^2 C_{44} + 2n_1 n_2 C_{26} \\ & + 2n_1 n_3 C_{46} + 2n_2 n_3 C_{24}\end{aligned}$$

$$\begin{aligned}\Gamma_{23} = & n_2 n_3 (C_{23} + C_{44}) + n_1^2 C_{56} + n_2^2 C_{24} + n_3^2 C_{34} \\ & + n_1 n_3 (C_{46} + C_{25}) + n_2 n_3 (C_{36} + C_{45})\end{aligned}$$

$$\Gamma_{31} = \Gamma_{13}$$

$$\Gamma_{32} = \Gamma_{23}$$

$$\begin{aligned}\Gamma_{33} = & n_1^2 C_{55} + n_2^2 C_{44} + n_3^2 C_{33} + 2n_1 n_2 C_{45} \\ & + 2n_1 n_3 C_{35} + 2n_2 n_3 C_{34}\end{aligned}$$

In the second step the eigenvalues λ_i of the Γ matrix should be calculated, where the λ_1 , λ_2 and λ_3 correspond to V_p , fast V_s and slow V_s , respectively, assuming that $\lambda_1 > \lambda_2 > \lambda_3$. Eigenvectors represent the polarization directions. Velocities then can be calculated using:

$$V_i = \sqrt{\frac{\lambda_i}{\rho}} \quad (4.11)$$

Equation (4.10) and (4.11) has been employed to plot figure 4.10, using the stiffness tensor values which already were calculated in figure 4.9. Note that in figure 4.10, the rate of changes of velocity depends on the effective pressure. For example velocity change rate is larger for the same amount of effective pressure increase when initial effective pressure is 20 MPa, compared to 80 MPa.

Following Herwanger and Koutsabeloulis (2011), I am going to take a closer look at the velocity variations as a function of stress for two anisotropic rock models available in the literatures. The first example is a Jurassic shale sample as described by Hornby (1995, 1998). This rock is transversely anisotropic with a vertical symmetry axis (VTI) and density of sample is 2.54 g/cm³. According to Prioul et al. (2004) the third-order elastic constants are measured as $c_{111} = -3100$ GPa, $c_{112} = -800$ GPa and $c_{123} = 40$ GPa. The stiffness tensor of this rock, measured at 40 MPa has been reported as:

$$C_{sh-VTI} = \begin{bmatrix} 44.0 & 17.0 & 17.4 & 0 & 000 & 000 \\ 17.0 & 44.0 & 17.4 & 0 & 000 & 000 \\ 17.4 & 17.4 & 30.1 & 0 & 0 & 0 \\ 0 & 0 & 0 & 7.9 & 0 & 0 \\ 0 & 0 & 0 & 0 & 7.9 & 0 \\ 0 & 0 & 0 & 0 & 0 & 13.5 \end{bmatrix}$$

The second sample as described in Dillen et al. (1999) is the Colton sandstone which has an orthorhombic stiffness tensor with the density of 2.38 g/cm³ and third-order elastic constants of $c_{111} = -7400$ GPa, $c_{112} = -1400$ GPa and $c_{123} = 500$ GPa (Dillen, 2000):

$$C_{S-ORT} = \begin{bmatrix} 18.6 & 1.60 & 2.1 & 0 & 000 & 000 \\ 1.60 & 20.1 & 2.6 & 0 & 000 & 000 \\ 2.10 & 2.6 & 19.8 & 0 & 0 & 0 \\ 0 & 0 & 0 & 8.6 & 0 & 0 \\ 0 & 0 & 0 & 0 & 8.5 & 0 \\ 0 & 0 & 0 & 0 & 0 & 8.9 \end{bmatrix}$$

This sand stone can also exhibit VTI behaviour. The stiffness matrix as reported by Prioul et al. (2004) at -0.7 MPa is:

$$C_{S-VTI} = \begin{bmatrix} 20.1 & 2.08 & 2.13 & 0 & 00 & 00 \\ 2.08 & 20.1 & 2.13 & 0 & 0000 & 00 \\ 2.13 & 2.13 & 18.3 & 0 & 0 & 0 \\ 0 & 0 & 0 & 8.5 & 0 & 0 \\ 0 & 0 & 0 & 0 & 8.5 & 0 \\ 0 & 0 & 0 & 0 & 0 & 9.01 \end{bmatrix}$$

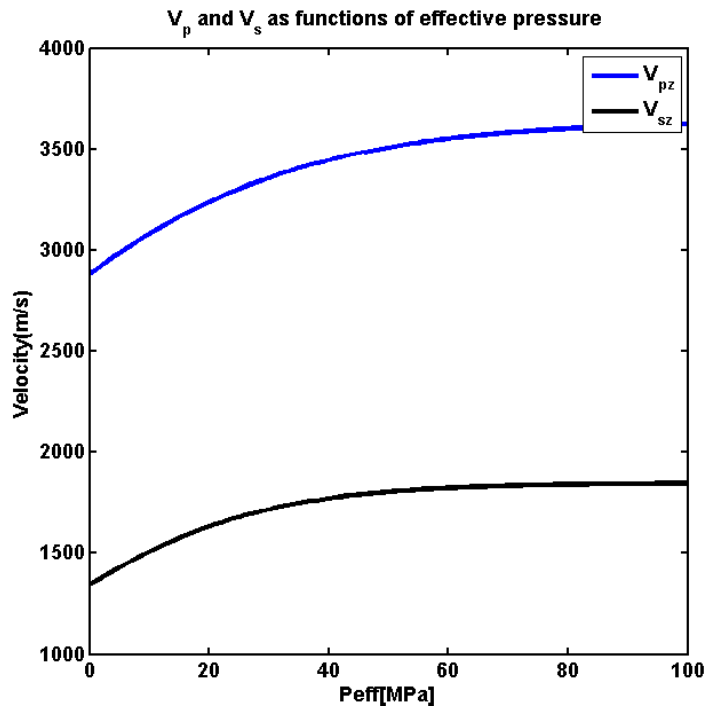


Figure 4.10, Velocity as a function of effective pressure, in the vertical direction stress (after Herwanger and Koutsabeloulis, 2011).

The colors in figure 4.11 shows the V_p in any arbitrary direction in the Jurassic shale. In this rock the velocity is a function of the propagation direction through the rock. It can be seen that it varies between 3600 m/s to 4100 m/s from vertical to horizontal direction. Figure 4.12, illustrates V_p and V_s variations as functions of vertical strain for major vertical and horizontal directions. This relationship has been investigated for three different stress system i.e., *Hydrostatic* stress test (Left), *Uniaxial* strain test (middle) and *Triaxial* stress test (right). Note that velocity behaviour highly depends on the stress system imposed on the medium. Figure 4.13 illustrate similar plots for orthorhombic sandstone sample. Note that V_p in the horizontal x and y directions are not equal any more.

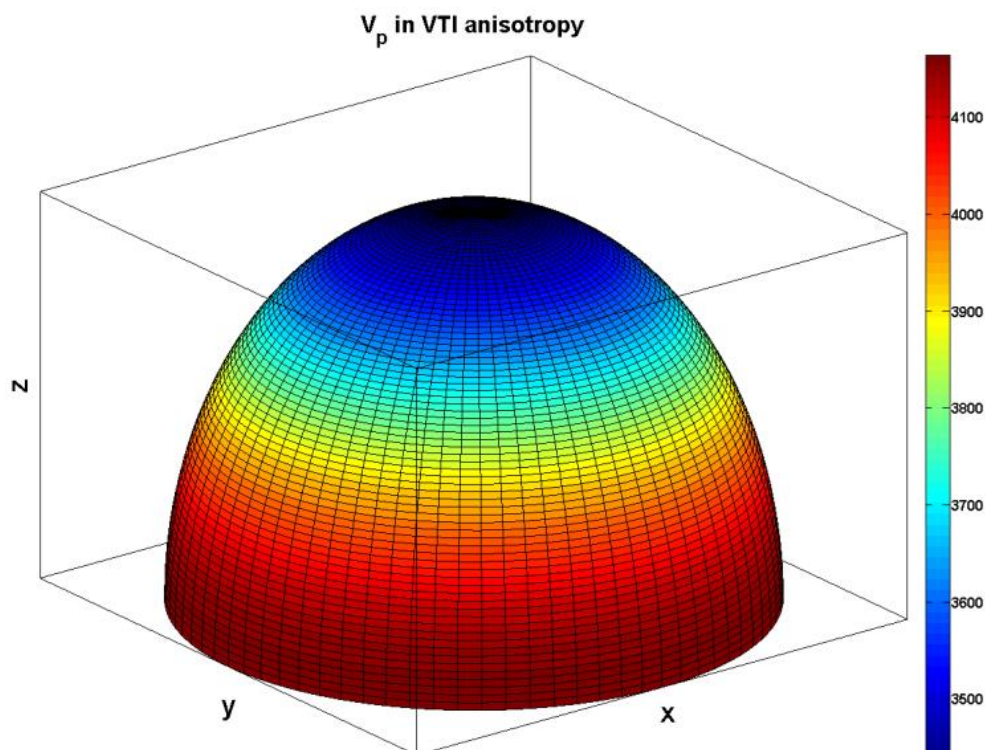


Figure 4.11, V_p in VTI anisotropy sample in different directions. z points towards the velocity in vertical direction, where x and y are horizontal direction of the VTI medium (after Herwanger and Koutsabeloulis, 2011).

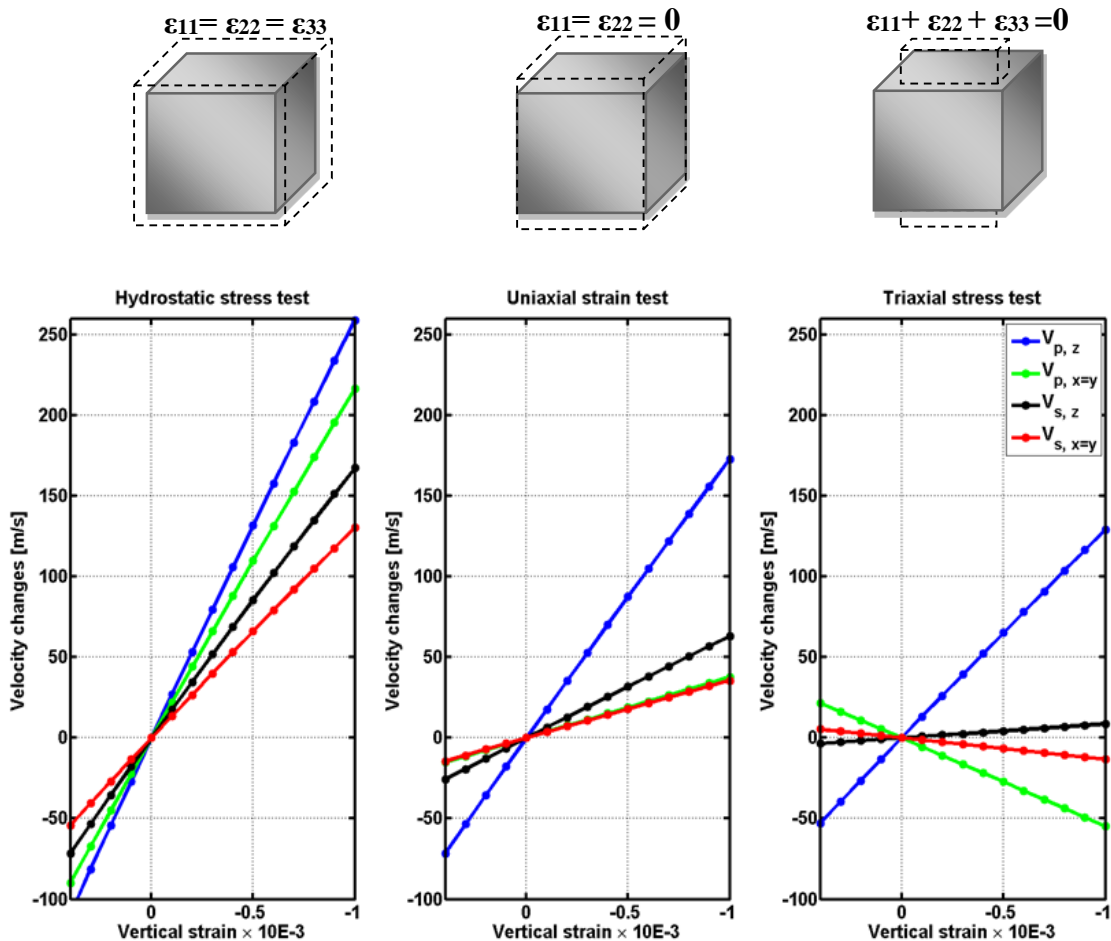


Figure 4.12, V_p and V_s in VTI anisotropy sample. Hydrostatic stress test (Left), Uniaxial strain test (middle) and Triaxial stress test (right) stress (after Herwanger and Koutsabeloulis, 2011).

In time lapse analysis we are interested in the changes in travel time and velocities. Ignoring effects of fluid on velocity changes (which was studied in chapter two and chapter three), we can calculate the velocity variations, merely due to the stress changes. Figure 4.14, for example illustrates the differences in V_p after the increase in effective stress for the VTI shale. Obviously in this figure, 10 MPa increase in effective stress is almost equivalent to 50-60 m/s velocity variation depending on the propagation direction. It worth

mentioning that, according to equation (4.7), velocity is in fact controlled by strain and not stress. This means that 10 bar increase in effective pressure might end up with significantly different results in terms of velocity changes, depending on the Young's modulus of the rock.

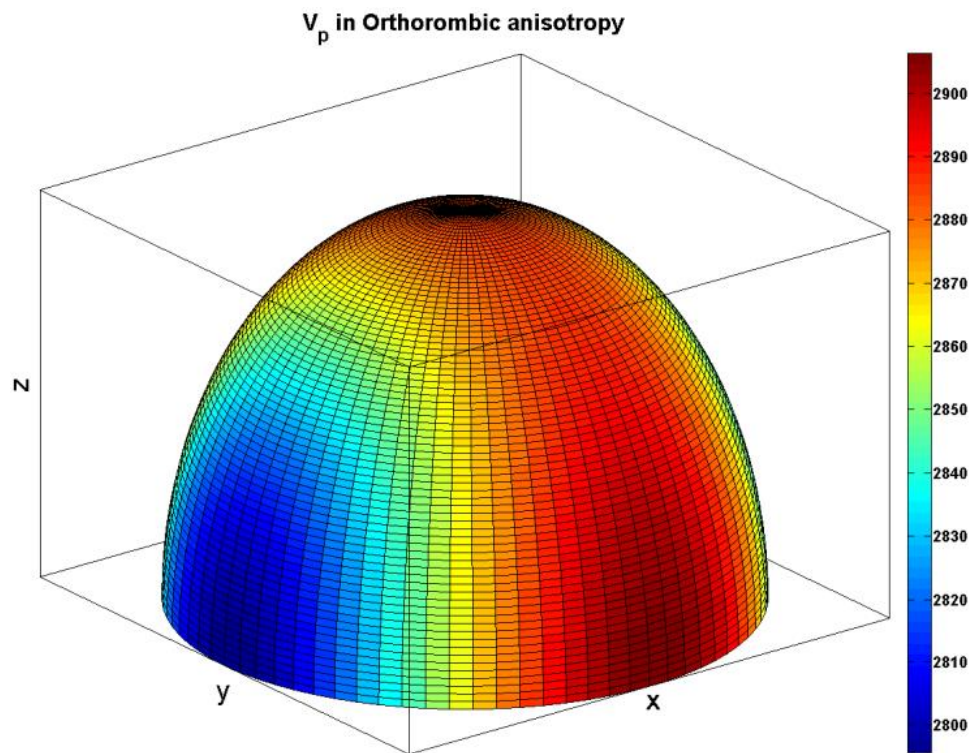


Figure 4.13, V_p in orthorhombic sample in different directions (after Herwanger and Koutsabeloulis, 2011).

Figure 4.11 to 4.13, signifies the applications of monitoring anisotropic velocity variations during the life of a reservoir. As a matter of fact, these observations have already been reported in the literature. Hall and MacBeth (2001), analysed the potential of P-wave and converted wave AVOA to detect time-lapse signatures using 4D-4C data. Van Dok et al., (2004) observed the presence of significant S-wave birefringence in the near

surface which was attributed to the local sea floor subsidence, induced by the compaction within the reservoir. Herwanger et al. (2007), investigated the anisotropy of the velocity changes and attributed them to field observations of offset-dependent time-lapse time shifts. Davis and Benson (2009), employed a time-lapse, multicomponent seismic survey to monitor tight-gas depletion for optimizing well planning and completion design.

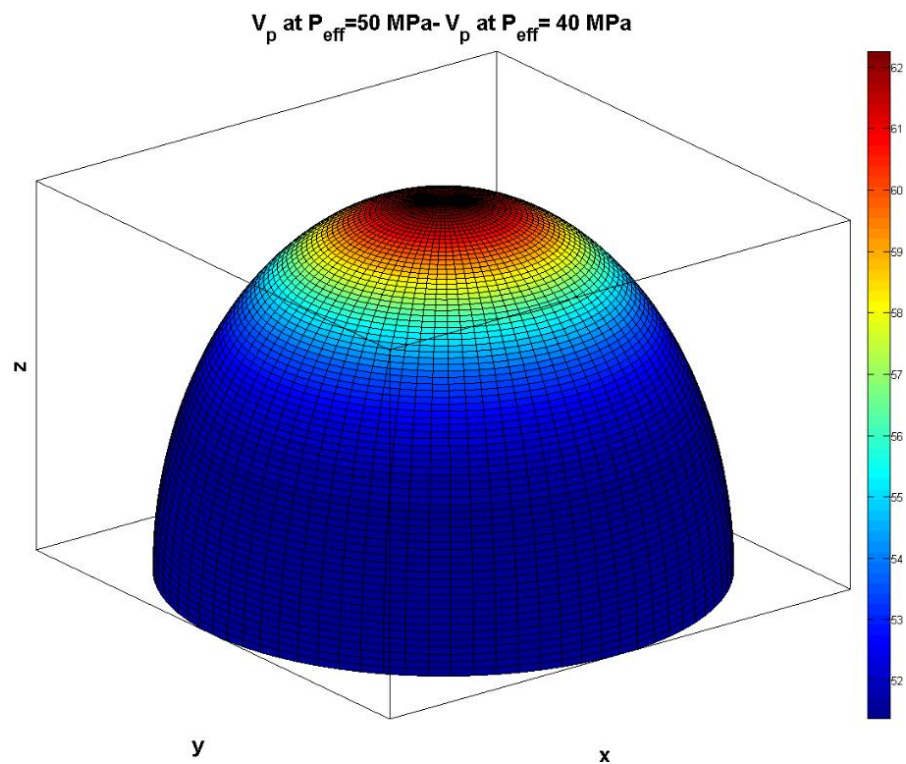


Figure 4.14, Velocity variation in different direction after increase of 10 bar in effective pressure for VTI shale sample.

4.2 Numerical simulations and case studies

In this section, a numerical model is built to investigate the influence of the pressure and temperature variations on the seismic wave velocity. I demonstrated how stress state evolves in different scenarios and how this controls the wave velocity. Saturation effects

which has been already studied is not the major concern in the current simulations. The following steps are conducted for this numerical study:

- Setting up a reservoir model, including reservoir geometry, petrophysical properties, relative permeability curves, fluid type and initial conditions,
- Running reservoir simulation with different development strategies; depletion, water flood and steam injection,
- Setting up geomechanical model with defined geomechanical properties, including Young's modulus, Poisson's ratio and yielding criteria, defined for the reservoir, overburden, underburden and sideburdens,
- Embedding the flow simulation grid model into the geomechanical grid and running geomechanical simulation to predict triaxial stress variations and displacements through the course of reservoir flow,
- Converting the flow and geomechanical simulation results to the velocity variations.

4.2.1 Model description

Dimensions of the studied reservoir model is 1200 (width) × 1200 (length) × 100 (thickness), which is buried at the depth of 1900 to 2000 meter. The reservoir has been divided to evenly spaced bins of 25 × 25 × 10 m. Two vertical wells have been modelled with 800 meter spacing, each of which has equal offset of 200 meters from the grid edges. For the isothermal model, a light oil and gas fluid model have been selected. The oil gravity is assumed to be 28 API with bubble point pressure of 160 bar. For the thermal case a bitumen (96%) and methane (4%) compound has been assumed.

For the geomechanical model, the described reservoir model is embedded into a larger grid to account for overburden, underburden and sideburdens. Figure 4.15 illustrates the side view of the geomechanical model. Geomechanical properties were defined for the reservoir and surrounding media, separately. For the reservoir, Young's modulus is 10 GPa, and Poisson's ratio is 0.3 with the thermal expansion coefficients of $1.3E-05$ (1/K) and density of 2.38 g/cm^3 . For the surrounding rocks, the Young's modulus is 30 GPa, Poisson's ratio is 0.2 with the thermal expansion coefficient of $1.3E-05$ (1/K), and density of 2.54 g/cm^3 . I assumed an elasto-plastic model with Mohr-Columb threshold for both rocks. Friction angle of 34.9° and 14.4° and dilation angle of 17.5° and 7.2° , are assigned for the reservoir rock and surrounding rocks, respectively.

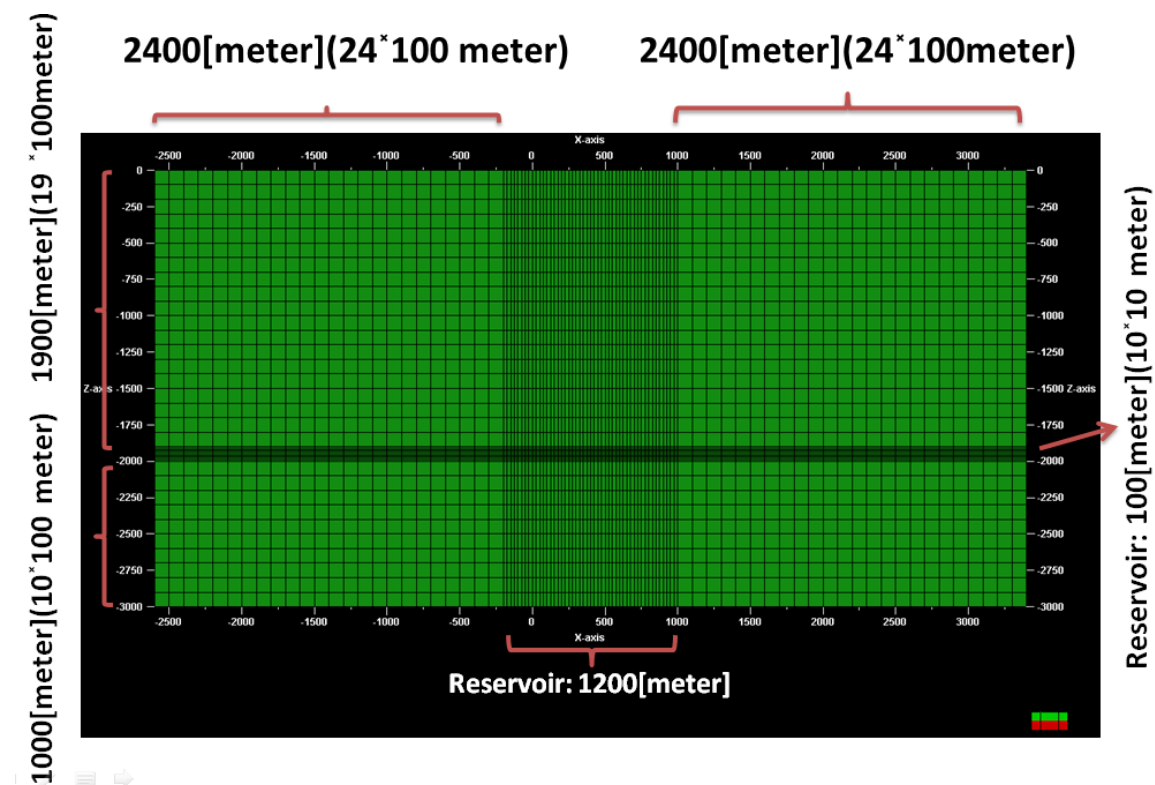


Figure 4.15, Side view of the reservoir geometry, embedded in the geomechanical earth model.

Two production strategies were studied. In the first scenario the production well was set to produce for 5 years. After 5 years an injector well starts to inject the water for the next five years along with production from the producing well. In the second scenario, the production and injection timing is similar to the first scenario, however the injector injects hot steam of 234° C for 10 years starting at 2015.

Figure 4.16, illustrates the pressure changes after five years of production. The initial pressure at the reservoir depths was 158 bar. The corresponding changes in pressure and saturation have been converted to the V_p at 2015, using Gassmann's equation, and the results are presented in figure 4.17. At this figure only fluid variations have been taken into account and stress effect is ignored. Note that V_p has been reduced due to the gas evolution. Beginning of 2015, the injector well starts injecting water, which in turn builds up pressure. Pressure and V_p variations at the end of simulation time (2020) are delineated in figure 4.18 and 4.19, respectively. Note that velocity has increased around the injector, due to high pressure, replacement of oil by water which has larger elastic moduli and most importantly the absence of gas.

The flow simulation result is passed to geomechanical simulator in the next step. Figure 4.20, illustrates, variation in effective stress in the vertical direction. The grid plot, represents the stress changes in the reservoir at 2020 after 5 years of water injection (2010-2015) and 10 years of production (2010-2020). In this figure, top plot shows the variation of effective stress along the wells within the reservoir, where the bottom one displays similar plot in the overburden. Note the opposite behaviour of the overburden and the reservoir in these two plots.

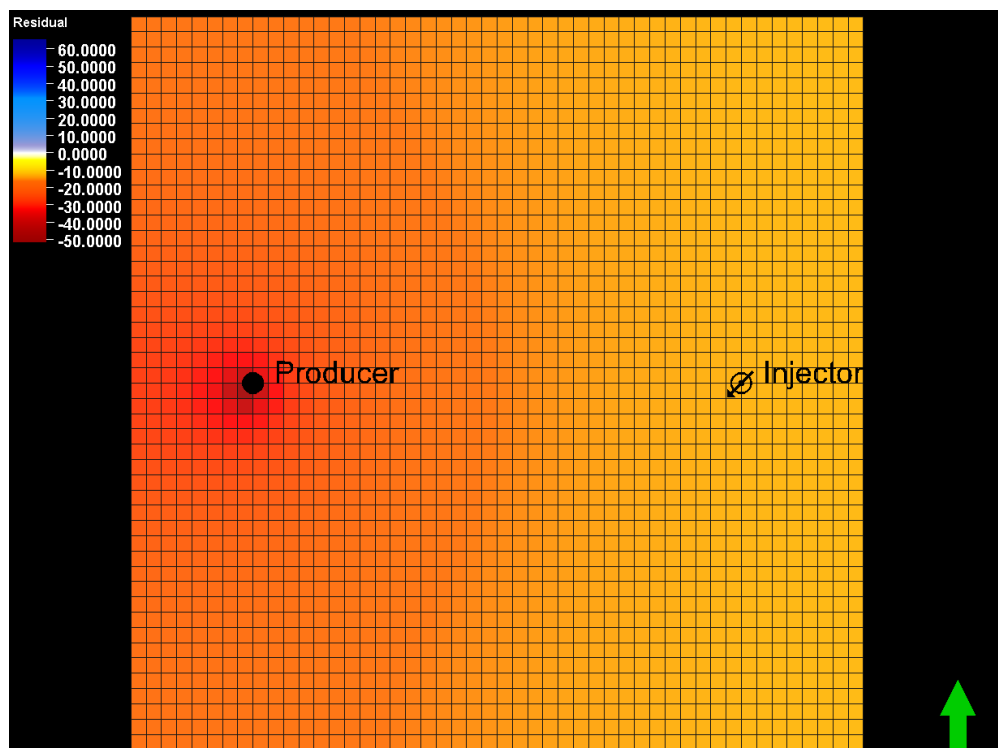


Figure 4.16, Pressure variations from 2010 to 2015, when only producer is open.

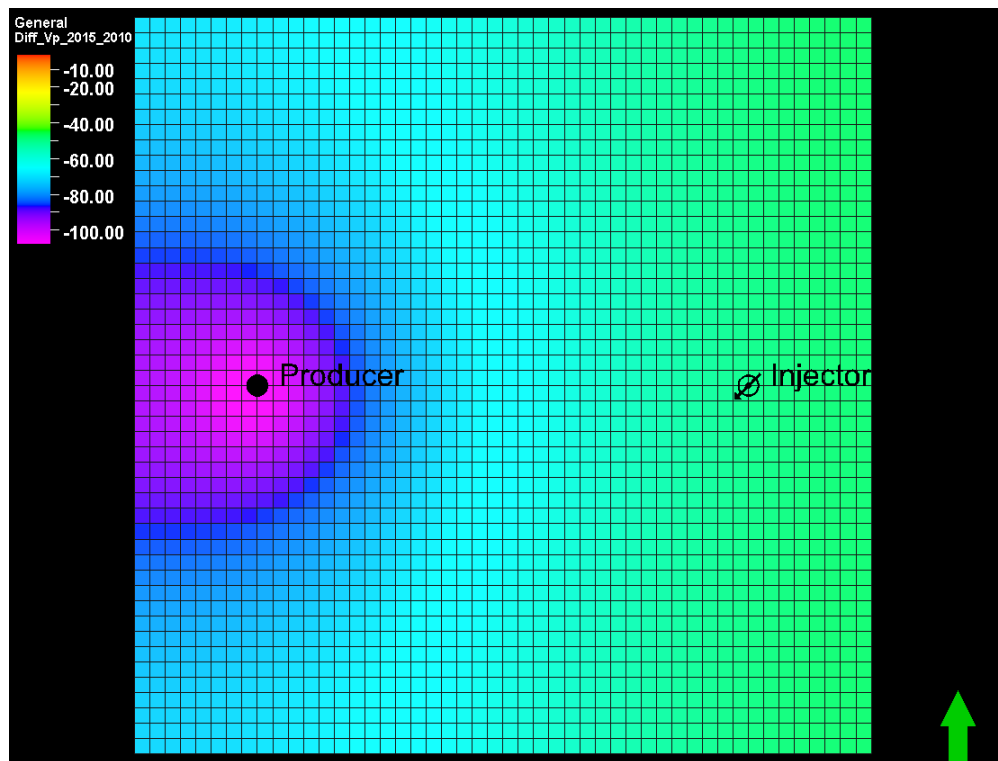


Figure 4.17, P wave velocity variations from 2010 to 2015, when only producer is open.

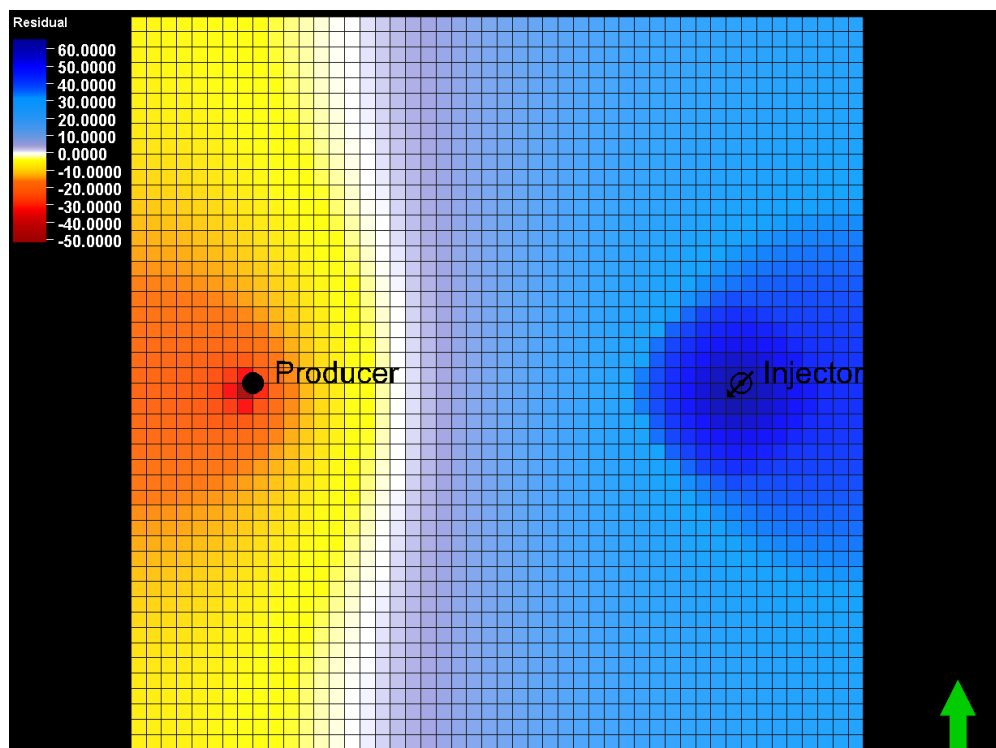


Figure 4.18, Pressure variations from 2010 to 2020, producer and injector are open.

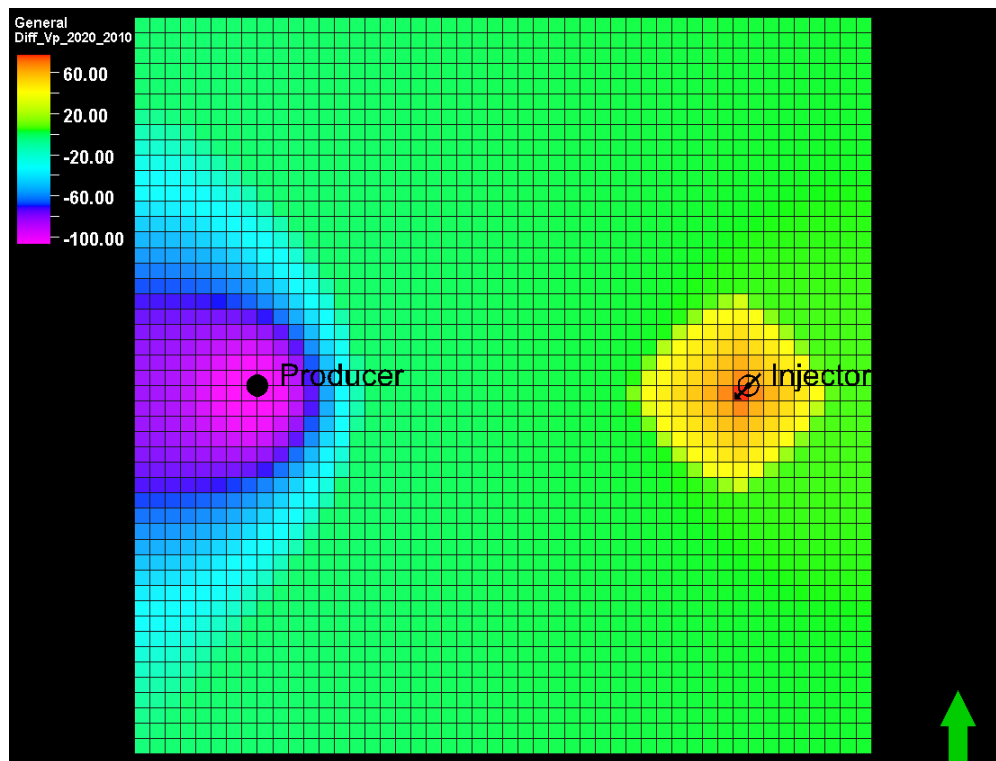


Figure 4.19, P wave velocity variations from 2010 to 2020, producer and injector are open.

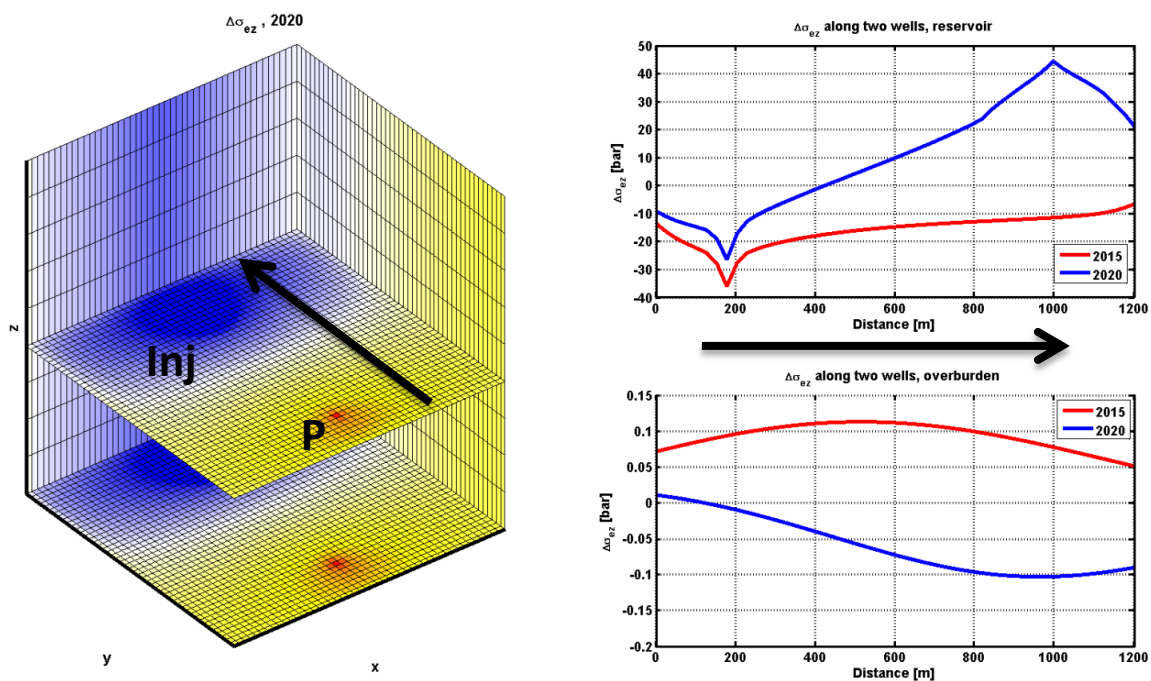


Figure 4.20, Grid plot shows the variation in effective stress in the vertical direction. Red color corresponds to increase in compressional stress (negative) while blue color shows reduction in compressional stress (positive). Top plot shows the variation of effective stress along the wells in the reservoir, where the bottom plot shows the variation of effective stress along the wells in the overburden.

In the next step, results of the geomechanical simulator are converted to the velocity variations, using the explained algorithm in the previous section. I assumed the reservoir rock to be similar to VTI behaviour of Colton sandstone, surrounded by the Jurassic shale. Figure 4.21, shows the velocity variations in principal directions from 2010 to 2015 in the reservoir and overburden where figure 4.22 shows similar plots from 2010 to 2020. Note that changes in reservoir and overburden have opposite signs with respect to velocity variations.

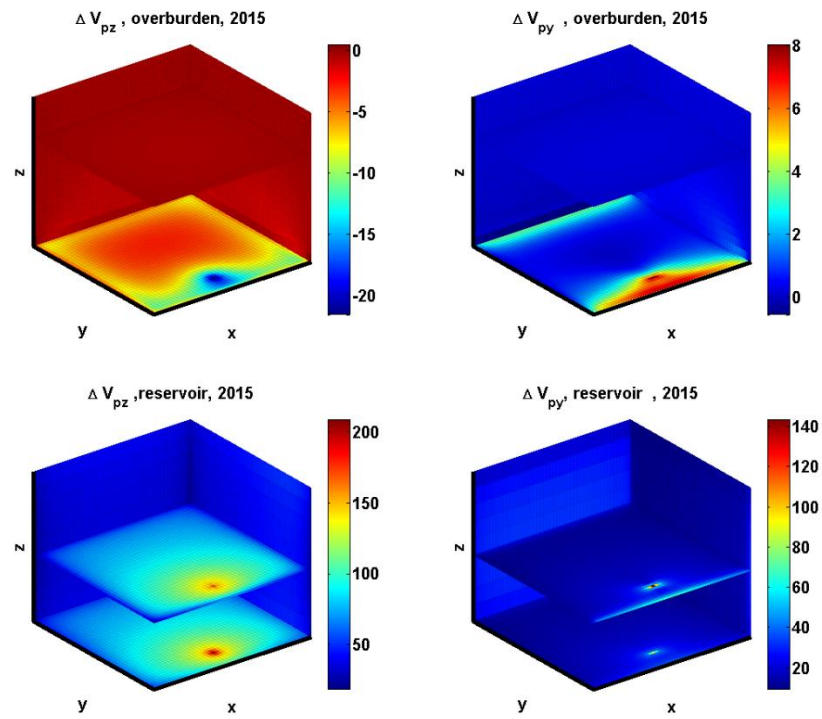


Figure 4.21, P-wave Velocity variations in principal directions from 2010 to 2015.

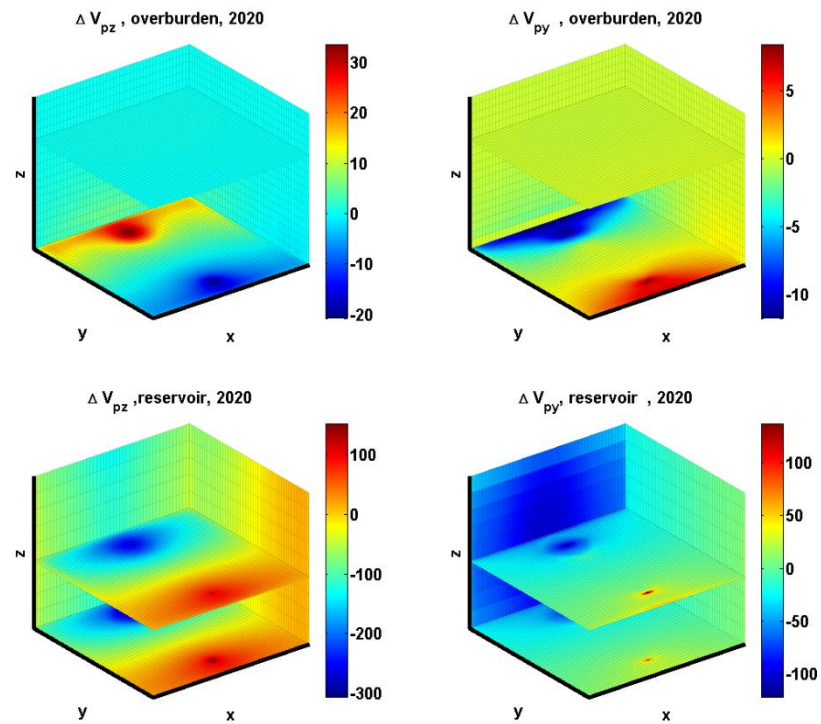


Figure 4.22, P-wave Velocity variations in principal directions from 2010 to 2020.

4.3 Geomechanics in thermal cases

This section is an attempt to bring up another mechanism involved in the thermal production, which impacts seismic monitoring and has been less appreciated. Geomechanical drivers induced by thermal recoveries, turn out to have quite complex influences on all aspects of seismic wave propagations. I try to single out different mechanisms in order to study them separately to perceive the subtle outcome.

Here in the second scenario, the injection is conducted using hot steam rather than water for 10 years (2015-2025). This triggers a thermal stress mechanisms, in addition to the discussed induced stresses, so far.

There are many articles describing case studies, laboratory measurements and numerical studies about the thermal effects on seismic velocities from fluid variation perspectives, which have been pointed out in the previous chapters. However there are very little literature available about the impacts of thermal induced stress on seismic wave velocities in the reservoir. Dusseault and Collins (2009) pointed out the existence of the thermal induced stresses in the reservoir that causes thermal induced shearing or failure mode and can occur when the anisotropic stresses in the rock exceeds its frictional and cohesion strengths. This shear failure can result in increasing the porosity and enhancement of permeability. Guy et al., 2013, studied a numerical SAGD model, with geomechanical-flow coupling method to show the effects of the thermal production on seismic velocities around the wells.

If we heat a bar with length L , the change in length ΔL , can be calculated using $\Delta L = \alpha_L L \Delta T$, where α_L is the linear thermal expansion coefficient, L is the initial length and ΔT is temperature change. If the bar is bounded at both ends it will be unable to expand and

builds up an internal stress according to $\sigma = E\varepsilon$, where σ is stress, E is Young's modulus and $\varepsilon = \Delta L/L$ is the strain. Equating the two equations, $\sigma = E \alpha_L \Delta T/L$ results in the following thermal induced equation for stress:

$$\sigma = E \alpha_L \Delta T \quad (4.12)$$

where E is Young's modulus, α_L is the linear thermal expansion coefficient, ΔT is the change in temperature and σ is the resultant thermal induced stress.

Increasing temperature of the reservoir is similar to adding extra load of overburden and sideburdens. Heating causes the effective stress to become more compressive due to thermal expansion of the rock matrix according to equation (4.12). This causes the rock matrix to expand, which is opposed by the surrounding rock that impose a compressive stress. The induced stress usually is remarkable in horizontal, since the opposing boundaries are quite firm where in the vertical direction the induce stress can relax by overburden displacement, provided that the reservoir is shallow.

This impact can be seen by comparing induced stresses in two different scenarios. Figure 4.23, shows the production/ injection impacts on vertical effective stress. Recall that in the selected convention, blue shows reduction and red represents increase in effective stress. In figure 4.23, before 2015, where the only disturbing well is the producer, the effective stress has been increased (smaller negative number, which means increase in compressional stress). Starting from 2015, when injection starts, increase in pore pressure results in generation of a new low effective stress front that gradually moves away from the injector well, outwards in all directions.

In figure 4.24, we expect to observe a similar stress system to the figure 4.23, before 2015, since the injector is shut in this period. This is correct where the pore pressure and

viscosities are the same, which is not the case due to different fluid models used in the two scenarios. At 2016, a year after steam injection, a significant compressional stress has been produced around the hot injector. This is superposition of the opposing thermal induced stress which tends to increase effective stress and pore pressure induced stress which tends to decrease effective stress. In the next years, the system of low effective stress which is raised because of pore pressure increase, has been clearly distinct. This pressure front is in principal similar to the front in figure 4.23, which travels faster than the red thermal front. Note that these two fronts are opposing each other and as a result we see a zero change stress boundary (white color between red and blue fronts) separating these two regions.

Pressure diffuses based on the Darcy's law and its flux is controlled by rock permeability and fluid viscosity as well as pressure gradient. From the other hand Fourier's law governs the heat diffusion which triggers thermal stress. Heat flux is a function of temperature gradient and thermal conductivity of rock and fluid. This explains why, pressure and thermal induced stresses travel with different velocities. This fact causes pressure stress front (blue) to drift away gradually from the red thermal front.

Considering velocity variations which are measurable parameters, note that velocity is a function of stiffness tensor according to equation (4.10). These tensors themselves are functions of strain, according to equation (4.7). This means that stress analysis should be converted to strains eventually, to measure the velocity variations. In other words this is Young's modulus and thermal expansion coefficient that will dictate the velocity variations, NOT stress variation only.

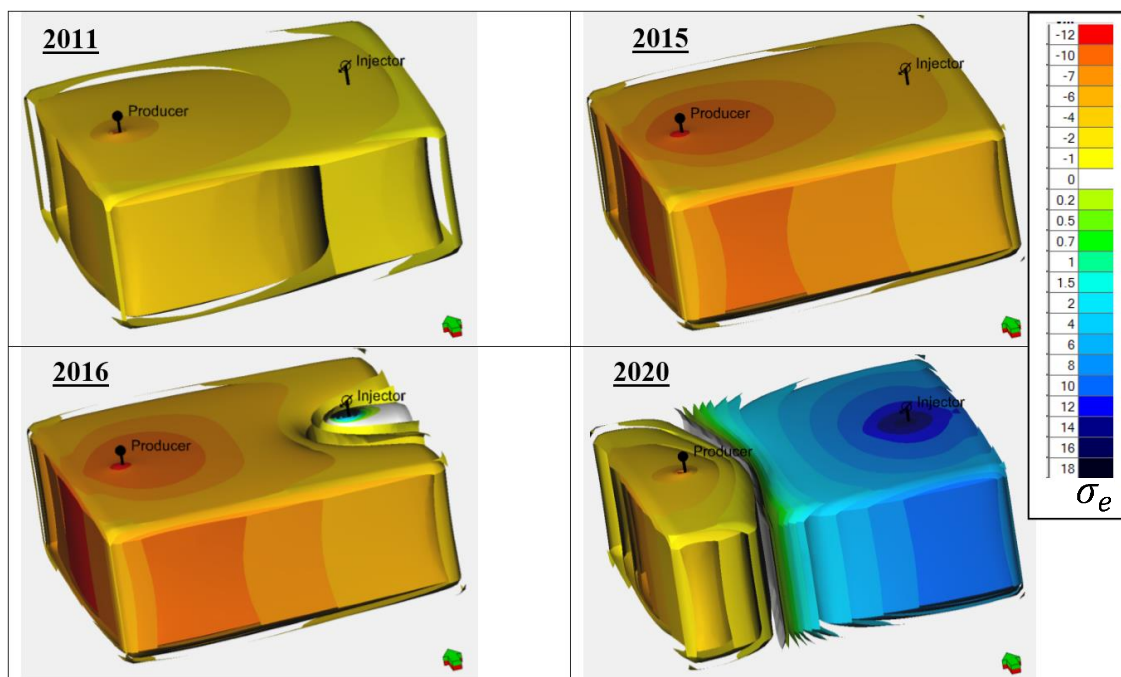


Figure 4.23, Effective stress variations during the water injection scenario. production starts at 2010, where injection starts at 2015. Both wells are open till 2020.

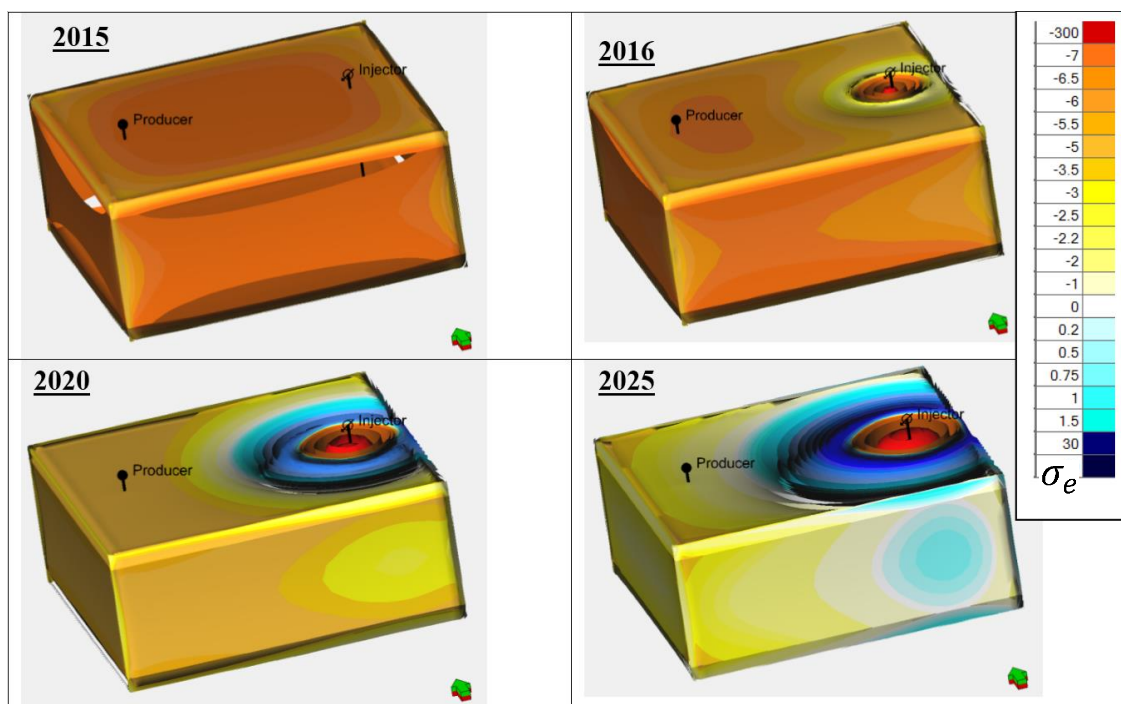


Figure 4.24, Effective stress variations during the steam injection scenario. Production starts at 2010, where injection starts at 2015. Both wells are open till 2025.

4.4 Results and discussions

Coupled geomechanical-flow simulation is proved to be powerful, and essential to model and hence, predict the time-lapse time shifts. This time shift is simpler to be analysed above the reservoir, since it has not been impacted by the fluid developments. For example in production wells, seismic wave slows down in the overburden ($twt_{new} > twt_{old}$) and speeds up within the reservoir ($twt_{new} < twt_{old}$), ignoring the fluid impacts on velocity. It means that, time shift seen at the base of the reservoir is in fact the superposition of two opposing mechanisms within and above the reservoir. Considering that there is thicker overburden compared to reservoir interval, one expect to see an overall time lag at the base of the reservoir, in general. Taking fluid contribution into account, makes the evolved gas or injected steam an influential parameter in time lag increase in the reservoir. This fact will further mask the negative time shift mechanism of the seismic wave at the base of the reservoir.

It was demonstrated that reservoir equilibrium disturbance by production or injection, will generate stress momentums that impact seismic wave velocity accordingly.

The detailed inspection of the velocity variations during reservoir life is difficult due to the coupling of the dominating events. In other word, change in pressure and temperature, changes the elastic constants, and thermal expansion coefficients of the rocks and fluid. These two parameters control the stress and strain of the system and govern the velocity of the seismic wave. The amount of changes is dictated based on the rock properties. For example the stiffer the rock, the less velocity variations due to induced stress.

Seismic velocities and impedances decrease only slightly in rocks saturated with gas or wet water as temperature increases (Timur, 1977; Wang and Nur, 1990 b). I showed in

previous chapter that, the wave velocities in heavy oil saturated rocks are quite sensitive to the temperature variations. Wang and Nur, (1990 b) showed that both compressional and shear velocities might reduce by as much as 40% for different heavy oil saturated sands, with increasing temperature. This kind of temperature influence on velocity has also been reported by Kato et al. (2008). Temperature, also will introduce gaseous phase in the form of evolved gas or steam, which tends to significantly reduce the seismic velocity. As a matter of fact this gives a powerful measure for steam chamber monitoring using 4D time lapse data. However, Sung et al. (2009) suggested that if free gas is available before steam injection, the velocity change after steam injection is as low as less than 3%.

Second aspect of temperature influence is the induced thermal stress. Thermal stress is the result of expansion of the medium which is opposed by bounding rocks. This stress is controlled by elastic moduli and coefficient of thermal expansion of the rock. Increasing temperature results in adding thermal stress to the system that is equivalent to have bigger load, which translates to increase in confining total stress and consequently increase the effective stress and velocity. Despite this, it is common observation to see a velocity decrease in SAGD operations during steam injection (for example Nakayama et al., 2008). This is the result of significant velocity reduction due to transforming solid like heavy oil to the liquid like fluid. Injected steam and released gas also will definitely slows down the propagating wave further. The current forward modelling was an effort toward resolving these distinct drivers.

4.5 Summary

In this chapter I emphasized the importance of stress variations during the course of production and was shown that it can significantly influence the time-lapse seismic

responses. These stress-induced velocity changes can be even higher than the changes in velocity due to the fluid substitution, depending on the rock's property.

In terms of pressure impacts, reservoir depletion causes pressure decline, which in turn leads to increase in effective pressure within the reservoir and velocity increase. On the other hand, injection increases the pore pressure and reduces effective pressure. This will result in a decrease in effective stress and hence, decrease in velocity.

Introducing heat to the system will complicate the elasticity of the rocks furthermore. On one hand it changes the pore pressure and saturations depending on the PVT properties of the pore fluid. In addition, injected steam will significantly reduce the velocity itself due to the low velocity nature of steam. On the other hand thermal injection will add total stress which will act like an additional thermal load due to the expansion of the rocks and resistance of overburden. This will result in increases in effective stress in the reservoir and wave speeds up accordingly. Nonetheless, the velocity speed up usually is masked due to the injected steam and evolved gas which tend to impede the propagating wave.

The stress effects are also observed in the host rock in addition to the reservoir. Overburden for example, resists to the changes in the reservoir. It means that shrinking the reservoir due to pore pressure reduction, will result in stretching the overburden, and velocity decrease accordingly. This behaviour is reversed in injection, where expansion of the reservoir is opposed by overburden, which will tend to speed up the velocity as a result.

In addition to the reservoir fluid parameters (saturation, pressure, temperature), and rock properties (elastic moduli, thermal expansion coefficient), the reservoir thickness also is a key factor. Needless to say that the resultant time shifts at the base of the reservoir, is the superposition of all the impacts that a wave experiences while propagates through the

reservoir and overburden. The longer the path in the reservoir, the larger is the impact on wave travel time.

Chapter Five: Case study

Thus far, the general scheme to convert simulation outputs to seismic impedance (Sim2Seis) for enhancing reservoir history matching, has been discussed. Furthermore, considerations with respect to viscoelastic fluids as well as stress substitutional models were studied. In this chapter, Sim2Seis approach is implemented on a reservoir. The available data are well logs, and seismic survey for a reservoir undergoing CHOPS production. There are no static or dynamic model available. This made a big challenge since, I had to address subtle tasks of a geophysicist, a geo-modeller, a reservoir engineer, and a software developer to reach to the point to be able to assess the idea of Sim2Seis. In this chapter, major implemented steps during the case study are explained with some details. The outline are as follows, and the terms in parentheses are software packages used:

- Data loading and QC (HRS, CGG; PETREL, Schlumberger)
- Well seismic tie and horizon interpretations (HRS)
- Survey calibration of the base and monitor seismic surveys (HRS-Pro4D)
- Post-stack and pre-stack inversion (HRS-Strata)
- Reservoir characterization and porosity estimation (HRS-Emerge)
- Velocity modelling (PETREL)
- Structural modelling of the reservoir (PETREL)
- Geostatistical variogram analysis (PETREL)
- Reservoir static geo-modelling (PETREL)
- Reservoir dynamic simulation (ECLIPSE, Schlumberger)
- Sim2Seis development (Ocean SDK, Schlumberger; C#, Microsoft Visual studio)
- Analysis and results (PETREL)

5.1 Field and data description

Primate is a heavy oil reservoir operated by Enterra and Equal Energy. This field is located within the heavy oil belt reservoirs in Western Canada field in Saskatchewan, Canada (Figure 5.1). Main production zones in this field are McLaren and Waseca formations which are parts of Mannville group in the area. This stratigraphic reservoir produces from a pay zone with a variable thickness between 5 m to 12 m, with no record of active water drive or available gas cap during the drilling.

The available data for this case study were as follows:

- Seismic data: a base 3D survey (2004) and a monitor 3D survey (2009)
- Well head information, well logs, well tops
- Reservoir production data (water, oil, and gas rates)

CHOPS (Cold Heavy Oil Production with Sand) technology is employed on this reservoir. In this process, the recovery is enhanced by producing sand and fluid altogether, using special pumps. Developments of the high porosity channels (wormholes) as the result of extreme sand production, make the dynamic simulation quite challenging, because the flow simulator simulates the fluid phase only and not the solid phase. Although, there are some simulators that are capable in dealing the sand production, the wormholes are still quite complicated to model.

Unfortunately, two important data type are missing which limits us to use conventional Gassmann's substitutional model in this study. Firstly, there is no viscoelastic fluid measurements (required for viscoelastic fluid substitutional models) and the other one is leak-off test which is needed to characterize stress regime in the reservoir (required for stress substitutional models).

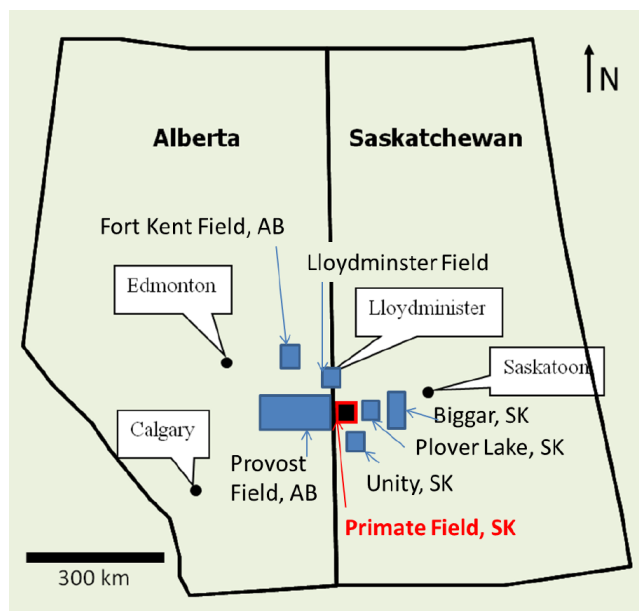


Figure 5.1, Location map of the primate field.

5.2 Horizon interpretation and survey calibration

Once the data, were loaded to the software project, I needed to come up with a reasonable time depth relationship to identify the seismic horizons using the well tops. There were no check shot available for this field so I tried to generate a reasonable tie using the available sonic data. Figure 5.2, illustrates the extracted statistical wavelet in a 350 msec window above the reservoir. With the obtained time depth relationship it was not only possible to interpret the horizons but also to present the well traces, well tops and well logs in the time domain.

The next step was to calibrate two seismic surveys in terms of amplitude, frequency contents, time shifts and phase differences with the aim of removing energy and phase differences and preserving the discrepancies as the production fingerprint.

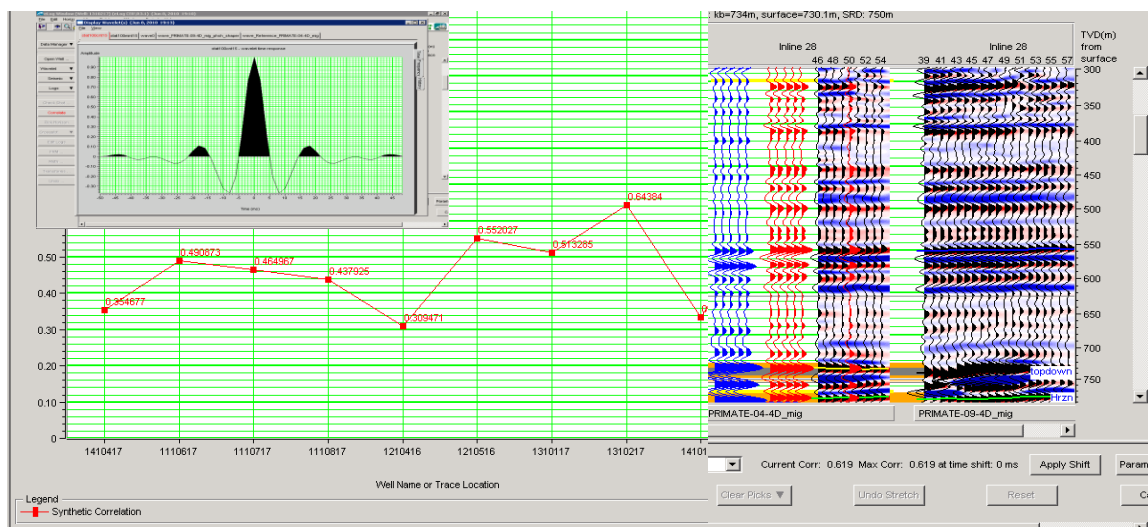
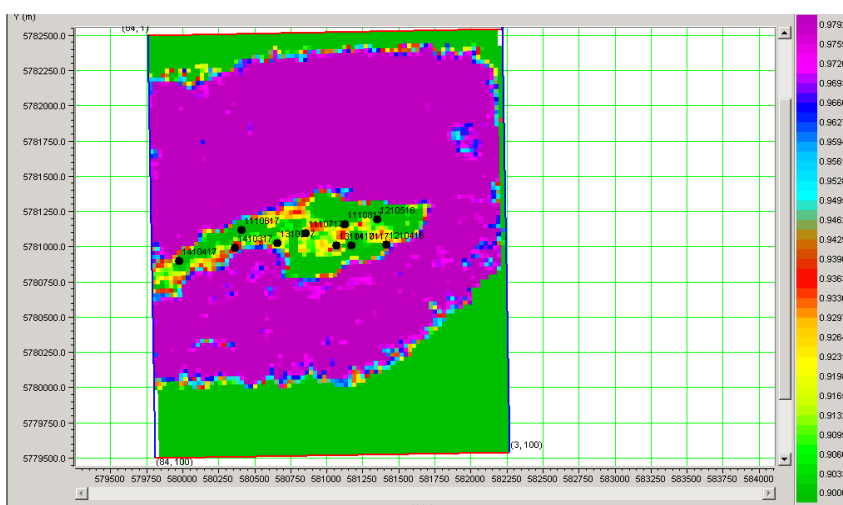


Figure 5.2, Statistical wavelet, correlation coefficients between synthetic seismogram and seismic trace at every well, and a sample seismic-well-tie.

Figure 5.3, shows the maximum cross correlation between the base and the monitor survey at 10 msec below the reservoir top after survey calibrations. Obviously the minimum similarity between base and monitor surveys are seen in the reservoir interval which is due to production. This map can be an indicator of reservoir boundary as well. The reservoir boundary defined here is also consistent with Sweetness attribute shown in figure 5.4, which is used for identification of features where the overall energy signatures change in the seismic data. Another way to identify the production induced reservoir changes is to plot amplitudes of monitor seismic data versus base seismic data. The idea is that two data set should line up along the $y=x$ line, except the differences between two surveys which will be isolated as clustered outliers and are attributed to reservoir production. This plot is shown in figure 5.5. Showing only the clustered data, represent the reservoir volume clearly. Similarity of the figure 5.3, 5.4 and 5.5 indicates that most likely the highlighted region in these figures is the reservoir boundary.



5.3 Post stack and pre-stack seismic inversion

5.3.1 Post-stack inversion

Since the objective is to compare the modelled and real seismic data at acoustic impedance level, it is required to invert both base and monitor seismic data. Two different post stack inversion techniques were implemented, namely *band-limited* and *model-based* inversion.

The band-limited method is a simple recursive approach, in which the wavelet is assumed to be zero phase. This method works best where there is a good signal to noise ratio. Band-limited inversion can be considered as an integration of seismic traces and then exponentiating that. Hence, in presence of noise the accumulation of noise amplitudes will be significant, especially in longer travel times. Another deficiency is that band-limited inversion considers the side lobes of the wavelet as lithological variations which do not really exist.

In the model-based inversion we employ geological information from logs parallel to the seismic data, as a guide. This reduces the inherent non-unique nature of seismic inversion. The highest concern here, is the sensitivity of inversion algorithm to the initial model, which is uncertain itself. This dependence in well locations is not a big deal since we have reliable control points. However between wells, one must have a reasonable starting model that roughly represents existing complexities of the reservoir.

Figure 5.6 through figure 5.9 show the results of both inversion schemes on the base case (2004) and the monitor case (2009). Differences in the reservoir interval between the base and monitor survey can be attributed to the reservoir production. The square of difference between two surveys is illustrated in figure 5.10 and figure 5.11.

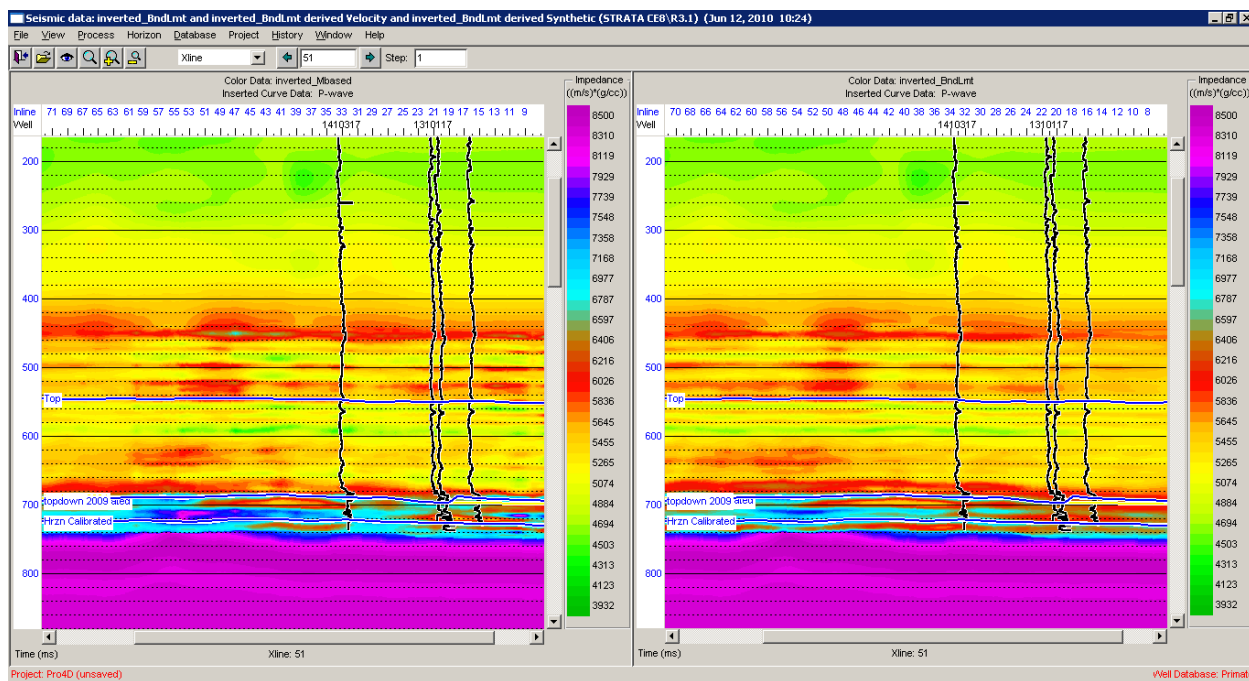


Figure 5.6, Model-based inversion (left) and band limited inversion (right) results on the base case seismic survey (2004).

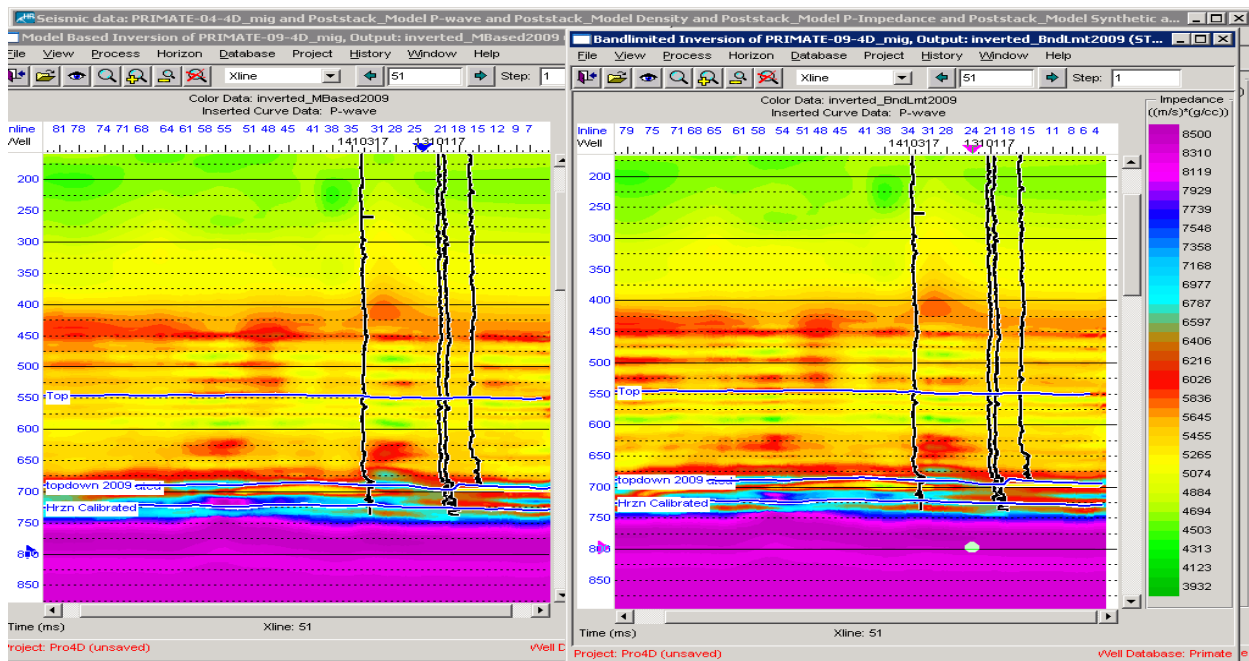


Figure 5.7, Model based inversion (left) and band limited inversion (right) results on the monitor seismic survey (2009).

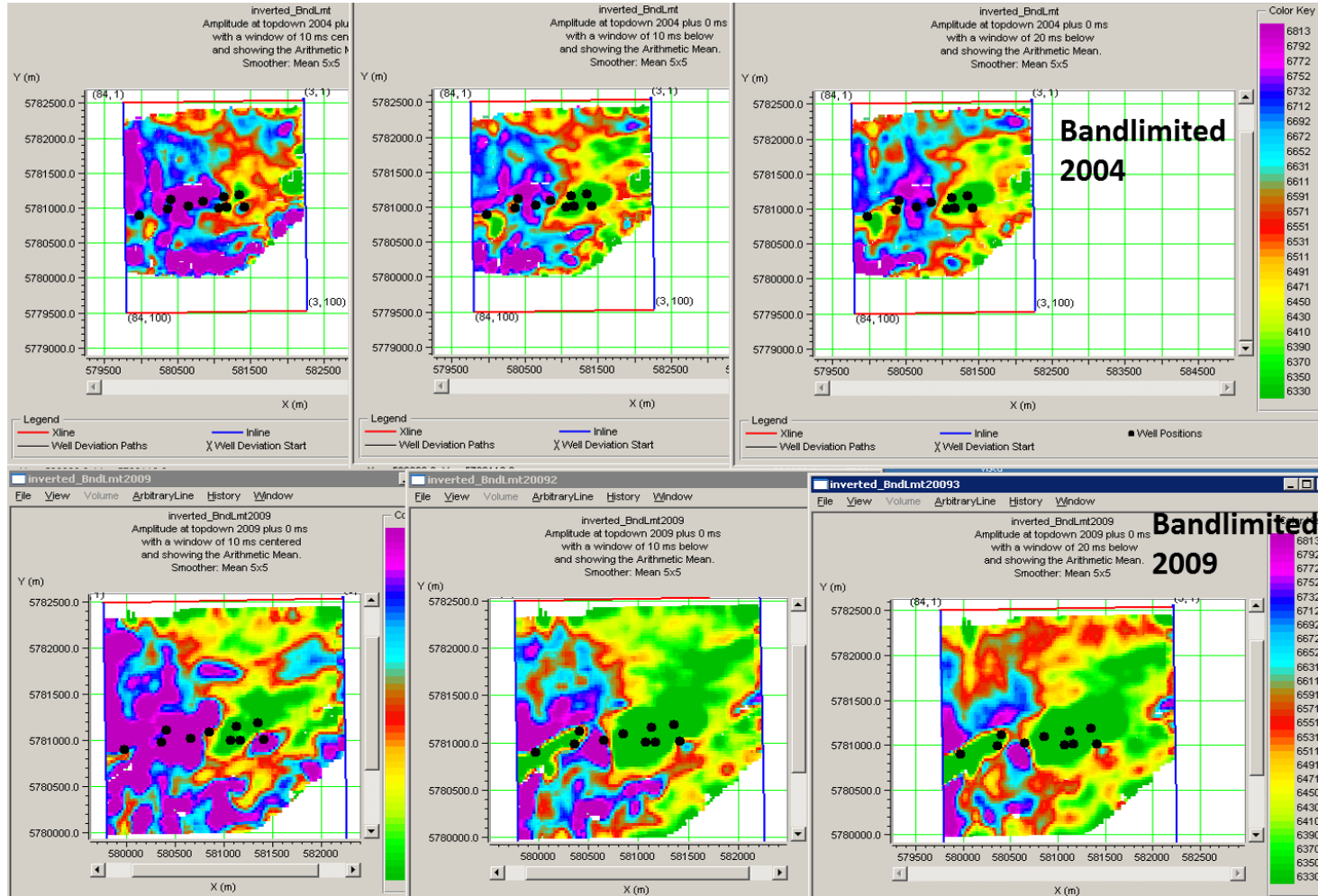


Figure 5.8, Map of the band limited inversion results in base (upper row, 2004) and monitor (lower row, 2009) cases. Maps are representing the arithmetic mean of P-impedance in 10 millisecond window centered at the reservoir top (left column), 10 millisecond window below the reservoir top (middle column) and 20 millisecond window below the reservoir top (right column).

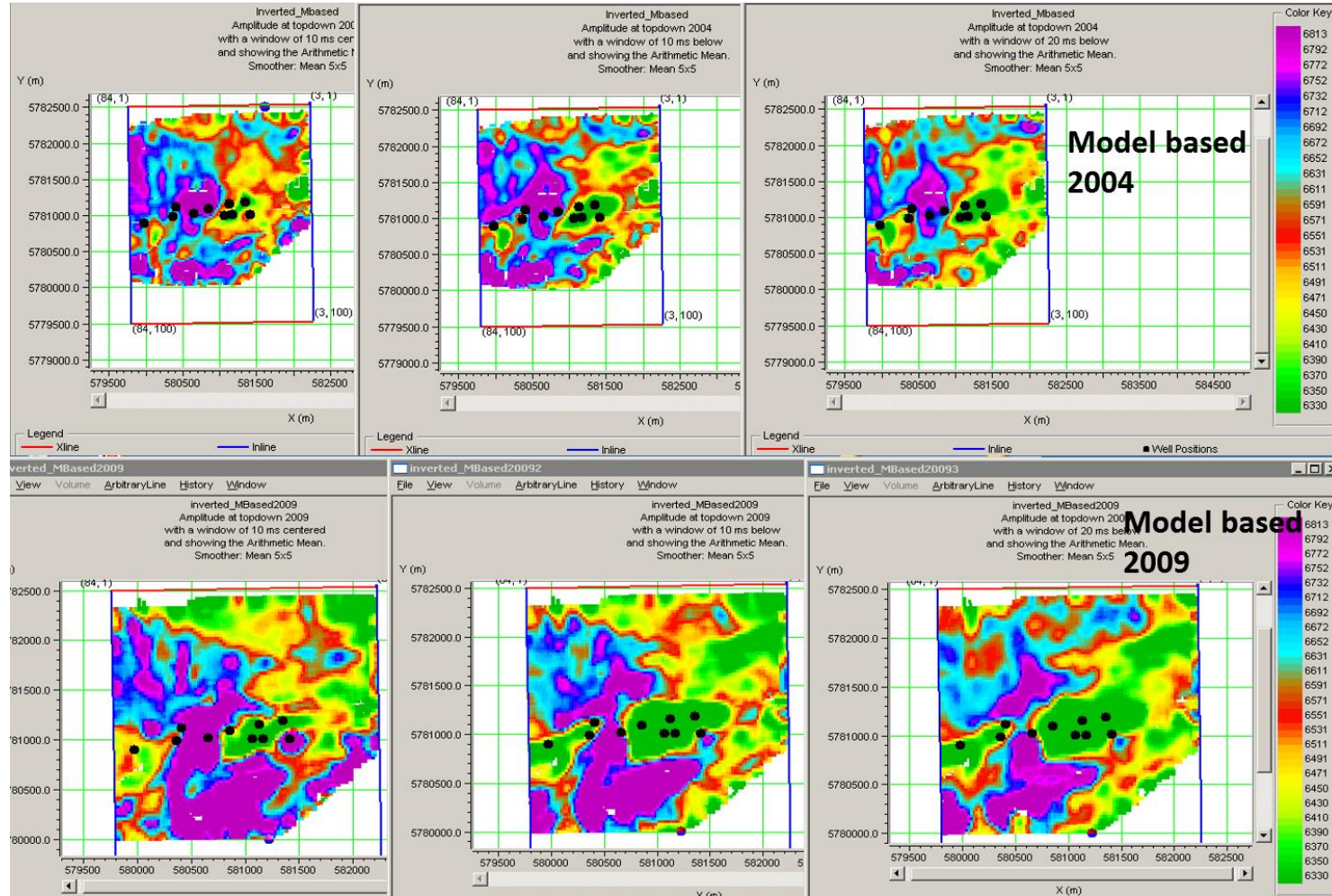


Figure 5.9, Map of the model based inversion results in base (upper row, 2004) and monitor (lower row, 2009) cases. Maps are representing the arithmetic mean of P-impedance in 10 millisecond window centered at the reservoir top (left column), 10 millisecond window below the reservoir top (middle column) and 20 millisecond window below the reservoir top (right column).

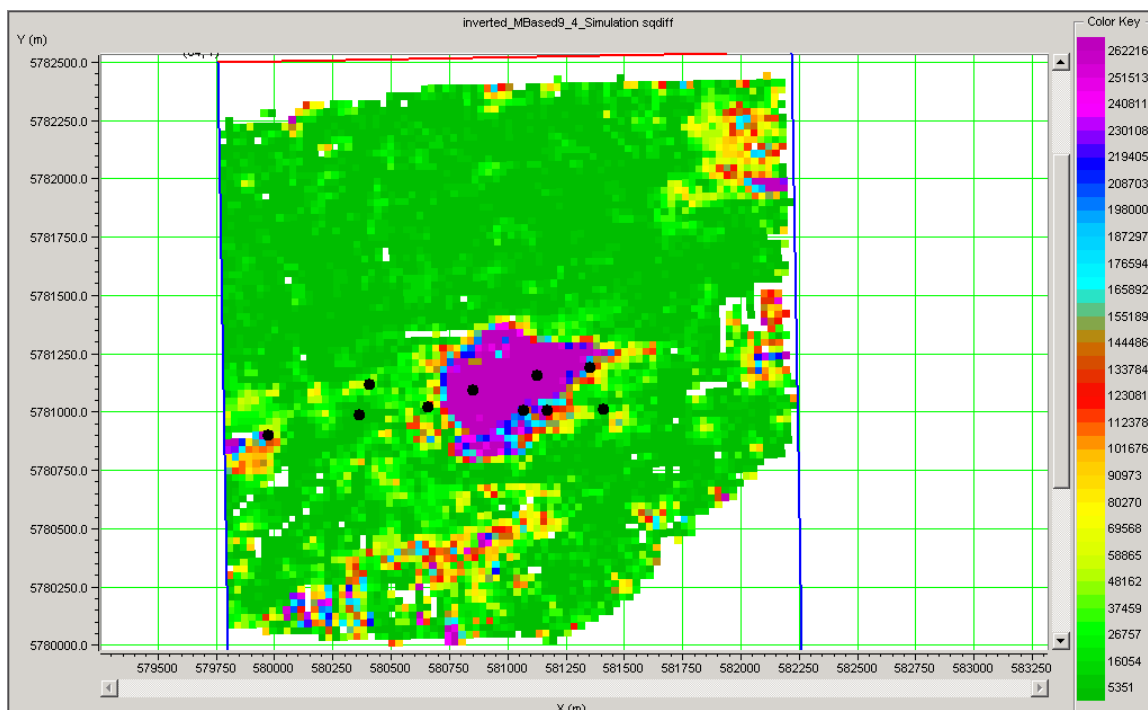


Figure 5.10, Square of the difference of band limited inversion results in monitor and base case, $(I_{p2009}-I_{p2004})^2$

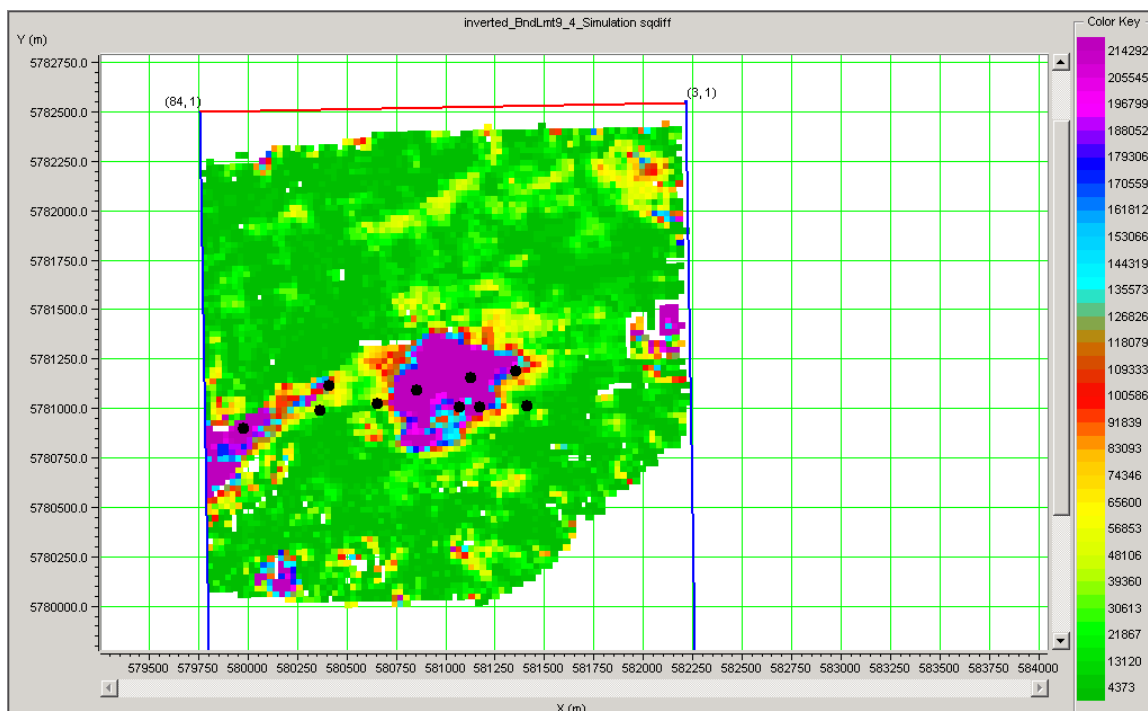


Figure 5.11, Square of the difference of model based inversion results in monitor and base case, $(I_{p2009}-I_{p2004})^2$

5.3.2 Pre-stack inversion

The next step in this case study is to perform pre-stack inversion. The goal is to extract, density as well as shear velocity information for the reservoir. The extracted V_p and V_s also will be employed in the calibration of the petro-elastic models. This inversion has been only applied on the base case to obtain the initial elastic moduli, required for calibration.

In the Pre-stack inversion the idea is to incorporate more data (all shot gathers rather than their stacked section) in the inversion of a reflection point, which in turn will reduce the ambiguity of the non-unique solution of the model parameters. In addition, simultaneous modelling of V_p and V_s allows us to predict fluid properties of the reservoir. Figure 5.12 represents a typical shot gather loaded for the prestack seismic inversion.

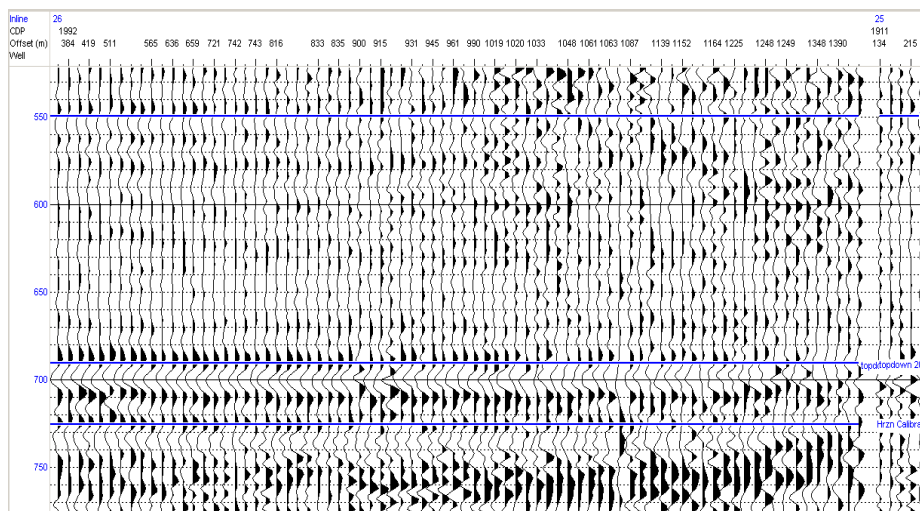


Figure 5.12, Raw shot gather loaded for the prestack inversion.

In order to prepare the shot gathers for the pre-stack inversion, a few processing steps are recommended to be implemented. The workflow is presented in figure 5.13. This processing workflow aims to enhance the overall signal to noise ratio. In this regard a high cut band-pass filter ensures the removal of the noise frequencies, followed by a super gather

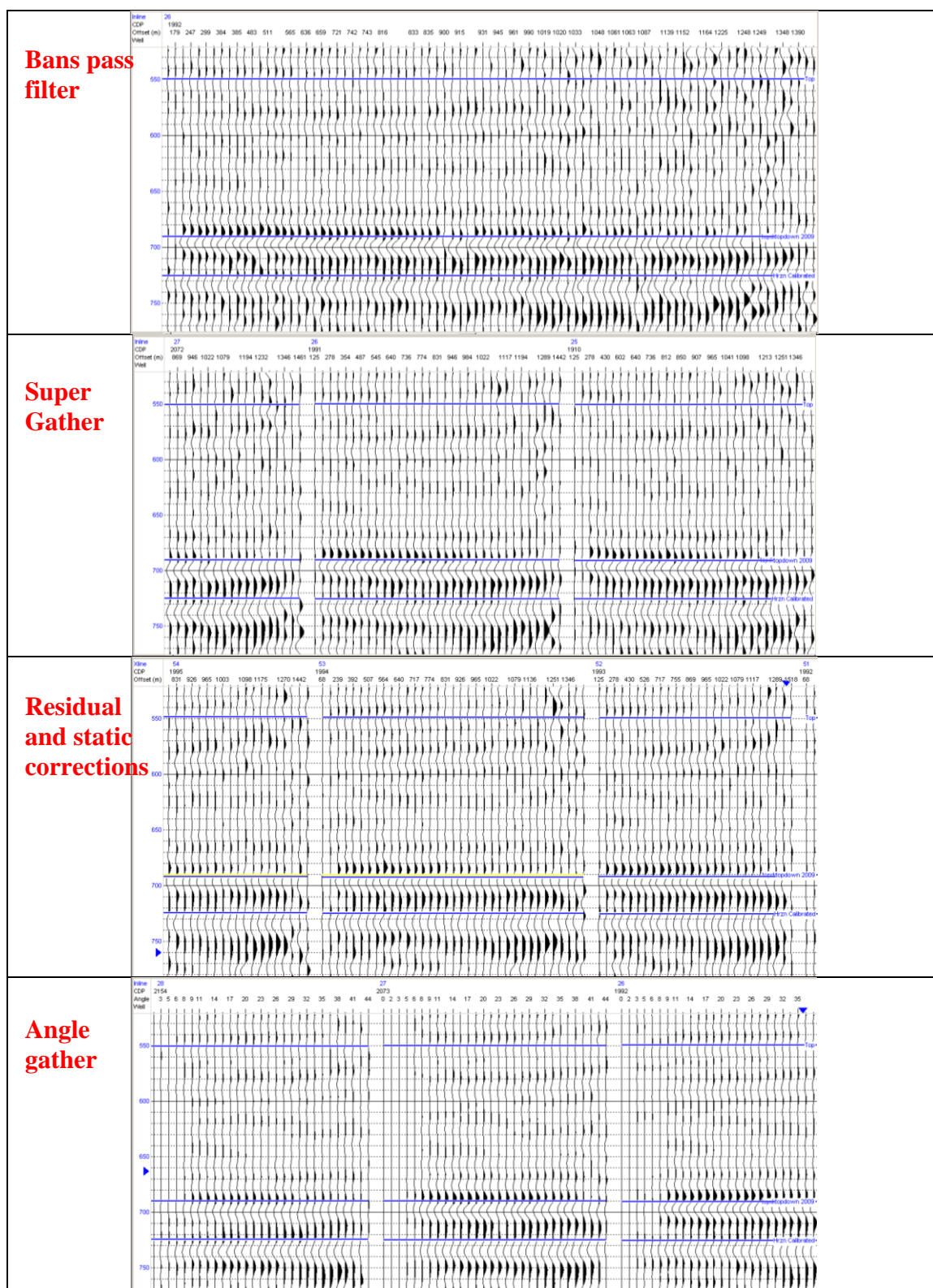


Figure 5.13, Processing workflow before pre-stack inversion.

which is a process similar to the stacking, but only stacks few (3 in this case) shot gathers together in order to improve S/N. Residual static correction in the next step, ensures the maximum continuity of reflectors. Finally, shot gathers will be reordered in the angle gather format, which was the software requirement for proceeding to inversion.

I conducted the pre-stack inversion only on the base survey to be able to use the computed Vp and Vs for further calibration. The results of the inversion are delineated on the map views in figure 5.14.

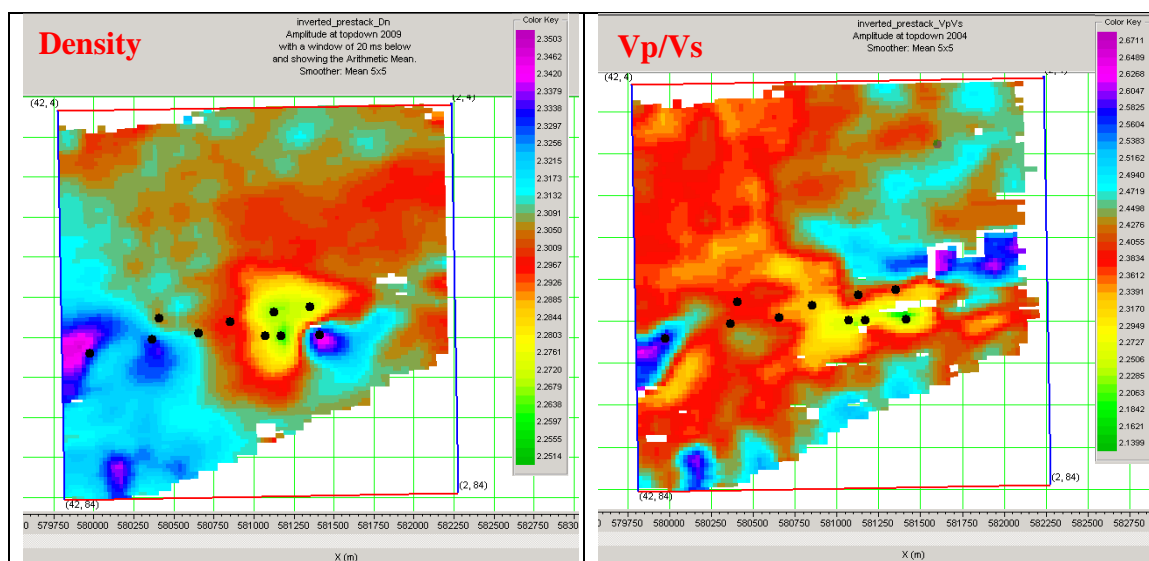


Figure 5.14, Pre-stack inversion results on the base seismic survey (2004). The map shows arithmetic mean in window of 20 millisecond below the reservoir top.

5.4 Reservoir modelling

The objective in reservoir modelling is to create a cellular model grid that firstly represents the reservoir structure and secondly contains the reservoir properties (permeability, porosity, reservoir net to gross ratio). The reservoir grid then can serve different purposes including volumetric calculations and reservoir simulation. In the current case study, the

grid model is built to run the reservoir simulation. Figure 5.15, summarizes the workflow for building the static geo-model, including its grid and the containing properties.

5.4.1 Structural modelling

In the workflow shown in figure 5.15, steps 3 to 6 are known as *structural* modelling which is the process where the faults, geometry, pillars and layers of the model are built. We discretize the model into grid blocks, where faults and reservoir boundaries serve as walls and pillars of the model. The main data, in which structural model is grounded on are well tops, surfaces and faults. I followed some considerations in gridding as follows:

- The boundary of the grid should cover the areal extension of the reservoir.
- Major grid directions are parallel/perpendicular to the flow direction. The flow direction usually is along/perpendicular to the structure and faults (dip/Azimuth).
- Square grid shape is preferred.
- Areal grid size should not be less than dimensions of seismic bin.
- Vertical resolution of grids should be more than logging resolution which typically is one to two feet.
- We should avoid introducing unnecessary details and complications in grid model, which can bring instabilities in reservoir simulation.

5.4.2 Property modelling

The next step in geo-modelling is to fill the grid cells with the most probable rock type or property, based on the statistics of well log data. In this practice geostatistical methods become key, where the unknown values can be estimated from the real data using the existing spatial relationship in the data. Spatial relationship can be characterized using the *variogram*; a plot representing the spatial variability of the data.

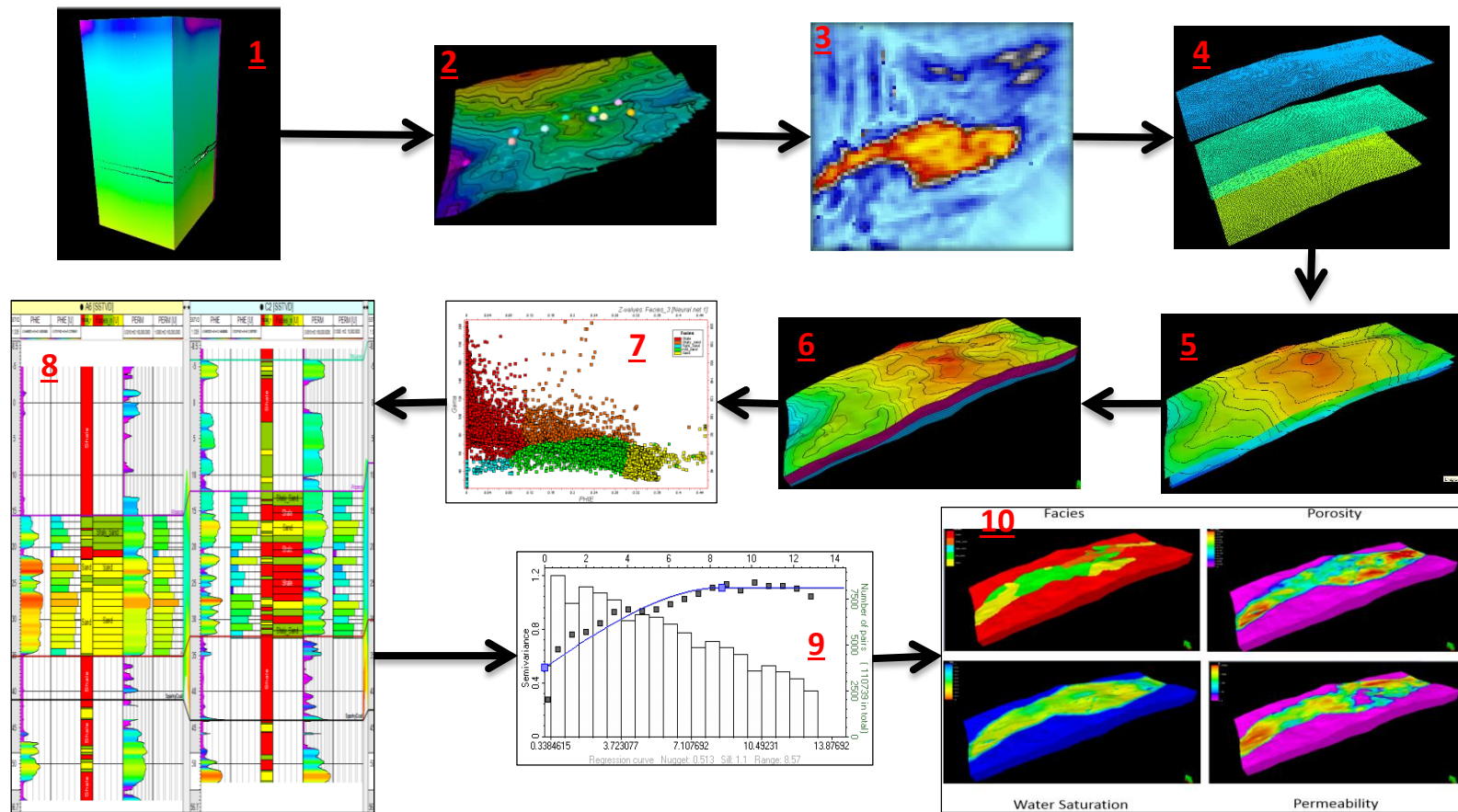


Figure 5.15, Stacking velocity cube, time horizons and well tops were used to create velocity model (1). Well tops and depth converted time horizon in depth domain (2). Defining reservoir boundary using sweetness attribute (3). Building grid skeleton (4). Defining model horizons (5). Adding vertical layers to the model (6). Rock type definition based on gamma ray and porosity values (7). Scaling up the logs into the grid cells (8). Variogram analysis (9). Cokriging rock types, porosity, permeability and saturation into the grid cells (10).

The variogram is useful when a spatial relationship exists between two close points. It assumes a stationarity in data, which means the local and global means are the same. Once the spatial relationship between available data is found and represented by a variogram, the next step is to utilize the variogram to estimate the values at unsampled locations. The estimation technique that deterministically estimates the unknown values using spatial relation between known values is called *kriging*. One can also take advantage of secondary data to estimate principal data. This technique is called *Cokriging*. The examples are estimating porosity using seismic acoustic impedances, based on the correlation between acoustic impedance and porosity at sampled locations. The other example is estimating permeability property using porosity, where permeability measurements can have correlation with porosity in the cored samples.

In order to establish a cokriging scheme, primary and secondary variables should have strong linear correlations. However, in practice cokriging is very tedious and could be difficult to achieve. It is necessary to characterize three variograms; principal (e.g. porosity), secondary (e.g. acoustic impedance) and their cross-variogram which makes this technique literally impractical. *Collocated cokriging* on the other hand, is a popular technique for integrating secondary data in the estimation of the principal variable. Unlike cokriging, it doesn't use the cross-variogram, which makes it more appealing. Instead, the secondary data is required to be available in every unsampled location, where one needs to estimate the values of principal unknown property. Seismic data, typically has such a characteristic to be employed as the secondary data.

Statistical simulation techniques are methods that apply kriging to simulate (not estimate) properties at unsampled locations. These methods reproduce the histograms of

the input data, and are appropriate for uncertainty assessments, since they introduce randomness in the modelling. In such techniques, the unsampled grid cells are visited sequentially in random order and their values are estimated based on kriging. The estimated grid cells, then are treated as sampled data and will be employed in the simulation of the next unsampled grid cells. Since the visiting path is randomly selected, it is possible to come up with many different realizations, which are equally probable and hence acceptable. In general, all the sequential simulation methods have the following steps in common:

1. Transforming data to normal score distribution
2. Variogram analysis
3. Random path (the order of visiting cells with unknown values) selection of the grid cells
4. Kriging
5. Back transform.

Disregarding 3rd and 5th steps, will turn the simulation to kriging estimation. Readers can refer to Kelkar and Perez (2002) for details about reservoir geostatistics.

5.4.3 Geo-modelling in the case study

In the current case study, once the inversion part of the reservoir was completed I managed to build the reservoir model. This stage of the project includes several major steps, with the ultimate goal of building the structural grid and populating it with the most likely properties. The steps are summarized in the order that were carried out. Figure 5.15, also displays the accomplished workflow:

1. Creating the velocity model.

2. Converting the seismic-based data to depth. Different QC steps are involved here, including residual depth errors and validating obtained interval velocity surfaces.

3. Defining reservoir boundary, based on different seismic and time lapse attributes.

4. Defining horizontal grid cells, which is 10m*10m.

5. Building the horizons of the geo-model using the depth converted surfaces.

6. Adding layers (vertical grids of size of 1m) to the model.

7. Defining facies properties using the porosity vs. gamma plots. Five classes of facies were defined in this study, based on the cut-off values of porosity log and gamma log. The importance of facies is to distinguish different rock types and represent their spatial relations with a distinctive variogram. It also allows to model reservoir heterogeneity and geological connectivity of different rock types.

8. Upscaling all required logs (Facies, permeability, porosity). The goal is to assign an appropriate property value to the grid cells penetrated by the wells using the well log values. This step is required to move from log scale (~1-2 feet) to the grid scale (1 m).

9. Data analysis and variogram modelling for discrete and continuous data. This step is the most tedious part of the modelling. Different parameters of the variogram should be defined for each rock type. In addition, one needs vertical, major horizontal and minor horizontal variograms to be able to reasonably estimate the data in a spatial geometry. This step is the key in all the geo-statistical modelling. Determination of variogram parameters is critical to observe a spatial relation. If there is no spatial relation, no matter what parameters are selected, no spatial relation will be seen. However poor selection of these parameters can mask the existing relation. As long as the selection of the parameters gives

a clear variogram structure, those parameters are good enough. I followed the following considerations in defining variogram structure:

- Starting with isotropic variogram. This variogram picks the data points in all the directions, hence is more stable than any anisotropic variogram. Most of the time some sort of spatial relation should be reflected in the isotropic variogram. If not, it is difficult to imagine that anisotropic variogram shows spatial structure, with fewer data points.

- Using the isotropic variogram to establish the lag interval and lag tolerance. The smallest possible tolerance at which an interpretable structure can be observed should be used to estimate the variogram. This is because some irrelevant data point might obscure the isotropic feature.

- Finding the maximum and minimum direction of continuity of the data. This can be investigated by finding the range of variograms at different directions. The maximum and minimum continuity will be in line with highest and lowest range, respectively. Variogram map of the range values would be also beneficial to examine this. For modelling purposes, minimum and maximum continuities are always assumed to be perpendicular.

- The variogram is very sensitive to the outliers. If pairs have an abnormally large difference, it impacts the variogram calculation and results in instabilities. One can either ignore these problematic pairs (identifying them by cross plot of the pairs), or mitigate their influence by incorporating larger number of pairs into variogram calculations. This can be achieved by increasing lag and/or angle tolerance.

10. Populating properties in the grid, using collocated co-kriging. The accuracy of this step depends on all the previous steps, and especially the quality of the variograms.

There is an inherent uncertainty associated in all steps. The main ones are velocity model, and property modelling. It worth mentioning that the model that I ended up with is just a realization among many realizations that are equally likely and consequently correct.

5.5 Reservoir simulation

The purpose of the geo-modelling in previous section is to feed the grid model to a reservoir simulator and to predict its behaviour (section 2.1).

Reservoir simulation is grounded on the basis of three fundamental laws, namely conservation of mass, Darcy's equation and the equation of state. The first two principals will lead to diffusion equation. Enforcing a certain initial and boundary condition to the grid model, will result in a certain solution (behavior), which is called reservoir simulation. The goal is to simulate the reservoir behaviour as similar as possible to the production history and pressure data. This process is known as history matching.

The history matching process is a difficult and tedious task because of many uncertain parameters. It might be argued that since the diffusion equation is a parabolic equation and its solution is smooth, it should be less complicated than hyperbolic equations like the wave equation. As the matter of fact, diffusion equation solved in reservoir simulators appeared to be much complex and has a fundamental distinction comparing to the wave equation. The difference is that the state of the medium of study is changing at every time step. The key variations are pressure and temperature which will result in a series of changes including but not limited to the compressibility of rock/fluid, absolute permeability, viscosity, formation volume factor, density, and saturation. Saturation changes will result in capillary pressure and relative permeability changes. In addition we are dealing with three set of equations for the gas, oil and water phases. Considering the nonlinear nature of

many of these coupled changes can explain many of the instabilities and failures in the simulation results.

History matching is a forward modelling solution for an inverse problem. In other words the approach is to modify key uncertain variables in the rock and fluid model and try to get a reasonable match between the predicted results and recorded data. The mismatch is very dependent on the input data, so a missing or invalid data, results in inaccurate and uncertain results.

The data which was available for the reservoir simulation in current study was static data including well tops, well logs and seismic surveys, which has been employed to build the grid model.

The available dynamic data for this field was oil, water and gas rates. The major missing part of the data was the flow and rock properties which are typically obtained from PVT and core analysis, respectively. In addition the pressure data had not been recorded during the production. I applied some typical heavy oil properties for the fluid. Also some characteristic relative permeability curves were selected for the reservoir rocks. Figure 5.16, illustrates the reservoir simulation results based on the selected rock and fluid properties. Note that even if we predicted the cumulative production accurately, this simulation has great uncertainty due to the missing data. It worth mentioning that one can change the unknown parameters by trial and error to find another good match, but it is arguably equally uncertain and biased. For the sake of this study I will go ahead with the current simulation results, since I don't care about the prediction reliability, and I just need to convert the results to acoustic impedance with a reasonable degree of uncertainty.

Here the value of seismic assisted history matching can be appreciated, since it will put the current simulation results to the test, by comparing seismic data with the synthetic seismic created from the static properties and dynamic simulation results.

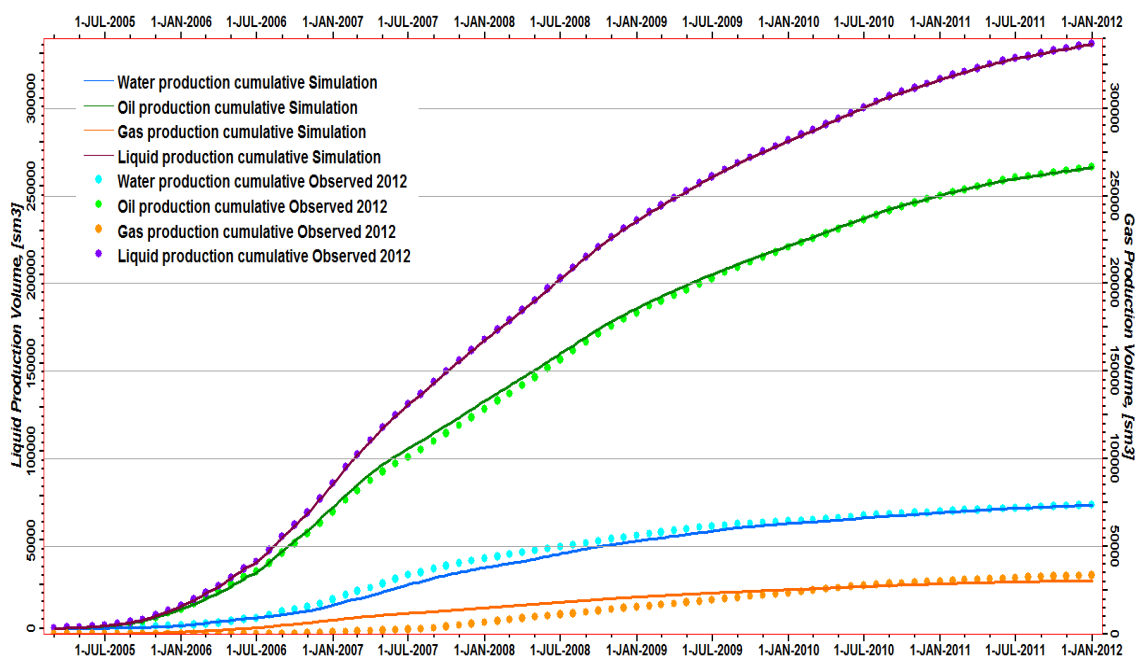


Figure 5.16, Simulation results in field level. Principle matching target is liquid production rate and the minimum bottom hole pressure at the wells is 2 bar. The wells are perforated in the entire reservoir interval. Note that the good match, other than reasonable static grid, fluid and rock properties is due to the fact that simulator is free to change the well head pressure. In case that pressure data is available this parameter is constrained and history matching process is more tedious.

5.6 Sim2Seis software development

Here I came to the point that it was required to develop the Sim2Seis idea through the programming. The objective behind developing this program was to generate synthetic seismic attributes, at any production stage using reservoir properties and simulation results. Simulation results provide us with wide range of dynamic information, such as flow rate,

pressure, temperature and saturation changes in the reservoir. Having the ability to convert simulation result to acoustic impedance can be translated to being capable of creating synthetic acoustic properties in the course of reservoir production. Figure 5.17, illustrates such a functionality. Since this process is not available in the deployed commercial software, I developed it as a plug-in to be attached to PETREL. This plan was accomplished using Ocean developer's kit which is Schlumberger's development platform. The *Sim2Seis* software was developed in C# language in Visual studio and as a plug-in for PETREL. The main purpose of this plug-in was to convert simulation results to acoustic impedance. This software was called Sim2Seis to describe such functionality. The goals that I aimed to achieve were:

- Reducing the uncertainty of the reservoir simulation results by constraining them with seismic acoustic impedance,
- Validation of the flow simulation results using seismic acoustic impedance,
- Feasibility studies to plan future 4D surveys,
- Evaluate the optimum time-lapse intervals between successive surveys,
- Generating time lapse logs.

5.6.1 Sim2Seis architecture for conventional fluids

The conventional fluid part of this plug-in, is based on the Gassmann's equation. Since C# is an object oriented programming language, the plug-in treats every reservoir grid cell as an object, comprised from three other objects (Figure 5.18). The grid object is the saturated bulk moduli object which is a function of matrix elastic moduli, fluid elastic moduli and dry framework elastic moduli, and can be computed using Gassmann's

equation. Fluid elastic object itself, has three properties, bulk modulus, shear modulus and density that can be estimated based on Batzel-Wang's correlations (Batzle and Wang, 1992). This object can be calculated from different properties of gas, water and oil, shown in Figure 5.19.

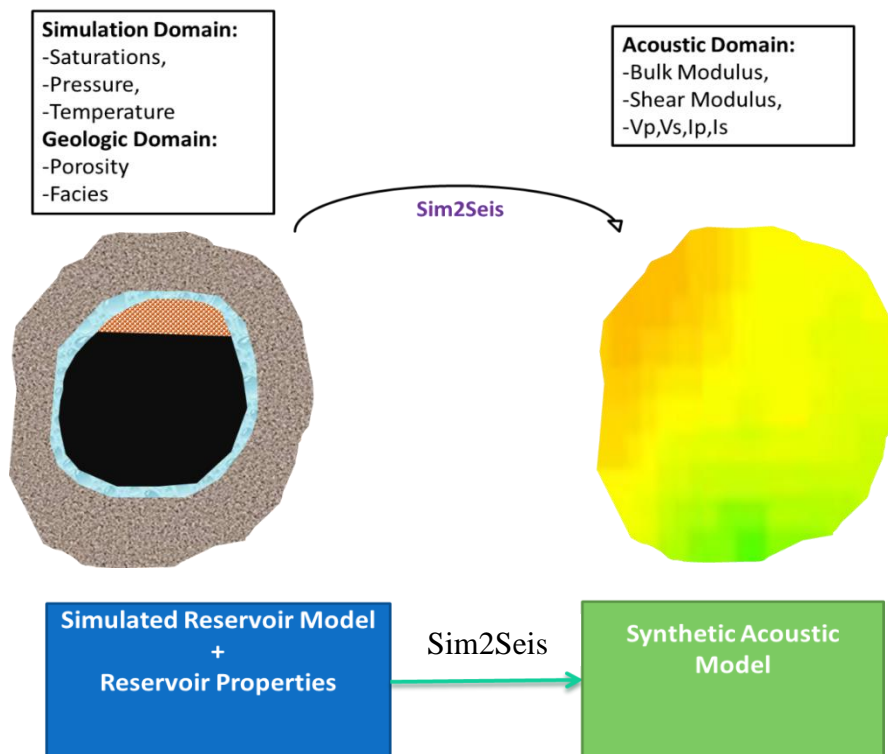


Figure 5.17, Sim2Seis developed to convert simulation results to acoustic impedance.

Calculations for the fluid elastic object are addressed in the input tab of this plug-in. The designed interface is shown in figure 5.20. Once the fluids' properties are entered, the lower table will be updated accordingly with the computed elastic moduli right away. Most of the time we have variable geological properties rather than a single number. For example we usually have saturation, porosity, temperature etc., as grids. I developed such a functionality in Sim2Seis to enable the calculations when the inputs are grids (Figure

15.21). Note that if any of the information is in grid format then the fluid elastic modulus will not be calculated, in the lower table.

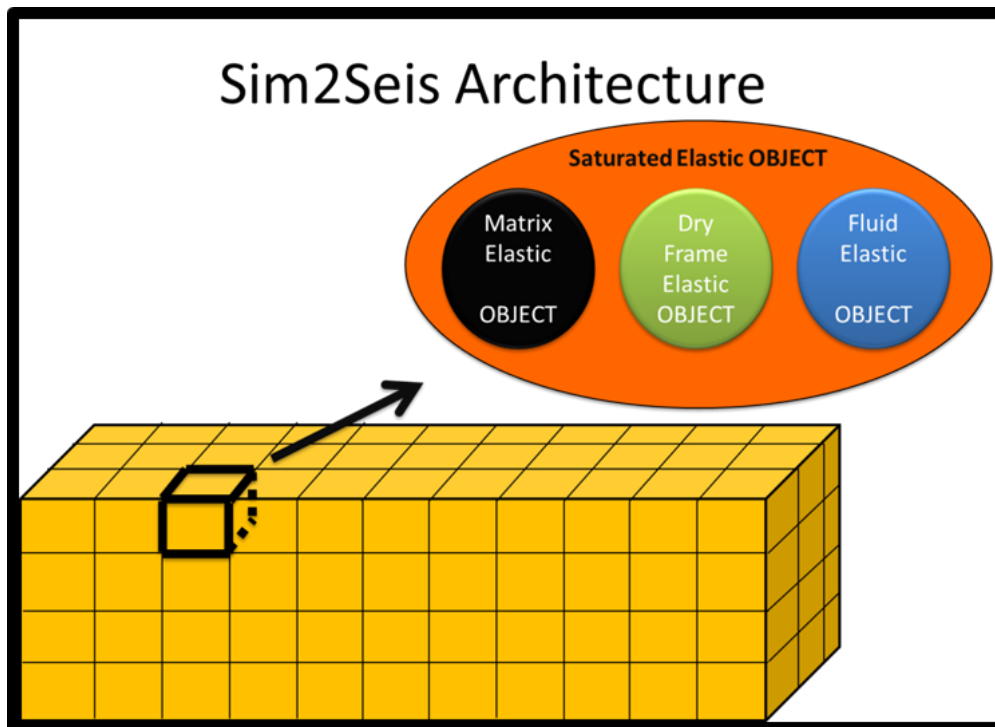


Figure 5.18, Saturated elastic object in every grid cell is a function of matrix, dry frame and fluid elastic object.

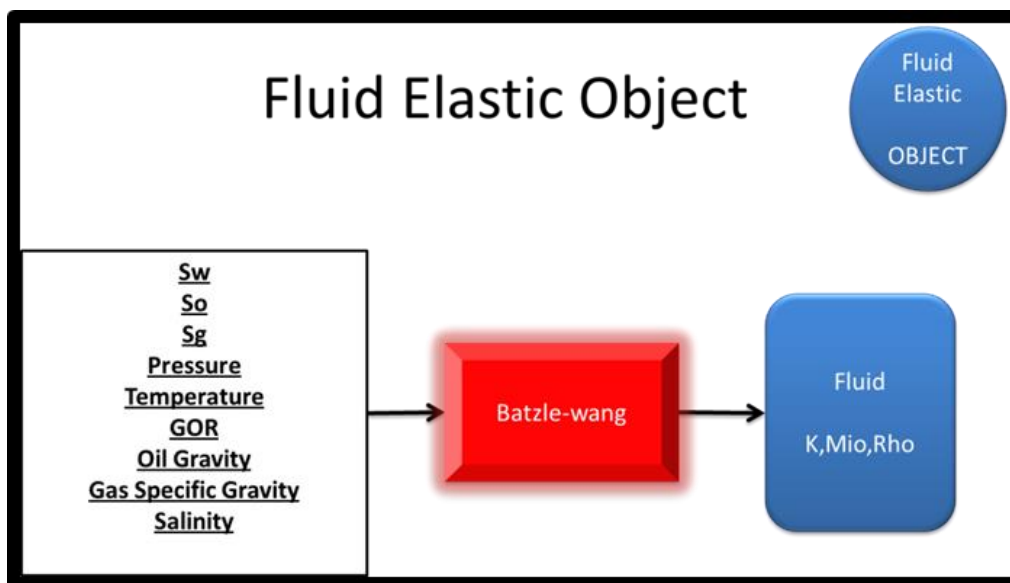


Figure 5.19, Fluid elastic moduli object.

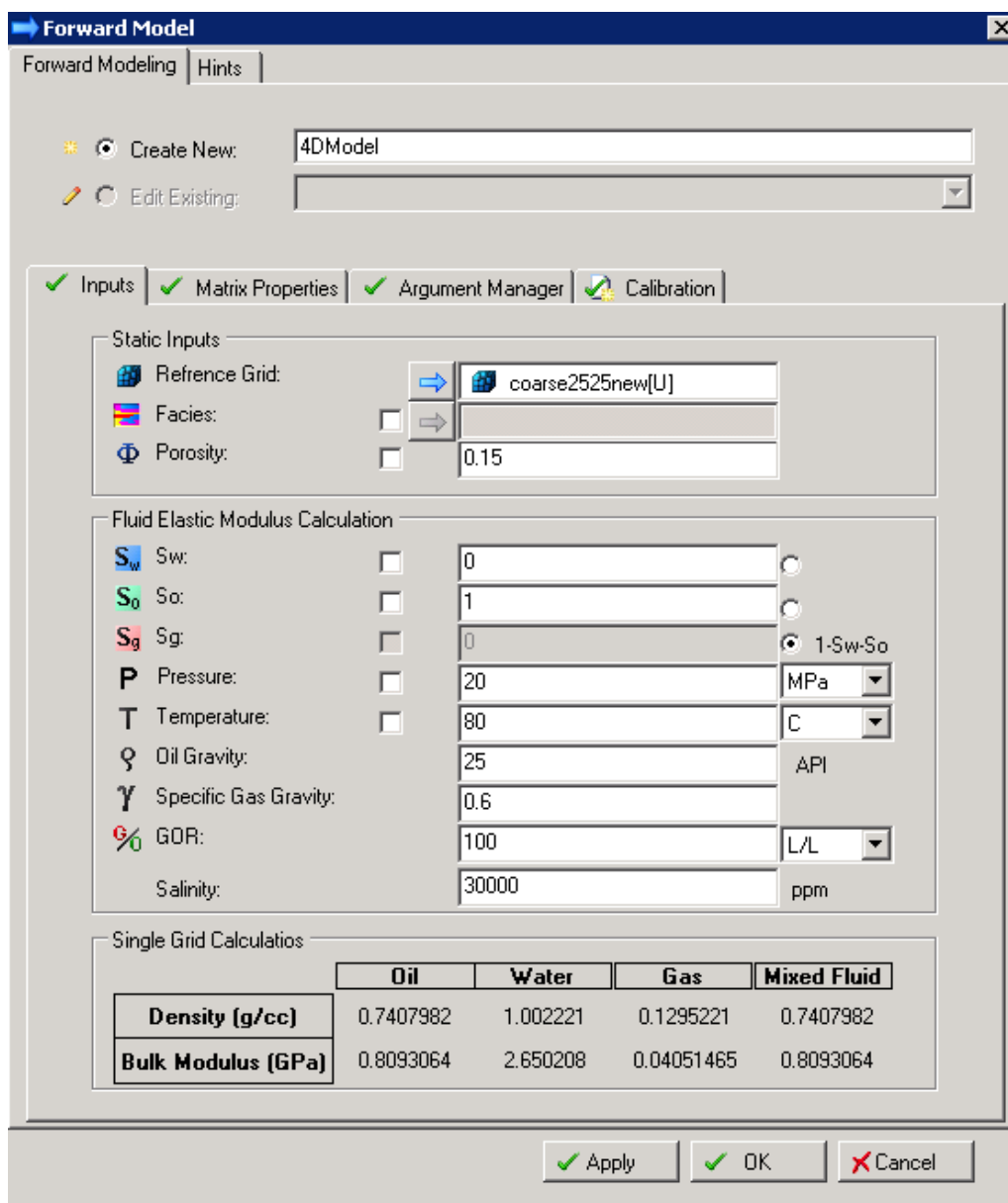


Figure 5.20, Sim2Seis inputs tab's interface; fluid elastic object.

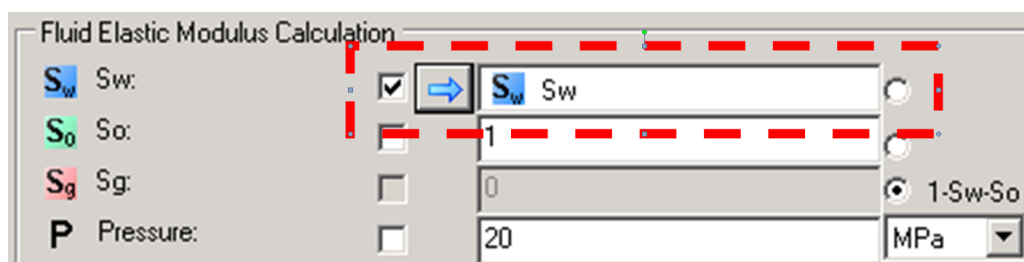


Figure 5.21, It is possible to input grid as the input data.

The second required object for saturated elastic modulus computations, is the matrix elastic modulus. For this object, one needs to have the constituent minerals of the matrix and their fractions. Hence we can come up with the effective elastic moduli using different mixing schemes (Figure 5.22).

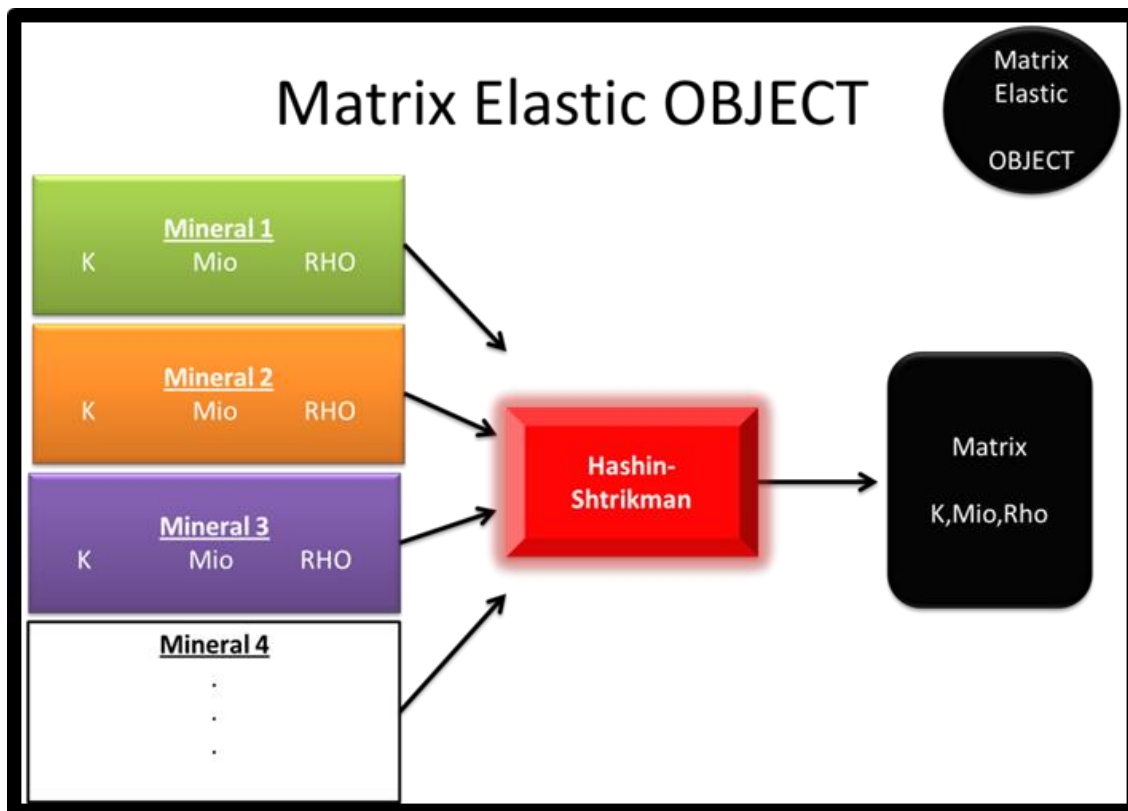


Figure 5.22, Matrix elastic moduli object.

Matrix property tab is designated to handle the entry of the required input minerals for the calculation of matrix elastic modulus (Figure 5.23). A library is provided internally as a drop down menu in the second column that allows the user to select any of the several minerals in the matrix. Also an option for user defined mineral is available to enter the required properties manually, in cases that the default library properties of a mineral is not

representative. Once the fractions are set for the constituent minerals (they should add up to 1), the warning sign on the tab will turn into the green check sign, showing valid entries.

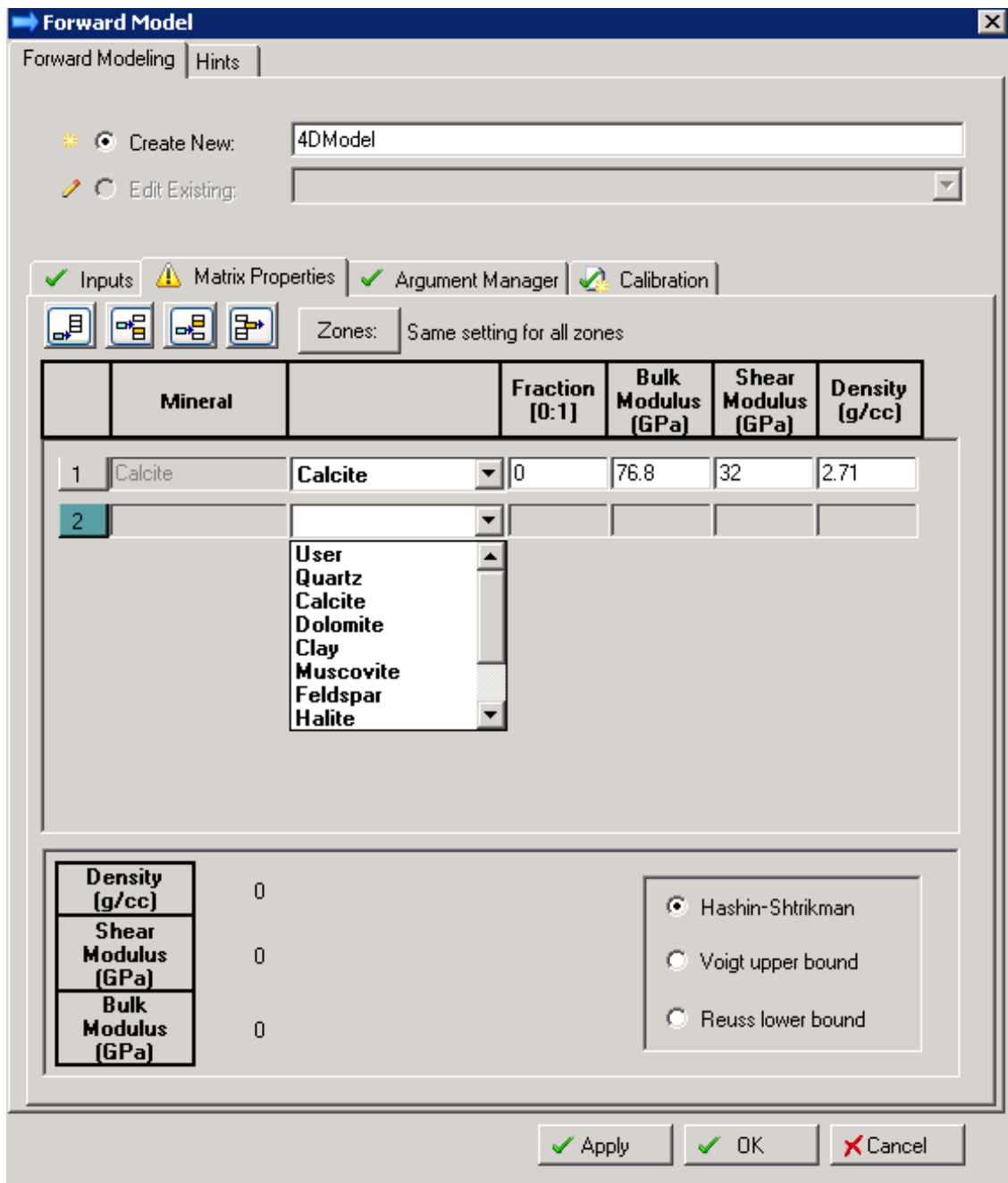


Figure 5.23, Calculations of the elastic moduli of the matrix; matrix elastic object.

At this point the calculated mixture of elastic moduli will be shown at the lower pane, based on the selected combination method.

Usually the matrix is assumed to be single type in the whole reservoir. However, since we would deploy the plug-in in the real case projects, multi-facies types should be considered. This option is available, only if the user enters the facies type as a discrete grid in the input tab (Figure 5.24). In such a case, by clicking on the Zones button in the Matrix Properties tab, we will have the option of setting a mineral mixture for every facies unit, separately (Figure 5.25). Also note that by importing the correct data, warning sign has turned into a check mark.

This option of multi-facies definition, proved to be very helpful in the current case study. It will be used to add the clay content for certain rock types, which in turn will reduce the acoustic impedance only for the regions in the reservoir comprising that that facies type.

Next object which is needed for the calculation of saturated modulus is the dry elastic modulus of the rock. This object is the most challenging one, and can be calculated from empirical correlations or can be calibrated based on the available data. Figure 5.26, shows the data types that are needed for calculations of this object.

The *calibration tab* of the Sim2Seis plug-in is intended to compute the dry framework elastic modulus. This tab has been shown in the Figure 5.27. The user has the options of using either empirical or calibration approaches for the estimation of elastic modulus.

If we choose to use the available inverted impedance data, the plug-in will back calculate dry elastic moduli from the provided saturated moduli. These computed dry framework moduli can be utilized to calculate the saturated modulus in the times, where neither dry nor saturated moduli, are available.

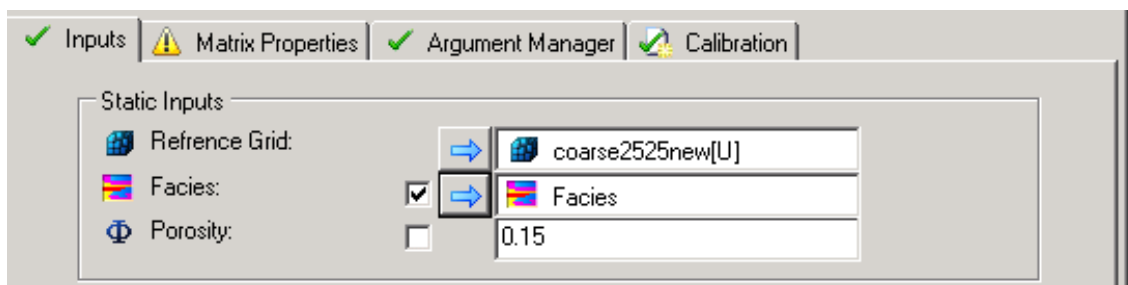


Figure 5.24, Discrete facie input, for using in matrix elastic calculations.

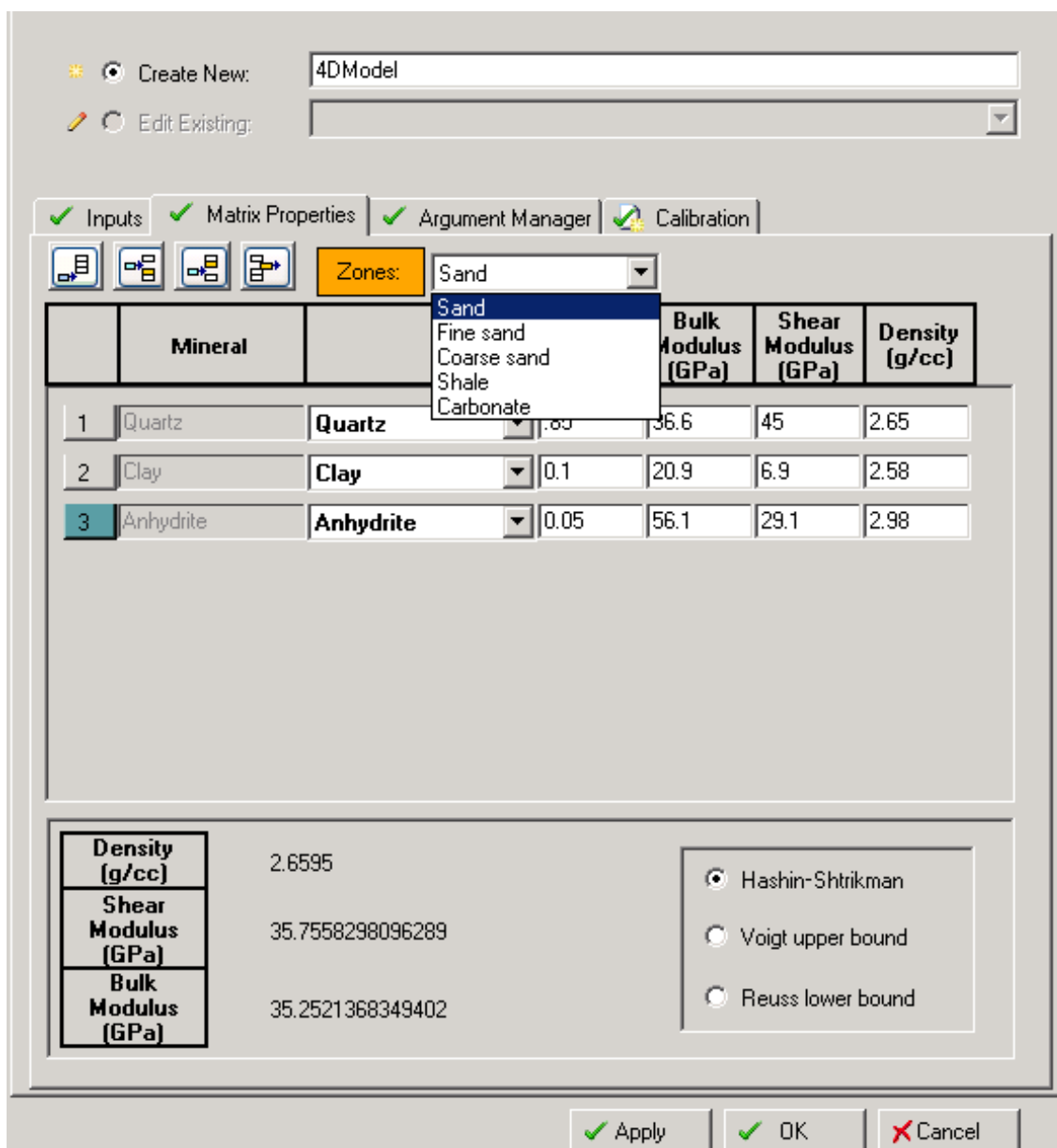


Figure 5.25, Calculations of the elastic moduli of the matrix for several facies units.

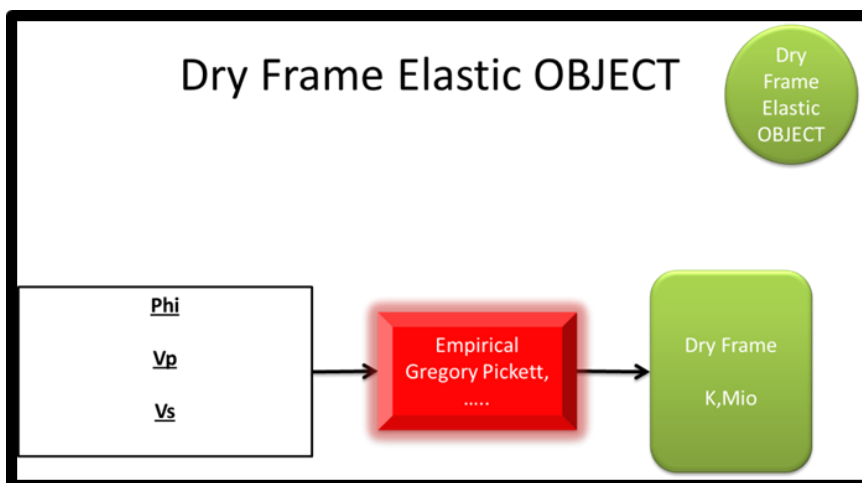


Figure 5.26, Dry frame work elastic moduli.

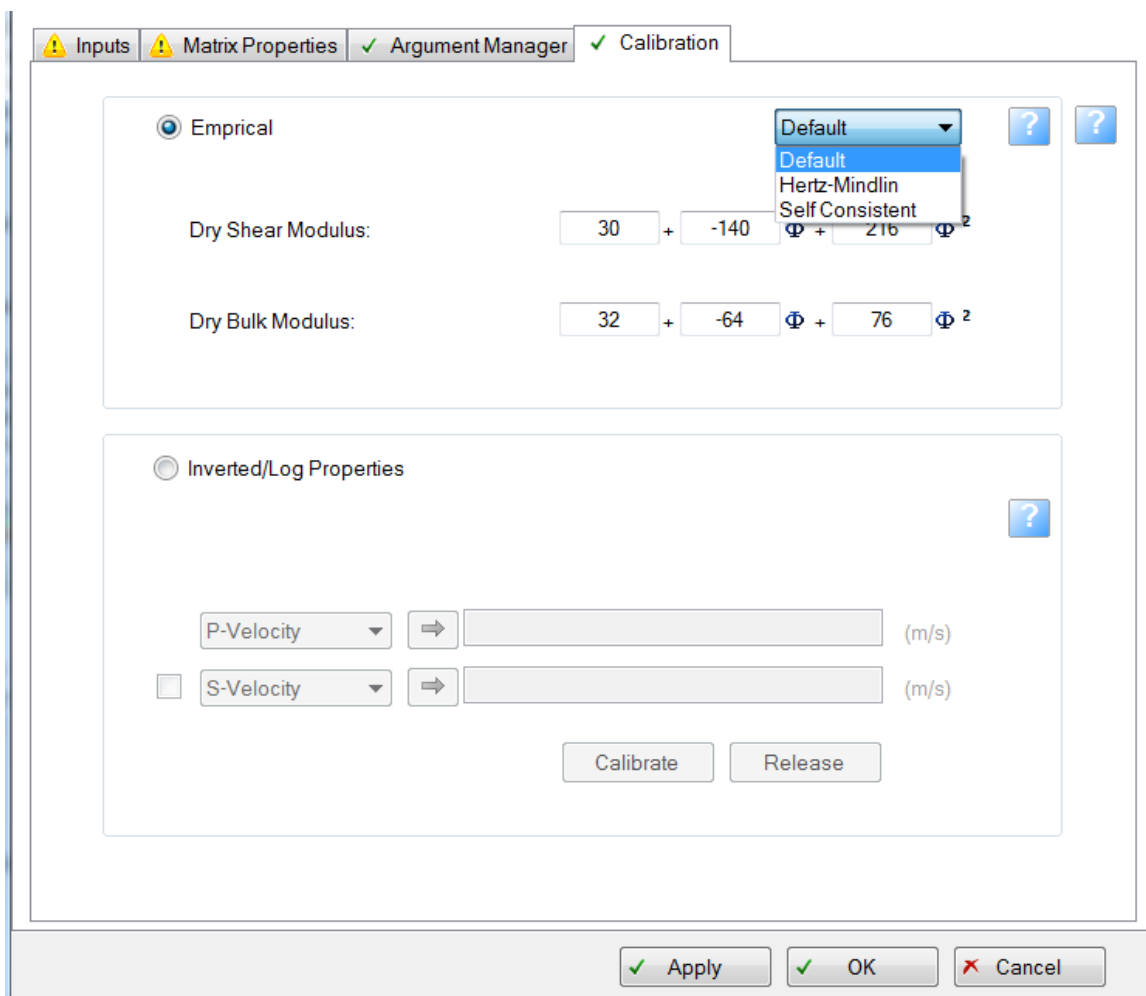


Figure 5.27, Calibration tab; dry frame elastic object.

Next tab, is the *Argument manager tab*. The purpose for this tab is to incorporate any data, from miscellaneous sources into the Sim2Seis computations. One can even make the software to read the dynamic saturation, pressure and temperature inputs, directly from simulation results at a certain time step. This feature will facilitate, the efficiency of calculations from simulation results towards seismic impedances. Another feature is to exempt plug-in from the calculations of intermediate arguments, and directly provide them to the plug-in. These intermediate overrides might be available from lab measurements or seismic data invasions. Also note that these parameters can be entered either as a grid property or as a constant number (Figure 2.28).

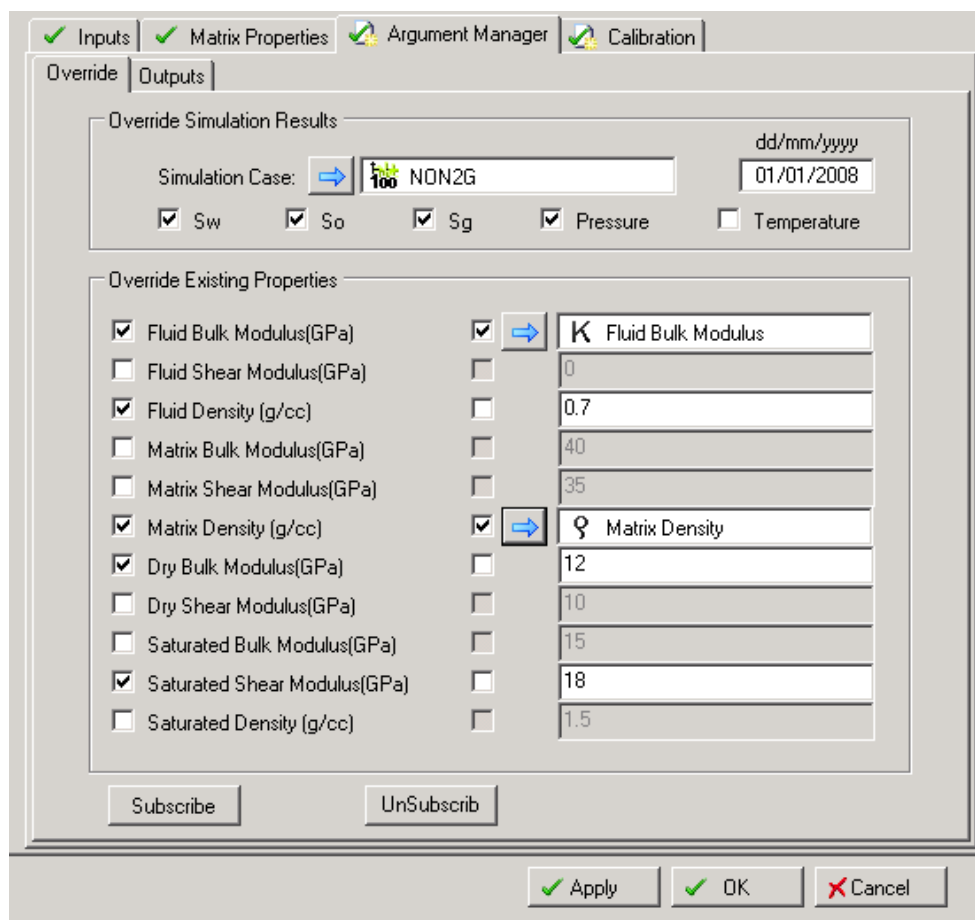


Figure 5.28, Overriding input parameters (simulation, or intermediate properties).

Requested output results also is going to be determined in the Outputs sub tab in the Argument Manager tab. The user has an option to create all the intermediate grids along with the main velocity and impedance grids. Figure 2.29, shows the range of outputs and sample property grids that can be created, in models pane.

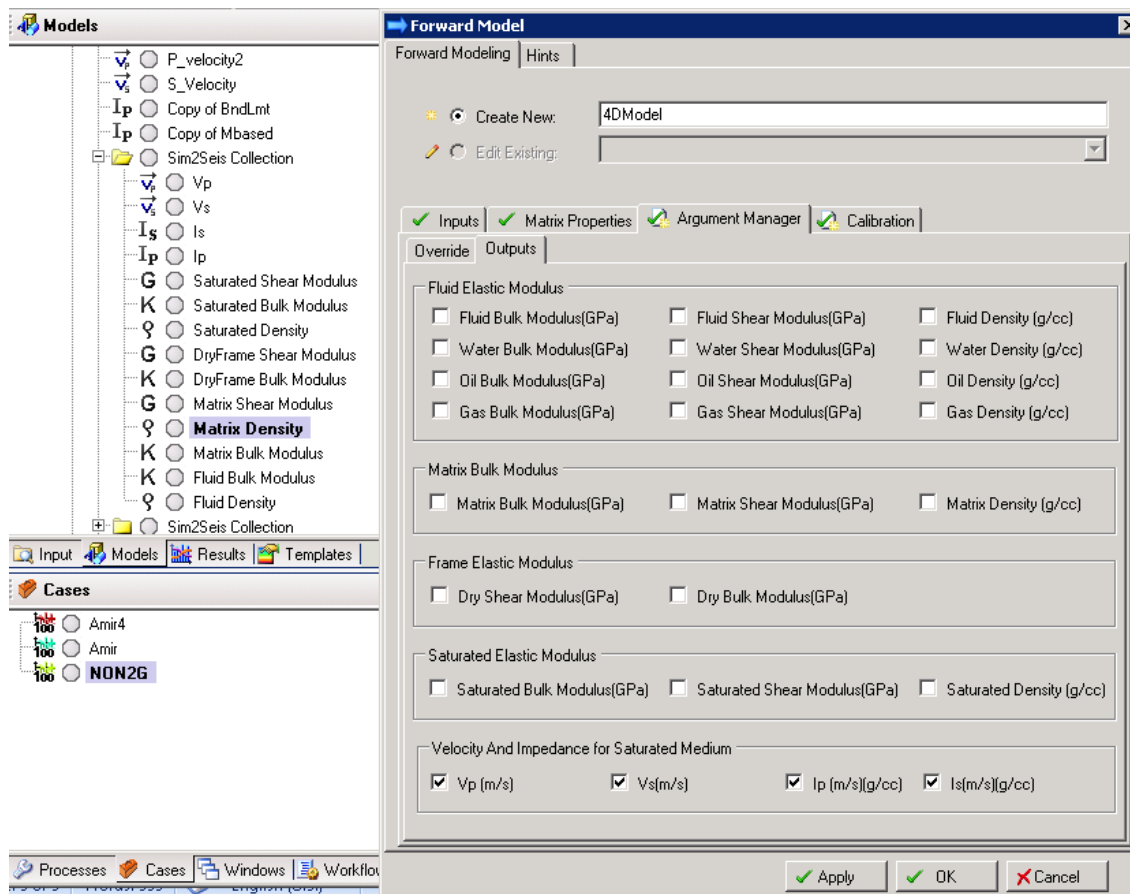


Figure 5.29, Different outputs that a user can select to be created in the models pane.

The most challenging part of the development of this plug-in, was to make it robust, solid and reliable. To achieve this purpose, I decided to add a debugging feature to Sim2Seis in order to generate a log file which would reflect the computation's flow. This feature not only is a debugging tool, but also will help the user to track down the

miscalculation sources and ensures that all imported data will be called correctly during the process. This approach is opposed to the case in which the software acts as a black box, with not much control on the reliability of the results. Figure 2.30, shows a sample section of this log file.

```

Log.txt - Notepad
File Edit Format View Help
+++++Summary of the Input Arguments
The Run is:      FULL RUN
*****InputTab
---Grid Name:   coarse2525new
---Facies Name: Null
---Porosity is Constant :      0.15
---SaturaionWater is Constant : 0
---SaturaionOil is Constant :   1
---SaturaionGas is Constant :   0
---Pressure is Constant :      20
---Temperature is Constant :   80
---Oil Gravity :      25
---Specific Gas Gravity :      0.6
---GOR :        100
---Salinity :   30000
*****MatrixTab
---Number of Facies Units, Used in The Modeling:      1
*****OverridesTab
---Simulation overrides are: 0
---Fluid overrides are: 0
---Matrix Overrides are: 0
---DryFrame Overrides are: 0
---Saturated overrides are: 0
*****CalibrationTab
---Calibration by P & S -info
P-Info is:      Impedance
Max P info is: 3532.038      and Min P info is:      2245.091
S-Info is:      Velocity
Max S info is: 1671.478      and Min S info is:      923.0625
---Calibrated KDryFrame Overrides are: 2
KDryCal
MioDryCal
*****Requested Outputs
---Number of outputs: 4
Vp
Vs
Is
Ip
+++++Fluid Elastic calculations
1.Constant Porosity is assigned
2.Constant Sw is assigned
3.Constant So is assigned
4.Constant Sg is assigned
5.Constant Pressure is assigned
6.Constant Temperature is assigned
7. INTERMEDIATE OVERRIDES: 0
8. Starting Fluid calculations....
  a.Computing Gas Constants
  b.Computing Oil Constants

```

Figure 5.30, the log file generated by Sim2Seis for QC purposes.

5.6.2 *Sim2Seis heavy oil version*

In the second version of Sim2Seis, I added the viscoelastic fluid modelling feature to the plug-in. This version gives the user an option to switch between conventional and heavy oil cases. If the latter is selected, then additional tab will be appeared for the purpose of viscoelastic fluid modelling.

The difficulty in such a development is that we deal with complex numbers as moduli of viscoelastic fluid. These numbers need complex algebra, accordingly. In terms of programming, C# is not capable of doing complex calculations directly, and it is needed to develop a *structure*, in which common math operations for complex numbers are defined. Figure 5.31 illustrates the created structure diagram of complex numbers and the associated methods for handling their mathematical operations.

Figure 5.32 shows the extra *Viscoelastic Calibration tab*, which will be appeared once the heavy oil option in the Sim2Seis is selected. Since this tab is for calibration, it is required to load the calibration data. For example let's say we need to load V_p measured data. For this purpose we need to select V_p from the drop down list. Now we have the options of either typing the data in the table or loading the data. By clicking on the load data button, and browsing the appropriate file, data will be displayed on the table and will be shown simultaneously on the corresponding graph. Figure 5.33 illustrates the sample imported data and its display.

For starting the calibration we need to import as much data as available, in a similar manner, i.e., the required data type should be selected from the drop down menu, followed by importing and verifying their quality on the corresponding plot section. Figure 5.34, illustrates an example of loading all the data for calibration tab.

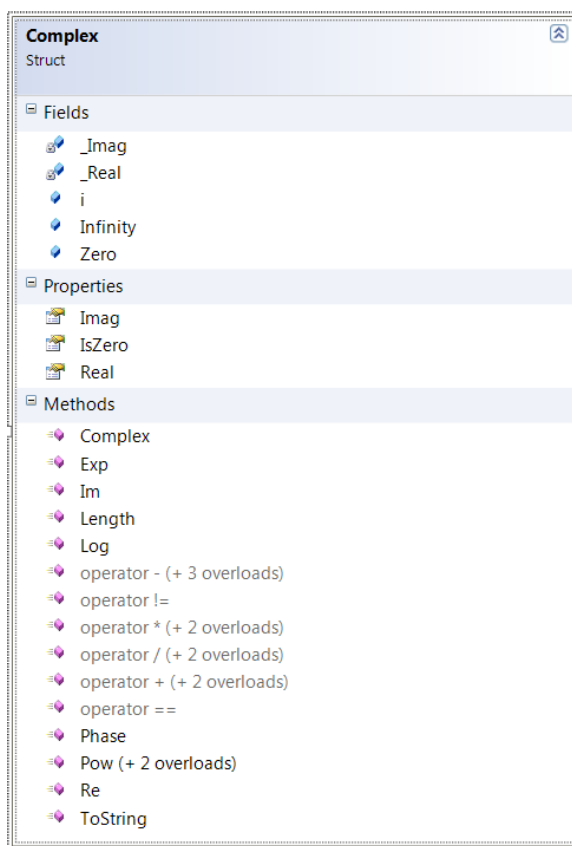


Figure 5.31, an structure designed for handling complex number algebra in C#.

Once the measured data is loaded, one can review and edit each data values. By selecting the appropriate option from the drop down menu and editing the data point, the plot display will be updated accordingly. Next step is to start matching the CPA and/or Hashin-Shtrikman models with available data. User has the option of either typing some value in each cell or import the already calculated values in Sim2Seis. The second option is only available for the parameters with a blue array right beside them. For example shear modulus of matrix or bulk modulus and densities of matrix and conventional fluid are already computed by Sim2Seis. So if one needs to employ them, it can be easily retrieved by clicking the blue arrow and the corresponding cells will be filled.

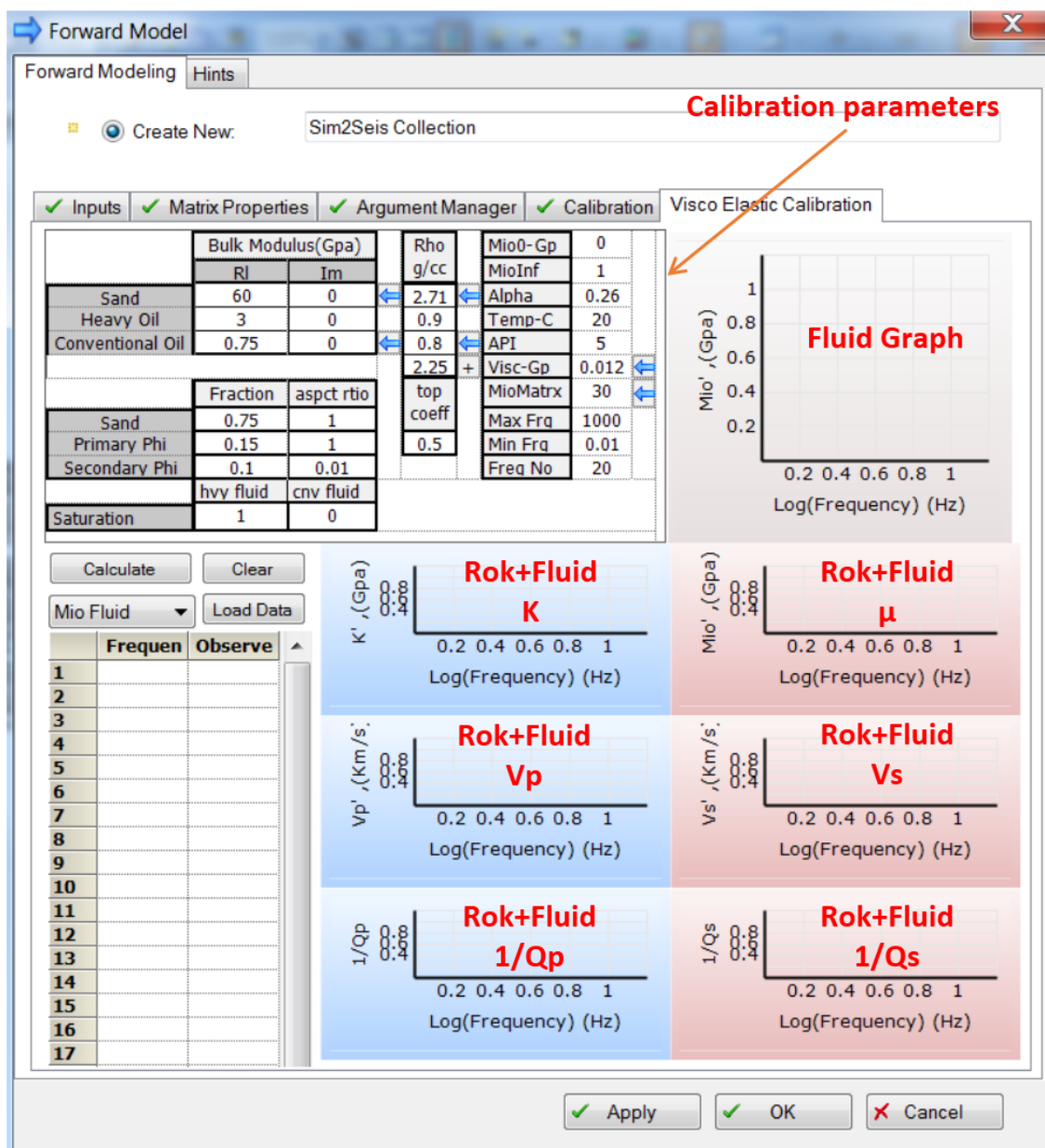


Figure 5.32, Viscoelastic Calibration tab.

Viscosity also can be estimated by Beggs-Robinson correlation (1995) by clicking the blue arrow, if it is not available for a certain temperature. And finally for calculating the total density clicking on “+” pushbutton will compute the value.

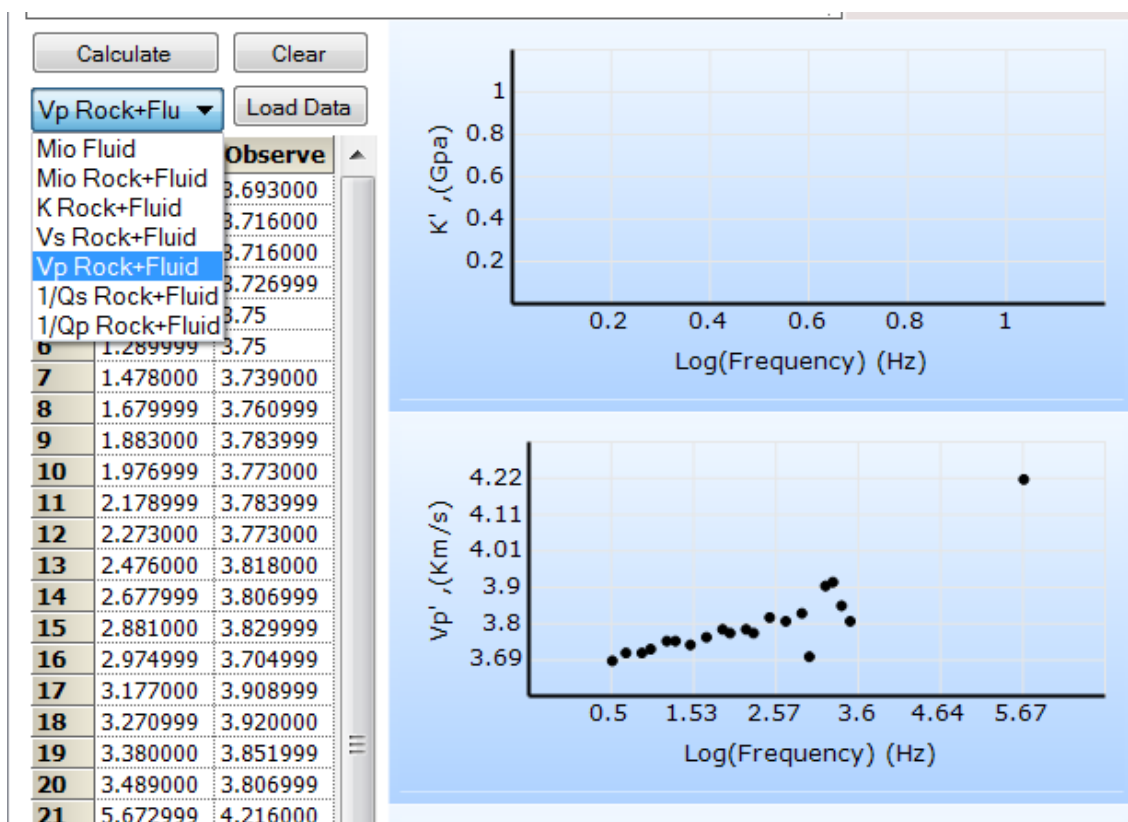


Figure 5.33, Loaded table will be automatically displayed on the corresponding plot section.

Once the parameters are set, one can click on the *calculate* button and all the corresponding plots will be updated on the graphs.

Figure 5.35 shows the final results. First graph which has a single curve, is the shear modulus estimation for the heavy oil, based on Cole-Cole correlation. Other graphs are the modelled elastic moduli with different methods (chapter three). The upper and lower Hashin-Shtrikman bounds are depicted by two purple curves. CPA method is shown in red and weighted average of Hashin-Shtrikman bounds are displayed in blue. User will be able to estimate the best matching parameters by tuning the input model variables. Once set,

these model parameters will be employed for the viscoelastic computations in the entire reservoir heavy oil saturated rock.

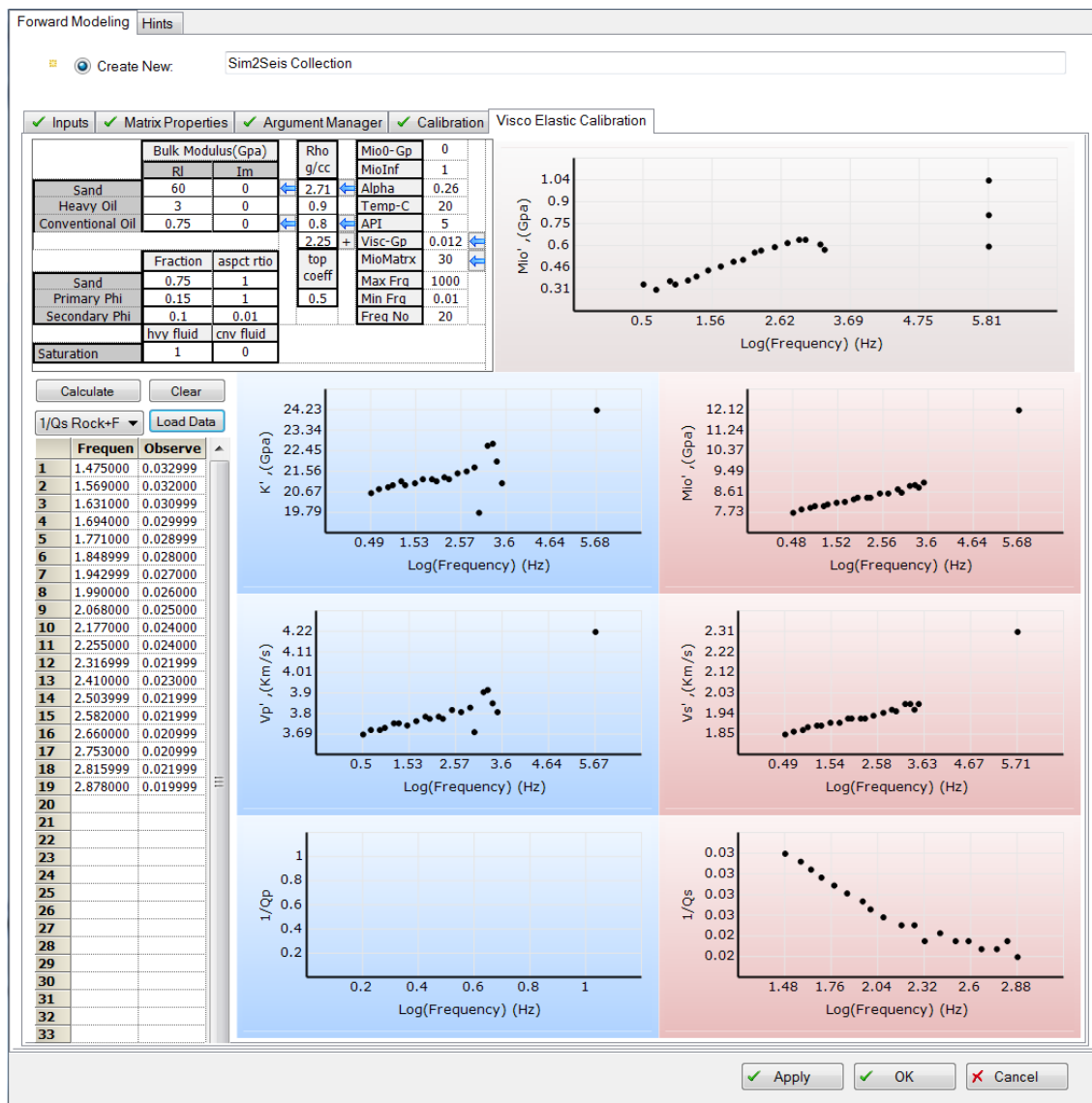


Figure 5.34, Loaded calibration data.

Unfortunately this kind of recorded lab data, is not commonly measured. In the current case study it was not possible to deploy this feature due to the lack of associated data measurements.

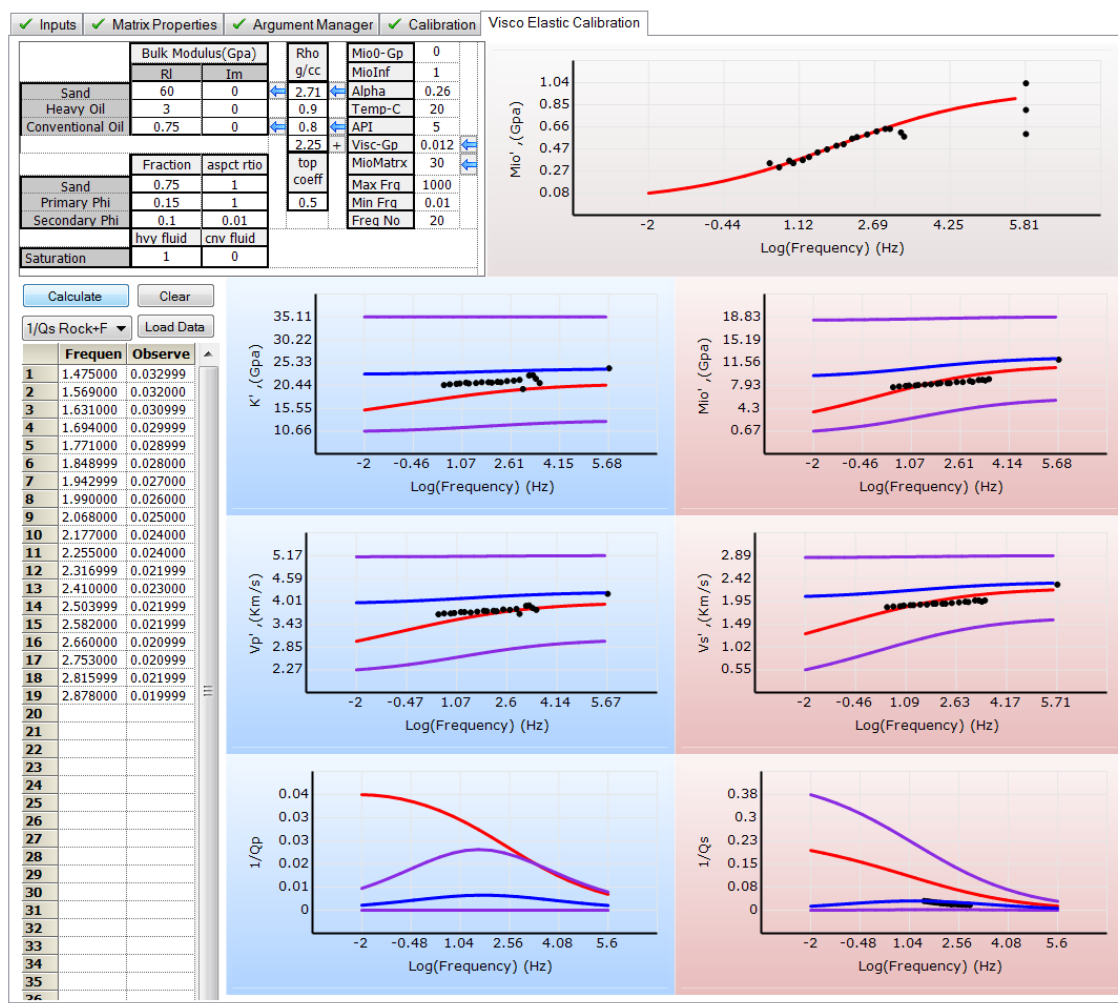


Figure 5.35, Modelled behaviour of the heavy oil.

5.7 Results and discussion

The final step and the main goal in the current case study is to feed the simulation results into the Sim2Seis plug-in in order to create synthetic elastic moduli and comparing it with the acoustic moduli computed from seismic inversion. Figure 5.36 shows the comparison between the modelled P-impedance, based on the simulation results (using Sim2Seis) and seismic inverted P-impedance for the monitor case (2009).

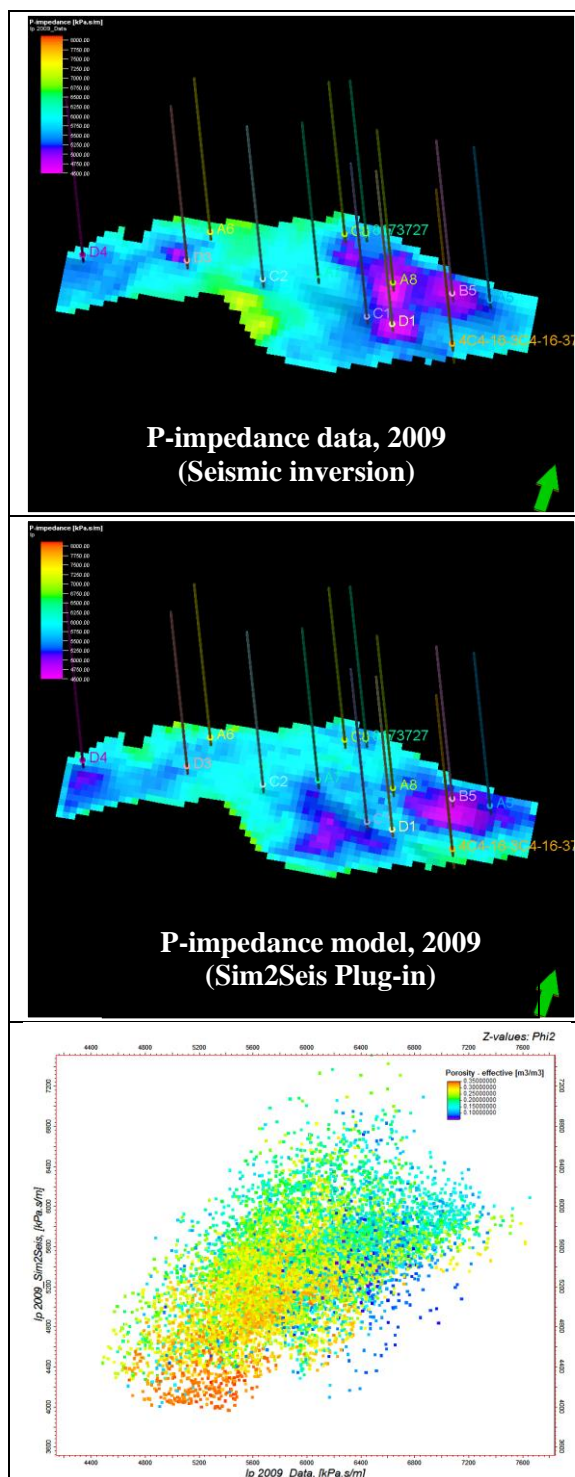


Figure 5.36, Comparison between the modelled (sim2seis) and real P-impedance (seismic inversion). The plot shows 0.55% correlation coefficient between data (x-axis) and model (y-axis). Colors show effective porosity.

This figure shows a reasonable agreement between the modelled and real P-impedance. According to the plot the correlation coefficient between these two is about 55%. The difference between the modelled and the inverted impedance data not only should not be surprising, but actually is appealing. This discrepancy is in fact a warning for the reservoir engineer and geo-modeller that even if the simulation scheme has ended up with perfect match (figure 5.16), there is a criterion (P-impedance) that is off by ~45%. So we must employ seismic assisted history matching strategy to obtain a reasonable match between modelled impedance and inverted seismic impedance, by tweaking modelling parameters.

Two major parameters that can influence the modelled results are grid properties (like porosity and permeability) and fluid properties. I opted to adjust the porosity, permeability and relative permeability curves, since there is no information available for fluid properties which means that it literally has infinite degree of freedom.

Figure 5.37, illustrates three major improvements that have been achieved in our seismic history matching case study. The property corrections include increasing permeability around the wells (5.37 a), cokriging porosity with monitor acoustic impedance (5.37 b) and dry frame modelling based on the different facies in every grid cells (5.37 c). Steps (a) and (b) were implemented on the basis that production in this reservoir is based on CHOPS technique in which the formation is going to be altered significantly. Also recall that property modelling is a stochastic approach, which means that the employed property is one among thousands of equally good (probable) realizations. In step c, I added clay content of the shale facies, in order to reduce P-impedance of certain rock type (grid cells). Figure 5.38, shows the enhanced correlation coefficient between modelled and inverted P-impedance, up to about 81%.

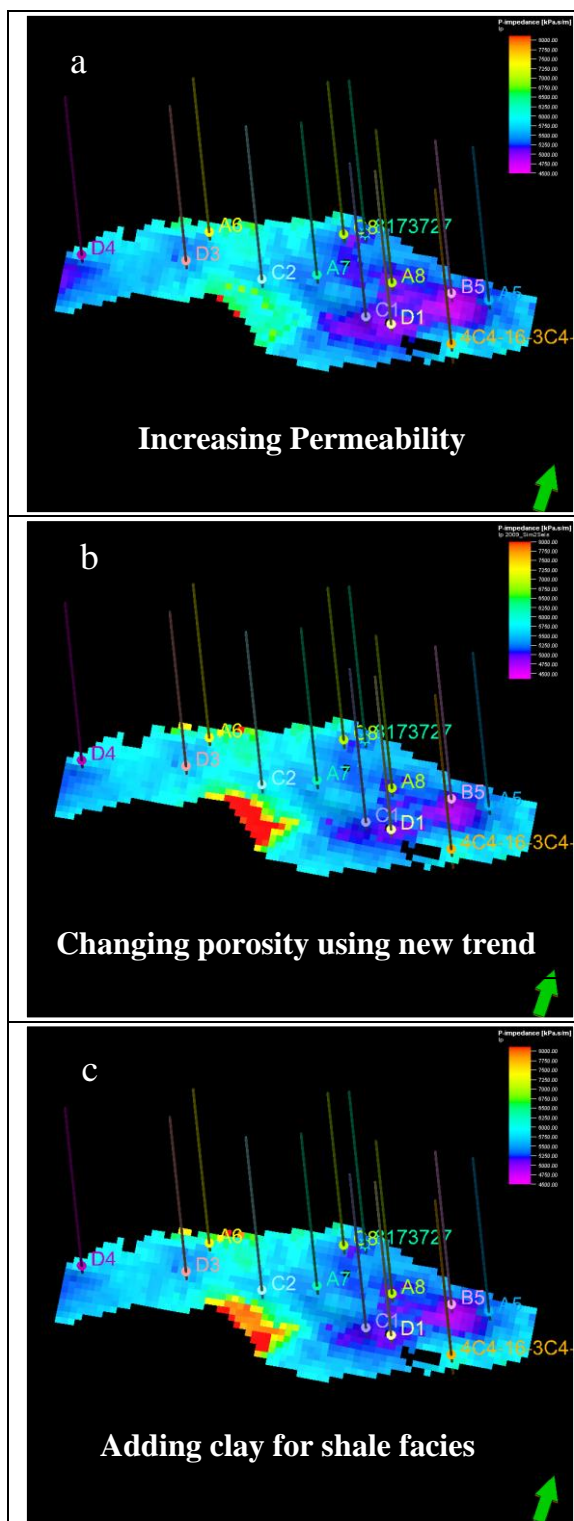


Figure 5.37, Property corrections include increasing permeability around the wells (a), co-kriging porosity with monitor acoustic impedance as secondary data (b) and dry frame modelling based on the different facies in every grid cells (c).

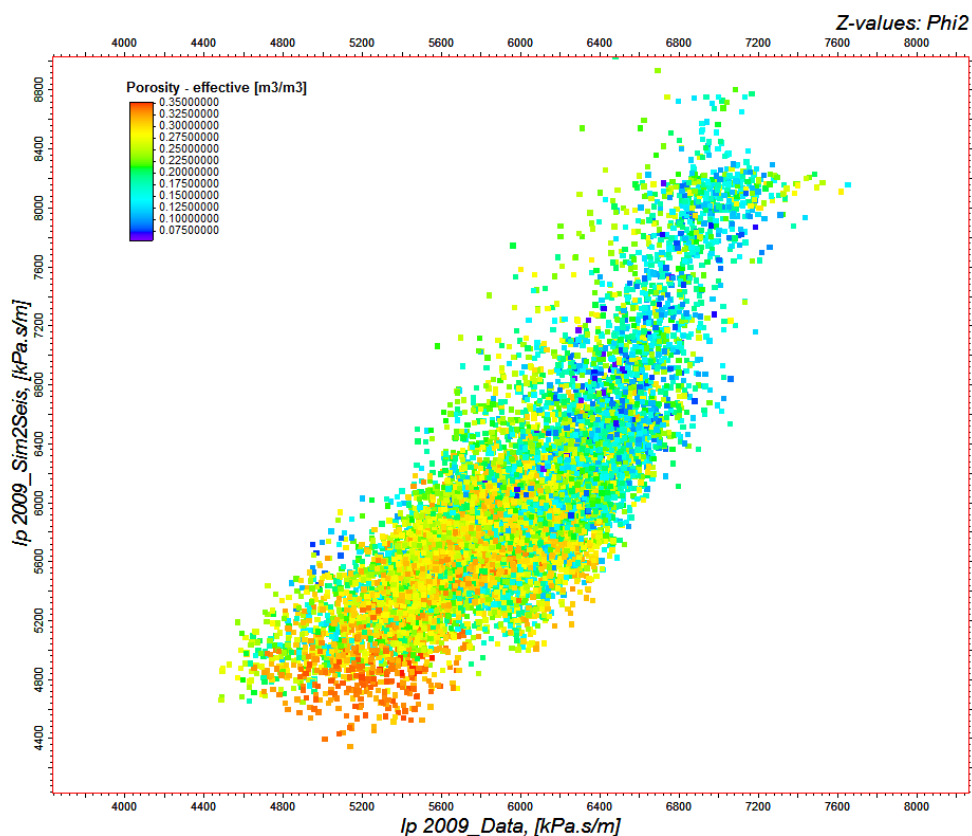


Figure 5.38, Modelled P-impedance vs. inverted P-impedance in 2009 (monitor case). Colors show effective porosity.

This case study was carried out to show the feasibility of the Sim2Seis approach for enhancing simulation forecasts. Thus far, we ended up with a reasonable agreement between modelled P-impedance and the inverted P-impedance for the monitor seismic survey. I did run the simulation again on the new grid cells with the updated properties. The history matching results is as good as figure 5.16, that's why it is not shown. However, the point is that this time we are more confident about the forecasts based on the new dynamic model since P-impedance is also reasonably matched.

Here are some limitations that I was aware of them and they are specific to this case study and should be considered further if one intends to enhance the results:

- Seismic and simulation resolutions are different, which means that for their comparisons it is impossible to get a perfect match, unless we impose appropriate upscaling/downscaling actions,
- This reservoir was heavy oil, so Gassmann's equation potentially can results in erratic results,
- Patchy saturation was very likely in this reservoir; fluid mixing laws and Gassmann's equation are prone to give misleading results,
- CHOPS production, impacts the porosity and permeability of the reservoir severely, which violates the Gassmann's equation, in the sense that solid frame not only changes but also flows. It worth to incorporate the geomechanical effects in the study as well.

My point is that the achieved results should be cautiously interpreted on the grounds of the known limitations. It is strongly, recommended to avoid doing the overcorrections, where we already know the compromises in this approach.

5.8 Summary

In this chapter, I implemented the seismic assisted history matching on a real case. For this purpose I developed a program (Sim2Seis) to convert simulation results to acoustic moduli. It was observed that comparison of the modelled acoustic moduli with those computed from seismic inversion, can increase the certainty of static and dynamic simulation models.

Chapter Six: **Conclusions**

6.1 Conclusions

The dynamic model for reservoir simulation should always be kept as simple as possible, but not simpler! In this thesis I have argued that ignoring time lapse seismic data, builds a model which is simpler than a trustworthy model.

I developed a plug-in program, called Sim2Seis that facilitated the contribution of seismic time-lapse data in reservoir history matching. During the seismic assisted history matching it was observed that many different geo-models resulted in equally reasonable history matched results. However, their resultant acoustic impedance models generated by Sim2Seis plug-in were different. This discrepancy is quite valuable, since it can enhance our perception of the geo-model and also can reduce the uncertainty in the simulation results.

In my research, viscoelastic fluid substitution modelling has also been studied using compositional fluid models. This has led to development of a practical fluid substitution framework that can be integrated with heavy oil phase behavior and simulation results. In cases with limited laboratory elastic measurements, the numerous uncertain parameters should be tuned with the available data before applying this modelling scheme to an entire reservoir.

The fluid compositional analysis suggests that viscosity is such a strong function of temperature and that the solution's gas cannot have a tangible influence on the elastic moduli of heavy oil reservoirs. Considering the small amounts of gas in solution and the low-pressure characteristics of heavy oil reservoirs, we can conclude that the viscosity

increase due to gas liberation can simply be ignored in heavy oils. Hence, the fluid shear modulus should decrease monotonically with increasing temperature.

In this research, different mechanisms, impacting wave propagation were discussed. These parameters are all coupled, and I scrutinized them individually for perceiving the mutual interactions of reservoir behaviour and elastic responses. To summarize, three factors compete or reinforce each other to characterize reservoir elastic properties. These are change in saturation, pore pressure and temperature, which might reinforce or cancel out each other, depending on different scenarios.

For instance, considering saturation variations, it is obvious that if water displaces oil, the velocity increase, where gas evolution tends to decrease the velocity.

In terms of pressure impacts, reservoir depletion causes pressure decline, which in turn leads to increase in effective pressure within the reservoir and velocity increase. On the other hand, injection increases the pore pressure and reduces effective pressure. This will result in a decrease in effective stress and velocity.

Introducing heat to the system will complicate the anelasticity of the rocks. On one hand it changes the pore pressure and saturations depending on the PVT properties of the pore fluid. In addition, injected steam will significantly reduce the velocity itself due to low velocity nature of steam. On the other hand thermal injection will add total stress which will act like an additional thermal load due to the expansion of the rocks and resistance of overburden and sideburdens. This will increase the effective stress in the reservoir and wave speed will also increase accordingly. The velocity speed up usually is masked due to the injected steam and evolved gas which tend to impede the propagating wave.

The degree of saturation, pressure and temperature impacts, depends on the fluid properties, stiffness tensor and thermal expansion coefficients, respectively while these parameters are coupled and do interact. It means that in the extreme cases, pore fluid properties (saturation, pressure, temperature), will influence a rock only if the rock is susceptible to change. Recalling that $P_{\text{eff}} = P_{\text{Confining}} - (1 - K_{\text{dry}}/K_{\text{matrix}}) \times P_{\text{pore}}$, one can see that P_{pore} , will effect P_{eff} only if K_{dry} is much smaller than K_{matrix} ; the situation that will happen for high porosity, weakly cemented rocks. High temperature also cannot significantly impact rocks as long as thermal expansion coefficient of the rock is small.

The stress effects are also observed in the host rock in addition to the reservoir. Overburden for example, resists to the changes in the reservoir. It means that shrinking the reservoir due to pore pressure reduction, will result in stretching the overburden, and velocity decrease accordingly. This behaviour is reversed in injection, where expansion of the reservoir is opposed by overburden, which will tend to speed up the velocity as a result.

In addition to the reservoir fluid parameters (saturation, pressure, temperature), and rock properties (elastic moduli, thermal expansion coefficient), the reservoir and overburden thickness also is a key factor. Needless to say that the resultant time shifts at the base of the reservoir, is the superposition of all the impacts that a wave experiences while propagates through the reservoir and overburden. The longer the path in the reservoir, the larger is the impact on wave travel time.

6.2 Suggestions for future works

This study can be extended in the following aspects:

1. The case study can be applied on thermal cases, to validate the fluid substitution models in viscoelastic fluids,

2. It worth including geomechanical simulations into the case study,
3. In the case study, patchy saturation calculations for the fluid moduli can be considered,
4. There are many rock physical models that I have pointed out in this research. A sensitivity analysis of different options is recommended,
5. Based upon the temperature-frequency-shear modulus relationship, a new approach has been proposed for estimating temperature in the reservoir. Further research in this regard, with application in real cases, is recommended to validate the proposed method.

6.3 Last words

The principal premise of this thesis was that the ambiguities of reservoir simulation can be reduced using time-lapse seismic data. A case study that was conducted in this research suggests that it is in fact quite rewarding to incorporate time-lapse seismic as assisting data in the reservoir simulation and history matching.

It is very important to note that the entire effort was to mitigate the risk of simulation forecasts and reduce the uncertainty of the reservoir model. In other words, we are more confident about the dynamic model, when it honours the seismic data in addition to the flow rate and reservoir pressures.

Despite all the endeavours to enhance the geo-model, we should bear in mind that the seismic assisted history matched model is still uncertain. In addition, similar to any other inversion problem, the demonstrated approach has its own uncertainties and challenges. Nonetheless the power of this method in mitigating the risks and increasing the confidence in the reservoir modelling is something that should be appreciated.

Appendix A: Peng-Robinson equation of state

The equation of state (EOS) is a thermodynamic equation relating pressure (p), temperature (T), volume (V) and composition to describe the state of the fluid. For real gasses, the equation of state is:

$$pV = znRT \quad (\text{A.1})$$

where n refers to the mole number, R is gas constant, and z is the gas compressibility factor, which is used to account for the non-ideality of real gasses. In 1976, Peng and Robinson introduced a new two-parameter EOS developed to improve the prediction of liquid density. This equation, in terms of the compressibility factor, takes a cubic form:

$$z^3 - (1 - B)z^2 + (A - 2B - 3B^2)z - (AB - B^2 - B^3) \quad (\text{A.2})$$

$$A = \frac{0.4572\alpha p_r}{T_r^2} \quad (\text{A.3})$$

$$B = \frac{0.077p_r}{T_r} \quad (\text{A.4})$$

$$\alpha = [1 + m(1 - \sqrt{T_r})]^2 \quad (\text{A.5})$$

$$m = (0.3796 + 1.485\omega - 0.1644\omega^2 + 0.01667\omega^3) \quad (\text{A.6})$$

where $p_r = \frac{P}{P_c}$, $T_r = \frac{T}{T_c}$, and T_c , P_c and ω are the critical temperature, critical pressure and acentric factor, respectively, the values of which are read from tables including properties of pure compounds.

A comparison of the predicted liquid molar volume using the PR (Peng-Robinson) EOS with experimental data of pure compounds always shows a systematic deviation. The deviation is almost constant over a wide range of pressures away from the critical point.

Hence, subtracting the predicted molar volume by a constant correction term can improve the predicted liquid density:

$$V^{cor} = V - c \quad (\text{A.7})$$

where V^{cor} is the corrected molar volume, and c is the correction term determined by matching the measured and predicted saturated liquid volumes at $T_r = 0.7$.

Jhaveri and Youngren (1988) related c to the parameter b , by defining a dimensionless shift parameter, S_E :

$$S_E = \frac{c}{b} \quad (\text{A.8})$$

where S_E was determined by matching the predicted and measured molar volumes for various hydrocarbons.

The roots (compressibility factors) of the EOS (A.2) can be used to determine whether the liquid and vapor phases are in equilibrium. In equilibrium conditions, the fugacities of all the components are equal in both phases, i.e. $\Phi_i^l x_i P = f_i^V = f_i^l = \Phi_i^l y_i P$, where f is fugacity, i refers to i^{th} component, v , l , x , and y refer to vapor and liquid phases, number of moles in the liquid and vapor phases, respectively. The fugacity coefficient, Φ , is calculated for both phases using the z values derived from (A.2), using the following expressions:

$$\ln(\Phi_i) = \frac{b_i}{b} (Z - 1) - \ln(Z - B) \quad (\text{A.9})$$

$$- \frac{A}{B(-2\sqrt{2})} \left(\frac{2 \sum_{j=1}^N X_j a_{ij}}{a} - \frac{b_i}{b} \right) \ln \left(\frac{Z + (1 - \sqrt{2})B}{Z + (1 + \sqrt{2})B} \right)$$

$$b_i = 0.077796RT_c/P_c \quad (\text{A.10})$$

$$b = \sum_i x_i b_i \quad (\text{A.11})$$

$$a_i = 0.457235 \alpha R^2 T_c^2 / P_c^2 \quad (\text{A.12})$$

$$a = \sum_i \sum_j x_i x_j a_{ij} \quad (\text{A.13})$$

where $a_{ij} = \sqrt{a_i a_j} (1 - K_{ij})$; R is a gas constant; A and B are calculated using (A.3) and (A.4), respectively; and, K_{ij} is referred to as the binary interaction parameter and can be read from chemical tables. For further detailed discussion, please refer to Danesh, 1998.

Appendix B: Coherent potential approximation method

The coherent potential approximation (CPA) method is an iterative method for estimating effective-medium moduli of a composite system. This self-consistent approximation starts with a guess for G_{sc}^* and K_{sc}^* , which are the effective shear and bulk moduli of the composite medium, respectively. The method also needs initial estimates for the aspect ratio of the grain and pore, α . The next step is the calculation of the values of functions θ and f for the constituents:

$$\theta = \begin{cases} \frac{\alpha}{(\alpha^2 - 1)^{3/2}} \left[\alpha(\alpha^2 - 1)^{1/2} - \cosh^{-1} \alpha \right] & \text{for prolate spheroids, } \alpha > 1 \\ \frac{\alpha}{(\alpha^2 - 1)^{3/2}} \left[\cosh^{-1} \alpha - \alpha(\alpha^2 - 1)^{1/2} \right] & \text{for oblate spheroids, } \alpha < 1 \end{cases} \quad (\text{B.1})$$

$$f = \frac{\alpha^2}{1 - \alpha^2} (3\theta - 2) \quad (\text{B.2})$$

The iteration then initiates and continues until the difference between the old and new elastic moduli becomes less than a tolerance value or the iterations exceed a maximum number. The following formulations summarize the approach for calculating geometric factors P and Q (Berryman, 1980b):

$$\vartheta_{sc} = \frac{3K_{sc} - 2G_{sc}}{6K_{sc} + 2G_{sc}} \quad (\text{B.3})$$

$$A_i = \frac{G_i}{G_{sc}} - 1 \quad (\text{B.4})$$

$$R = \frac{1 - 2\vartheta_{sc}}{2(1 - \vartheta_m)} \quad (\text{B.5})$$

$$B_i = 1/3 \left(\frac{K_i}{K_{sc}} - \frac{G_i}{G_{sc}} \right) \quad (\text{B.6})$$

$$F_{1i} = 1 + A_i \left[\frac{3}{2} (f + \theta) - R \left(\frac{3}{2} f + \frac{5}{2} \theta - \frac{4}{3} \right) \right] \quad (\text{B.7})$$

$$F_{2i} = 1 + A_i \left[\frac{3}{2} (f + \theta) - R \left(\frac{3}{2} f + \frac{5}{2} \theta \right) \right] + B_i (3 - 4R) \quad (\text{B.8})$$

$$+ \frac{1}{2} A_i (A_i + 3B_i) (3 - 4R) [f + \theta - R(f - \theta + 2\theta^2)]$$

$$F_{3i} = 1 + A_i \left[1 - \left(f + \frac{3}{2} \theta \right) + R(f + \theta) \right] \quad (\text{B.9})$$

$$F_{4i} = 1 + \frac{1}{4} A_i [f + 3\theta - R(f - \theta)] \quad (\text{B.10})$$

$$F_{5i} = A_i \left[-f + R \left(f + \theta - \frac{4}{3} \right) \right] + B_i \theta (3 - 4R) \quad (\text{B.11})$$

$$F_{6i} = 1 + [1 + f - R(f + \theta)] + B_i (1 - \theta) (3 - 4R) \quad (\text{B.12})$$

$$F_{7i} = 2 + \frac{1}{4} A_i [3f + 9\theta - R(3f + 5\theta)] + B_i \theta (3 - 4R) \quad (\text{B.13})$$

$$F_{8i} = A_i \left[1 - 2R + \frac{1}{2} f (R - 1) + \frac{1}{2} \theta (5R - 3) \right] \quad (\text{B.14})$$

$$+ B_i (1 - \theta) (3 - 4R)$$

$$F_{9i} = A_i [(R - 1)f - R\theta] + B_i \theta (3 - 4R) \quad (\text{B.15})$$

$$s = T_{iijj} = \frac{3F_1}{F_2} \quad (\text{B.16})$$

$$T_{ijij} - \frac{1}{3} T_{iijj} = \frac{2}{F_3} + \frac{1}{F_4} + \frac{F_4 F_5 + F_6 F_7 - F_8 F_9}{F_2 F_4} \quad (\text{B.17})$$

$$P_i = \frac{1}{3} T_{iijj} \quad (\text{B.18})$$

$$Q_i = \frac{1}{5} \left(T_{ijij} - \frac{1}{3} T_{iijj} \right) \quad (\text{B.19})$$

The last step is the guessing of a new K_{sc} and G_{sc} from the following relations:

$$\sum_{i=1}^N x_i (K_i - K_{sc}^*) P^{*i} = 0 \quad (\text{B.20})$$

$$\sum_{i=1}^N x_i (G_i - G_{sc}^*) Q^{*i} = 0 \quad (\text{B.21})$$

where i refers to the i^{th} component; x_i is its volume fraction; P^{*i} and Q^{*i} are geometric factors, and the superscript $*i$ on P and Q indicates that the factors are for the inclusion of material i in a background medium with self-consistent effective moduli K_{sc}^* and G_{sc}^* . Please refer to the Mavko et al. (2009) for a more detailed explanation.

Appendix C: Pedersen correlation for estimating viscosity

The Pedersen viscosity (Pedersen et al., 1984) correlation is based on the principal of corresponding states in which the mixture viscosity, μ , is related to a reference viscosity, μ_o , by terms involving the mixture's properties: critical temperature, T_C , critical pressure, P_C , and molecular weight, MW .

The deviation from simple corresponding states is accounted for by a rotational coupling coefficient, α . The viscosity of the mixture is calculated according to the following formula:

$$\begin{aligned} \mu(P, T) & \quad (C.1) \\ &= \left(\frac{T_{c,mix}}{T_{c,o}}\right)^{-1/6} \left(\frac{P_{c,mix}}{P_{c,o}}\right)^{4/6} \left(\frac{MW_{mix}}{MW_o}\right)^{3/6} \left(\frac{\alpha_{mix}}{\alpha_o}\right) \mu_o(P_o, T_o) \end{aligned}$$

where subscript *mix* refers to the mixture property and subscript *o* refers to the reference material, which was taken to be methane in the Pedersen model.

The critical pressure and temperatures for the mixture can be found using mixing rules, e.g. $\theta_{c,mix} = \sum z_i \theta_i$, where θ_c is the critical property (pressure or temperature), z is the mole fraction and subscript i refers to the i^{th} component in the mixture.

The molecular weight of the mixture is determined from:

$$\begin{aligned} MW_{mix} &= 1.3404 \times 10^{-4} b_1 (MW_w^{2.303 \times b_2} - MW_n^{2.303 \times b_2}) \quad (C.2) \\ &+ MW_n \end{aligned}$$

where MW_w is the weight fraction averaged molecular weight, and MW_n is the mole fraction averaged molecular weight. The rotational coupling coefficient is calculated as:

$$\alpha_m = 1 + b_5 \varphi_{rm}^{b_3} MW_m^{b_4} \quad (\text{C.3})$$

$$\alpha_o = 1 + b_6 \varphi_{rm}^{b_3} \quad (\text{C.4})$$

where φ_{rm} is the reduced density (density calculated at reduced pressure and reduced temperature, where reduced property is defined as $\theta_r = \theta/\theta_c$), and b_1 to b_6 are the tuning parameters.

References

- Arenas, E.M., T. Oldenziel, and C.P.J.W. Van kruijsdijk, 2001, History matching a reservoir model to time-lapse seismic using the pilot point method: EAEG 63rd conference & technical exhibition, Amsterdam, the Netherlands.
- Batzle, M., and Z. Wang, 1992, Seismic properties of pore fluids: *Geophysics*, **57**, 1396–1408.
- Batzle, M., R. Hofmann, and D.-H. Han, 2006, Heavy oils—seismic properties: The Leading Edge, **25**, 750–757.
- Beggs, H. D., and J. R. Robinson, 1975, Estimation of the viscosity of crude oil systems: *Journal of Petroleum Technology*, 27, 1140–1141.
- Behura, J., M. Batzle, R. Hofmann, and J. Dorgan, 2007, Heavy oils: Their shear story: *Geophysics*, **72**, no. 5, E175–E183.
- Berryman, J.G., 1980b, Long-wavelength propagation in composite elastic media: *J. Acoustic. Soc. Am.*, **68**, 1809–1831.
- Berryman, J.G., 1995, Mixture theories for rock properties in rock physics and phase relations: A handbook of physical constants, ed. T.J. Ahrens. Washington, DC: American Geophysical Union.
- Bown, T. D., and D. R. Schmitt, 2010, Seismic dispersion in extra-heavy oil saturated rock: *GeoCanada 2010*.
- Brie, A., F. Pampuri, A.F. Marsala, and O. Meazza, 1995, Shear sonic interpretation in gas-bearing sands: *SPE 30595*, 701-710.
- Caers J., T. Hoffman, S. Strebelle, and X. W. Wen, 2006, Probabilistic integration of

geologic scenarios, seismic, and production data—a west Africa turbidite reservoir case study: *The Leading Edge*, **25**(3), 240-244.

Carlson, M. R., 2006, *Practical reservoir simulation: using, assessing, and developing results*: PennWell.

Ciz, R., and S. A. Shapiro, 2007, Generalization of Gassmann's equations for porous media saturated with a solid material: *Geophysics*, **72**, no. 6, A75– A79.

Danesh A., 1998, *PVT and phase behavior of petroleum reservoir fluids*: Elsevier.

Das, A., and M. Batzle, 2008, Modelling studies of heavy oil in between solid and fluid properties: *The Leading Edge*, 27, 1116–1123.

Davis, T.L. and R.D, Benson, Tight-gas seismic monitoring, Rulison Field, Colorado: *The Leading Edge*, April 2009, v. 28, p.408-411.

Dillen, M.W.P, H.M.A. Cruts, J. Groenenboom, J.T. Fokkema, and A.J.W Duijdam, 1999, Ultrawave velocity and shear-wave splitting behavior of a Colton sandstone under a changing triaxial stress: *Geophysics*, 64(5), 1603-1607.

Dusseault M. B., and P. M. Collins, 2009, Heavy oils: reservoir characterization and production monitoring: *Geophysical developments*, No. 13, p287-291.

Dvorkin, J., and A. Nur, 1996, Elasticity of high-porosity sandstones: theory for two North Sea datasets, *Geophysics*, 61, 1363-1370

Eastwood, J., 1993, Temperature-dependent propagation of P-waves and S-waves in Cold Lake oil sands: Comparison of theory and experiment: *Geophysics*, 58, 863–872.

Ertekin, T., J.H. Abou-Kassem, and G.R. King, 2001, *Basic Applied Reservoir Simulation*. SPE Textbook Series. Richardson, Tex.: Society of Petroleum Engineers.

Ferry, J. D., 1980, *Viscoelastic properties of polymers*: JohnWiley&Sons.

- Gassmann, F., 1951, Über die Elastizität poröser Medien: Vierteljahrsschr. der Naturforsch. Gesellschaft Zurich, 96, 1-23.
- Gosselin, O., S. I. Aanonsen, I. Aavatsmark, A. Cominelli, R. Gonard, M. Kolasinski, F. Ferdinandi, L. Kovacic, and K. Neylon, 2003, History Matching Using Time-Lapse Seismic (HUTS): Proceedings of the SPE Annual.
- Gregory, A.R., 1976, Fluid saturation effects on dynamic elastic properties of sedimentary rocks: Geophysics, v. 41, p. 895–921.
- Grasso, J.-R., 1992, Mechanics of seismic instabilities induced by the recovery of hydrocarbons: Pure and applied geophysics, 139, 507-534.
- Gurevich, B., K. Osypov, R. Ciz, and D. Makarynska, 2008, Modelling elastic wave velocities and attenuation in rocks saturated with heavy oil: Geophysics, 73, no. 4, E115–E122.
- Guy, N., J.-F. Nauroy, and A. Baroni, 2013, Influence of SAGD process on seismic velocities: ARMA 13-676.
- Hall, S. A., C. MacBeth, (2001), 4D-4C AVOA at Teal South: 63th EAGE conference exhibition.
- Han, D. H., A. Nur, and D. Morgan, 1986, Effects of porosity and clay content on wave velocities in sandstones: Geophysics, 51, 2093-2107.
- Han, D.-H., Q. Yao, and H.-Z. Zhao, 2007a, Complex properties of heavy oil sand: 77th Annual International Meeting: SEG, Expanded Abstracts, 1609–1613.
- Hashin, Z., and S. Shtrikman, 1963, a variational approach to the theory of the elastic behavior of multiphase materials: Journal of the Mechanics and Physics of Solids, 11, 127–140.

Hatchell, P. J., A. van den Beukel, M. M. Molenaar, K. P. Marin, C. J. Kenter, J. G. F. Stammeijer, J. J. van den Velde, and C. M. Sayers, 2003, whole earth 4D: monitoring geomechanics: 73rd Annual international meeting, SEG, Expanded abstract, 1330-1333.

Hatchell, P., and S. Bourne, 2005, Rocks under strain: strain induced time-lapse time shifts are observed for depleting reservoirs: *The Leading Edge*, 24, 1222-1225.

Hearmon, R.F.S. (1953), Third-order elastic coefficients: *Acta Crystallographica*, 6, 331-340.

Hernandez, R.I.I, 2011, Numerical reservoir simulation coupled with geomechanics state of the art and application in reservoir characterization: SPE 152364-STU.

Herwanger, J., E. Palmer, C. R. Schiøtt, (2007), Anisotropic Velocity Changes In Seismic Time-lapse Data: 2007 SEG Annual Meeting, 23-28 September, San Antonio, Texas, SEG-2007-2883.

Herwanger, J., and S. Horne, 2009, Linking reservoir geomechanics and time-lapse seismics: Predicting anisotropic velocity changes and seismic attributes: *Geophysics*, 74, W13-W33.

Herwanger, J., and N. Koutsabeloulis, 2011, Seismic geomechanics: how to build and calibrate geomechanical models using 3D and 4D seismic data: European Association of Geoscientists & Engineers Publications B.V. (EAGE).

Hill, R., 1952, the elastic behaviour of a crystalline aggregate, *Proc. Phys. Soc. A* 65 349

Hornby, B. E., 1995, the elastic properties of shales, Ph.D. dissertation: Cambridge University, England.

Hornby, B. E., 1998, Experimental laboratory determination of the dynamic elastic properties of wet, drained shales: *Journal of geophysical research*, 103(B12), 29945-29964.

- Huang, X., L. Meister, and R. Workman, 1997, Reservoir characterization by integration of time-lapse seismic and production data: SPE 38695.
- Jaeger, J. C., N. G.W. Cook, and R.W. Zimmerman, 2007, Fundamentals of rock mechanics, 4th ed.: Blackwell Publishing.
- Jhaveri, B. S., and G. K. Youngren, 1988, Three-parameter modification of Peng-Robinson equation of state to improve volumetric predictions: SPE 13118.
- Johnson, D. L., 2001, Theory of frequency dependent acoustics in patchy-saturated porous media, JASA, 110, 682-694.
- Kato, A., S. Onozuka and T. Nakayama, 2008, Elastic property changes in a heavy oil reservoir during steam injection: The Leading edge, 27, 1124-1131.
- Kazemi, A., and K. D. Stephen, 2011, Automatic production and seismic history matching by updating locally and by geological environment in the Nelson Field: SPE 143629.
- Kelkar, M., and Perez, G., 2002, Applied Geostatistics for Reservoir Characterization: Society of Petroleum Engineers
- Krief, M., J. Garta, J. Stellingwerff, and J. Ventre, 1990, A petrophysical interpretation using the velocities of P and S waves (Full-waveform sonic): The Log Analyst, v. 31, p. 355–369.
- Kuster, G.T., and Toksöz, M.N., 1974, Velocity and attenuation of seismic waves in two-phase media: Part I. theoretical formulations: Geophysics, 39, 587-606.
- Lakes, R., 2009, Viscoelastic materials: Cambridge university press.
- Lee M. W., 2003, Velocity Ratio and its Application to Predicting Velocities: U.S. Geological Survey Bulletin 2197.

MacBeth, C., 2004, A classification for the pressure-sensitivity properties of a sandstone rock frame: *Geophysics*, 69(2), 497-510.

Makarynska, D., B. Gurevich, J. Behura, and M. Batzle, 2010, Fluid substitution in rocks saturated with viscoelastic fluids: *Geophysics*, 75, no.2, E115-E122.

Mavko, G., C. Chan, and T. Mukerji, 1995, Fluid substitution: estimating changes in V_p without knowing V_s , *Geophysics*, 60, 1750-1755.

Mavko, G., T. Mukerji, and J. Dvorkin 2009, *the Rock Physics Handbook*: Cambridge University Press.

Menard, K. P., 1999, *Dynamic mechanical analysis: A practical introduction*: CRC Press.

Mezghani, M., A. Fornel, V. Langlais, and N. Lucet, 2004, History matching and quantitative use of 4D seismic data for an improved reservoir characterization: SPE 90420.

Mindlin, R.D., 1949, Compliance of elastic bodies in contact: *Journal of Applied Mechanics*, 16, 259–268.

Murphy, W., A., Reischer, and K., Hsu, 1993, Modulus decomposition of compressional and shear velocities in sand bodies: *Geophysics*, 58, 227-239.

Nakayama, T., A. Takahashi, L. Skinner and A. Kato, 2008, Monitoring an oil-sands reservoir in northwest Alberta using time-lapse 3D seismic and 3D P-SV converted-wave data: *The leading edge* 27: 1158-1175,

Nur, A., C. Tosaya, and D. V. Thanh, 1984, Seismic monitoring of thermal enhanced oil recovery processes: 54th Annual International Meeting, SEG, Expanded Abstracts, 118–121.

Ogushwitz, P. R., 1985, Applicability of the Biot theory. I–Low porosity materials: *Journal of the Acoustical Society of America*, 77, 429–440.

- Pedersen, K. S., A. Fredenslund, P. L. Christensen, and P. Thomassen, 1984, Viscosity of crude oils: *Chem. Eng. Sci.* **39**(6), 1011-1016.
- Peng, D.-Y., and D.B. Robinson, 1976, A New Two-Constant Equation of State: *Ind. Eng. Chem. Fundamentals*.
- Prioul, R., A. Bakulin, and V. Bakulin, 2004, Nonlinear rock physics model for estimation of 3D subsurface stress in anisotropic formations: Theory and laboratory verification: *Geophysics*, **69**, 415-425.
- Samier, P., A. Onaisi and G. Fontaine, 2003, Coupled analysis of geomechanics and fluid flow in reservoir simulation: *SPE 79698*,
- Sarkar, D., A. Bakulin, B. Karanz (2003), 2003, Anisotropic inversion of seismic data for stressed media: theory and physical-modelling study on Bereca sandstone: *Geophysics*, **68** (2), 690-704.
- Sayers, C M., 2005, Sensitivity of elastic wave velocities to reservoir stress path: *SEG/Houston 2005 Annual Meeting*.
- Sayers, C M., 2010, *Geophysics under stress: Geomechanical applications of seismic and borehole acoustic waves*, Distinguished Instructor Series,
- Schmitt, D. R., 1999, Seismic attributes for monitoring of a shallow heated heavy oil reservoir: A case study: *Geophysics*, **64**, 368–377.
- Segall, P., 1989, Earthquakes triggered by fluid extraction, *Geology*, **17**, 942-946
- Sheriff, R. E., and L. P. Geldart, 1995, *Exploration Seismology*: Cambridge University Press
- Smith, T. M., C. H. Sondergeld, and C. S. Rai, 2003, Gassmann fluid substitutions: A tutorial: *Geophysics*, Vol. **68**, no. 2, 430–440.

- Staples, R., J. Ita, R. Burrell, and R. Nash, 2007a, Monitoring pressure depletion and improving geomechanical models of the Shearwater field using 4D seismic: *The Leading Edge*, 26, 636-642.
- Sung, Y., M. Ravalec., C. Hubans, P-O. Lys, and D. Foulon, 2009, seismic monitoring of steam flooding in a depleted mobile heavy oil field: models of steam drive (SD) and steam assisted gravity drainage (SAGD): SEG, Houston Annual meeting.
- Timur, A., 1977, Temperature dependence of compressional and shear wave velocities in rocks: *Geophysics*, 42, 950-956.
- Tran, D., L. Nghiem, and L. Buchanan, 2009, Aspects of coupling between petroleum reservoir flow and geomechanics: ARMA 09-89.
- Van Dok, R. R., J. E. Gaiser, and T. Probert (2004), Time-lapse shear wave splitting analysis at Ekofisk field, North Sea: 66th EAGE conference exhibition.
- Viswanath, D. S., K. T. Ghosh, D. L. Prasad, N. V. K. Dutt, and K.Y. Rani, 2007 , *Viscosity of Liquids Theory, Estimation, Experiment, and Data*: Springer.
- Wang, Z., 2001, Fundamentals of seismic rock physics: *Geophysics*, 66, P. 398-412.
- Wang, Z., and Nur, A., 1990b, Wave velocities in hydrocarbon, saturated rocks: Experimental results: *Geophysics*, 55, 723-733.
- Wilson, G., 1968, A Modified Redlich-Kwong EOS, Application to general physical data calculations: Paper No 15C, presented at the AIChE 65th National Meeting.
- Zoback, D., 2012, *Reservoir geomechanics*: Cambridge University Press.
- Zou, Y., L. R. Bentley, and L. R. Lines, 2006, Integration of seismic methods with reservoir simulation, Pikes Peak heavy-oil field, Saskatchewan: *The Leading Edge*.